

**COMPUTATIONAL INVESTIGATION OF  
AEROMECHANICAL HCF EFFECTS IN A  
COMPRESSOR ROTOR**

**THESIS**

Andrew L. White, 2Lt, USAF

AFIT/GAE/ENY/01M-09

**DEPARTMENT OF THE AIR FORCE  
AIR UNIVERSITY**

**AIR FORCE INSTITUTE OF TECHNOLOGY**

**Wright-Patterson Air Force Base, Ohio**

**APPROVED FOR PUBLIC RELEASE; DISTRIBUTION UNLIMITED.**

**20010523 019**

The views expressed in this thesis are those of the author and do not reflect the official policy or position of the United States Air Force, Department of Defense, or the U. S. Government.

COMPUTATIONAL INVESTIGATION OF AEROMECHANICAL  
HCF EFFECTS IN A COMPRESSOR ROTOR

THESIS

Presented to the Faculty  
Department of Aeronautics and Astronautics  
Graduate School of Engineering and Management  
Air Force Institute of Technology  
Air University  
Air Education and Training Command  
In Partial Fulfillment of the Requirements for the  
Degree of Master of Science in Aeronautical Engineering

Andrew L. White, B.S.

2Lt, USAF

March 2001

APPROVED FOR PUBLIC RELEASE; DISTRIBUTION UNLIMITED.

COMPUTATIONAL INVESTIGATION OF AEROMECHANICAL HCF  
EFFECTS IN A COMPRESSOR ROTOR

Andrew L. White, B.S.  
2Lt, USAF

Approved:

Paul King

Dr. Paul King (Chairman)

14 Mar 01

date

William C. Elrod

Dr. William Elrod (Member)

14 Mar 01

date

Montgomery C. Hughson

Maj. Montgomery Hughson (Member)

14 MAR '01

date

Mitch Wolff

Dr. Mitch Wolff (Member)

14 Mar 01

date

## **Acknowledgments**

I would like to express my appreciation to my faculty advisor, Dr. Paul King, for his guidance throughout the course of this thesis effort. The insight and experience was certainly appreciated. I would also like to thank my advisors from Wright State University, Dr. Mitch Wolff and Dr. David Johnston for their help in making this thesis come together. I would also like to thank my sponsors at AFRL, Dr. Steve Puterbaugh and Mr. Dave Car for their help in educating me about the CARL facility.

I am also indebted to the Linux system administrators at AFIT and at Wright State University, Mr. Jim Gray and Mr. Timothy Leger for their hard work getting their computer systems to perform as I needed them to.

Andrew L. White

## Table of Contents

	Page
Acknowledgments .....	iv
List of Figures .....	vii
List of Tables .....	ix
List of Symbols .....	x
List of Abbreviations .....	xi
Abstract .....	xii
<b>I. Introduction .....</b>	<b>1</b>
HCF Problem.....	1
Computational Fluid Dynamics .....	3
Detuning.....	4
Research Proposal and Approach.....	8
<b>II. TESCOM.....</b>	<b>10</b>
HSL Program.....	10
TESCOM Design .....	10
Previous TESCOM Research.....	12
<b>III. ADPAC .....</b>	<b>13</b>
General Concepts .....	13
Numerical Algorithm .....	14
Convergence Acceleration Techniques .....	15
Boundary Conditions .....	19
Turbulence Modeling.....	20
<b>IV. TIGER.....</b>	<b>23</b>
General Concepts .....	23
Grid Generation.....	24
Grid Modification.....	25

	Page
V. Grid Generation .....	27
Geometry Modifications .....	27
Tuned Grid Generation.....	30
Detuned Grid Generation .....	33
VI. Methodology .....	35
Tuned Rotor Case.....	35
Detuned Rotor Case .....	39
VII. Results.....	40
Grid Sensitivity .....	40
Steady-State Results.....	41
Unsteady Results .....	43
Force and Moment Analysis .....	48
Overall Performance Analysis .....	50
VIII. Conclusions and Recommendations.....	51
Figures.....	53
Appendix A. $Y^+$ Calculations For Viscous Grids .....	89
Bibliography.....	91
Vita.....	93

## List of Figures

Figure	Page
1. CARL TESCOM Three-Stage Compressor Rig (Meridional View) .....	53
2. TESCOM Configuration 1A Streamline Geometry .....	54
3. TESCOM Stage 1 (Configuration 1A) Performance Map .....	55
4. Upstream Inlet Computational Mesh (two-dimensional).....	56
5. Tuned Computational Mesh.....	57
6. Detuned Computational Mesh.....	58
7. Tuned Compressor Map (Steady-State) .....	59
8. Tuned Efficiency Map (Steady-State).....	59
9. Tuned Steady-State Convergence Plot.....	60
10. Tuned Unsteady Convergence Plot .....	61
11. Detuned Steady-State Convergence Plot.....	62
12. Schematic of the Detuned Geometry .....	63
13. Grid Independence Study .....	64
14. Tuned IGV $C_p$ Steady-State Profiles.....	65
15. Detuned IGV A Steady-State $C_p$ Profiles.....	66
16. Detuned IGV B Steady-State $C_p$ Profiles.....	67
17. Tuned Rotor Steady-State $C_p$ Profiles.....	68
18. Detuned Rotor A Steady-State $C_p$ Profiles.....	69
19. Detuned Rotor B Steady-State $C_p$ Profiles.....	70
20. Steady-State Mach Contours, Tuned and Detuned Cases .....	71

Figure	Page
21. Axial Velocity Contours, Tuned and Detuned Cases.....	72
22. Tuned IGV Unsteady $C_p$ Profiles .....	73
23. Detuned IGV A Unsteady $C_p$ Profiles.....	74
24. Tuned Case Unsteady Pressure Contours .....	75
25. Tuned Rotor Unsteady $C_p$ Profiles .....	77
26. Detuned Rotor A Unsteady $C_p$ Profiles.....	78
27. Detuned Rotor B Unsteady $C_p$ Profiles .....	79
28. Unsteady $C_p$ Amplitude Estimates, Tuned and Detuned Cases .....	80
29. Unsteady Loading, Tuned Case .....	81
30. Unsteady IGV Loading, Detuned Case.....	82
31. Unsteady Rotor Loading, Detuned Case .....	83
32. IGV Forces Time History and Fourier Analysis .....	84
33. IGV Moment Time History and Fourier Analysis .....	85
34. Rotor Forces Time History and Fourier Analysis .....	86
35. Rotor Moment Time History and Fourier Analysis .....	87
36. IGV First Harmonics.....	88
37. Rotor First Harmonics.....	88

## **List of Tables**

Table	Page
1. TESCOM Performance .....	12
2. Overall Performance Comparison .....	50

## List Of Symbols

Symbol	
ft	feet
s	seconds
lb	pounds
D	discrete dissipative function
Q	vector of discrete solution vectors
$\Delta$	difference operator
$\lambda$	dissipation scaling factor
$\epsilon$	dissipation coefficient, smoothing coefficient
$\Phi$	relative dissipation scaling function, mass flow parameter
p	pressure
$\nu$	dissipation coefficient, kinematic viscosity
$\alpha$	dissipation exponent
u	axial velocity
$\kappa$	dissipation constant
R	residual vector, gas constant
$Q_m$	sum of convective and dissipative terms
$D_m$	total dissipation
$\tau$	shear stress
$\mu$	viscosity
$C_f$	skin friction coefficient
Re	Reynolds number
$\rho$	density
$\mathbf{V}$	total velocity
$\theta$	meridional coordinate
x,y,z	Cartesian coordinate directions
$y^+$	viscous wall coordinate
$C_p$	coefficient of pressure
T	temperature
P	pressure
A	area
$g_c$	gravitational constant
$\gamma$	ratio of specific heats
M	Mach number

### Subscripts

i,j,k	coordinate indices
$\xi, \eta, \zeta$	computational space coordinates
m	Runge-Kutta stage number
wall	value at solid wall
rel	relative
n	near-wall values
0	stagnation conditions

### List of Abbreviations

HCF	H-Cycle Fatigue
Hz	Hertz
CFD	Computational Fluid Dynamics
ADPAC	Advanced Ducted Propfan Analysis Codes
TIGER	Turbomachinery Interactive Grid Generator
HSL	High Stage Loading
AFRL	Air Force Research Laboratory
IGV	Inlet Guide Vane
CARL	Compressor Aero Research Lab
NASA	National Aeronautics and Space Administration
GUI	Graphical User Interface
FORTRAN	Formula Translation
CFL	Courant-Freiderichs-Lewy Number
MB	Megabyte
RAM	Random Access Memory
Mbit	Mega bit

### **Abstract**

High-Cycle Fatigue is a major problem facing the gas turbine industry today. It has been investigated by many researchers, using many different methods. Due to its highly complex nature, designers still do not have adequate tools to accurately predict the onset of high-cycle fatigue.

A three-dimensional Navier-Stokes program was used to perform a study of the unsteady aerodynamics on a compressor rotor. The effect of aerodynamic detuning on the forced response of a rotor blade was compared to a baseline tuned rotor case. Detuning consisted of a ten percent decrease in circumferential spacing between alternate pairs of blades. The high-cycle fatigue effects of this detuning were investigated by examining the unsteady forces and moments on the rotor blades and inlet guide vanes.

Computations were performed using a three-dimensional NASA research code (ADPAC) on a cluster of five desktop PCs. Computational times were on the order of several days for a grid of approximately 500,000 cells. These computations showed that detuning of the rotor blade could result in a reduction in the forced response of the IGV and rotor blades. This reduction came without much loss in overall performance (less than ten percent) and therefore may be a viable option to reduce high-cycle fatigue.

# **COMPUTATIONAL INVESTIGATION OF AEROMECHANICAL HCF EFFECTS IN A COMPRESSOR ROTOR**

## **I. Introduction**

### **HCF Problem**

High-cycle fatigue (HCF) of turbomachinery components is a serious problem in the gas-turbine industry. It results from blade cracking or fracture due to a large number of cycles at stresses well below the yield strength of the material [1]. Although more than 90% of potential HCF problems are discovered during engine developmental testing, the remaining 10% account for nearly 30% of the total development cost [1]. HCF research is focused on the need for increased durability and reliability of turbomachinery components, since those characteristics impact operational and maintenance costs and flying safety. Still lacking though is a complete understanding of the flow physics within turbomachinery components.

HCF typically describes failure associated with vibratory stress cycles resulting from resonant vibrations combined with moderate levels of steady stresses. The frequencies of interest usually range from 100 Hz to 20 kHz. Conceptually, this is a simple definition. However, turbomachinery designers still do not have robust methods to predict future HCF failures. This is due to the nature of the highly complex

interactions in turbomachinery components. These include, but are not limited to, unsteady aerodynamics, material capability and vibratory stresses.

Current engine design requirements demand a higher thrust-to-weight ratio and reduced specific fuel consumption. These requirements necessitate significant changes from previously successful design practices. Engines today have fewer compressor and turbine stages with higher stage pressure ratios, low aspect ratio blades and minimal axial spacing between stages. These factors result in blade designs that are highly stressed and that are subjected to increased levels of aerodynamic excitation with reduced overall damping. These factors are the primary drivers of HCF failures.

As mentioned before, one of the driving factors behind HCF failures is the unsteady aerodynamics produced by blade row interactions. In a transonic compressor, the rotor blade operates with a supersonic relative velocity that has a subsonic axial component. Shocks form near the rotor blade leading edges and propagate upstream into the neighboring vane row. With closely spaced blade rows, these upstream-propagating shocks generate a strong forcing function to the upstream vane row. This generates a potential for HCF failures [2].

Upstream blade rows can also cause excitation of downstream blade rows. This excitation is caused by the passage of an upstream blade, which generates a wake. This wake travels downstream and excites the downstream blade. Each time an upstream blade passes, its wake produces unsteady loading, thereby exciting the downstream blade. In current engine design, the upstream blades are typically tuned (blade-to-blade spacing uniformity), and as a result, the excitation of the downstream row is periodic. This

periodicity results in the downstream blade being excited at fixed frequencies. This fixed-frequency excitation is also a major driver of HCF failures.

The unsteady aerodynamics that cause HCF failures are generated by strong blade row interactions due to the highly unsteady nature of the flow. This unsteady flow field is inherently three-dimensional. Therefore, to accurately predict HCF failures (and as a result, design blades for longer life), a three-dimensional Navier-Stokes solver should be employed. Current computer advances allow such codes to generate results in a time frame that is compatible with the early part of the design process.

### Computational Fluid Dynamics

Recently, it has become practical to use Computational Fluid Dynamics (CFD) to solve turbomachinery problems using Euler solvers for inviscid or ideal flows or Navier-Stokes solvers for viscous flows. This is due to advancements in computer technology such as parallel processing, as well as developments in efficient numerical techniques. These advances allow for the solution of single or multiple blade rows to be generated in a reasonable amount of time.

Given a proper computational mesh, current CFD codes do an adequate job of predicting unsteady aerodynamic loading trends on turbomachinery components [3]. This includes loading due to various factors such as potential interactions, waves, shocks, and flutter.

Current engine design trends include uniformly spaced, highly loaded and fewer compressor and turbine blades. The uniformly spaced vanes or blades produce uniform and periodic wakes that excite downstream blade rows. These continuous excitations are

at fixed high frequencies correlated with the engine rotation speed and are thought to be the leading cause of fatiguing and cracking of the blade.

The uniformity of blade passages is exploited in most current CFD analyses, since the computational domain can be reduced by assuming that a single passage represents the blade row. This uniformity is not entirely realistic, however, since as-built components always experience some random blade-to-blade variability due to manufacturing tolerances and surface irregularities [4]. Intentional blade-to-blade variability, however, may present an opportunity to shift the stress-inducing frequencies to a lower level. Blade spacing variability would result in several different low-frequency modes being excited with each rotation of the rotor and may reduce fatigue cycles by an order of magnitude.

The unsteady aerodynamic flow field generates two separate HCF effects [5,6] on blade rows. Flutter is defined as an individual blade oscillating in the presence of a uniform free stream flow. Flutter develops abruptly and grows until the blade fails. A second effect is called the forced response problem. The forced response problem is caused by a blade row generating an aerodynamic forcing function for the oscillation of neighboring blade rows. In a tuned rotor, this forcing function excites the neighboring blade row (upstream or downstream) in a periodic fashion. This periodic excitation can also cause HCF failures.

### Detuning

Operating a compressor rotor in the transonic or supersonic regime produces both flutter and forced response HCF effects. These factors must be addressed in the design of

a transonic axial flow compressor. One approach to control both the flutter and forced response problems is called detuning. Detuning is defined as a prescribed non-uniformity of some type in the design of the rotor.

Detuning can be classified as either structural detuning or aerodynamic detuning. Structural detuning is defined as blade-to-blade differences in the natural frequencies of a blade row resulting from variations in blade structural properties [7]. Mathematical models have been developed that demonstrate even small amounts of variability (and hence, structural detuning) that occur in the manufacturing process can have an effect on the both the flutter and forced response of rotors [7]. Structural detuning has been investigated and its effects quantified by several investigators [8,9]. These effects show that structural detuning can eliminate the flutter problem, but can either alleviate or magnify the forced response problem, depending on the level of detuning and the specific geometry being investigated. Structural detuning is not universally accepted in the aerospace community as a means to eliminate or control vibrational forced response in the operation of a compressor [7]. This is because of the associated manufacturing, material, maintenance and cost problems, just to name a few.

The other type of detuning is aerodynamic detuning. Aerodynamic detuning is defined as passage-to-passage differences in the aerodynamic flow field across a blade row. Aerodynamic detuning causes blade-to-blade differences in the unsteady forces and moments acting on a blade row. These blade-to-blade differences result in a blade response that is unlike the classical traveling wave typical of the vibrational forced response of an aerodynamically tuned rotor. Therefore, aerodynamic detuning affects the

driving characteristics of vibrational forced response, the unsteady aerodynamic forces and moments on a blade row.

In a classically tuned rotor, the downstream blade row responds at integral multiples of the rotor blade pass frequency. Aerodynamic detuning functions by breaking up the fundamental periodicity of the blade row forced response. This results in the downstream blade row responding not only at integral multiples of the blade pass frequency, but also at other integral multiples of the rotor shaft pass frequency [10]. This will affect the HCF problem, as the blade row will be excited at various frequencies, not just at the rotor blade pass frequency. This has the effect of spreading out the vibrational forced response over several frequencies, which should result in less fatiguing of the blade.

Hoyniak and Fleeter performed a two-dimensional analysis of a flat-plate airfoil cascade embedded in a supersonic inlet flow field [7]. Using an influence coefficient technique, the effects of alternate blade-to-blade circumferential spacing on an unstalled supersonic turbofan cascade were investigated. Alternate blade-to-blade spacing effectively creates small changes in the blade solidity. Small changes in blade row solidity typically do not have a significant effect on overall performance. In their study, it was determined that aerodynamic detuning has a stabilizing effect on the flutter stability of a blade row. Therefore, it was determined that this type of detuning could potentially be beneficial with regard to the flutter of a blade row at a variety of rotor operating conditions.

Chiang and Fleeter [5] also carried out a flutter analysis of aerodynamic detuning using an influence coefficient technique. Their analysis also suggested that aerodynamic

detuning produces enhanced rotor flutter stability. An examination of the phase and magnitude of the steady and unsteady pressure differences showed that enhanced stability of the detuned rotor is associated with the effect of the aerodynamic detuning on the phase of the unsteady pressure difference.

Another investigation of aerodynamic detuning was conducted by Spara and Fleeter [6]. This investigation used an influence coefficient method applied to three rotor geometries with a supersonic axial component. Each rotor geometry was investigated in three different configurations. One configuration was tuned, and the other two incorporated different levels of aerodynamic detuning. For each geometry, the forced response of the two detuned (10% and 20% detuning) cases was compared to the baseline tuned case for three gust modes.

For the first blade geometry, detuning decreased the response amplitude for both detuning levels, and it was observed that a higher level of detuning resulted in a larger decrease in the response amplitude. For the second geometry tested, the 10% detuned case decreased the response for the two largest gust modes, but increased it for the smallest. The 20% detuning resulted in a decrease in the response amplitude for all gust modes. The final geometry tested showed that both levels of aerodynamic detuning increased the response amplitude for all gust modes. These results show that aerodynamic detuning may or may not alleviate forced response of a rotor blade. This depends on the specific level of detuning and the blade geometry under investigation. Spara and Fleeter's results will be somewhat different than results obtained from our effort, due to their supersonic axial velocity component compared with the subsonic axial component for this research.

## Research Proposal and Approach

The purpose of this research was to utilize state-of-the-art CFD principles to perform a high-fidelity analysis of the potential HCF effects of aerodynamic detuning on the forced response of a compressor rotor. To this end, an experimental compressor called TESCOM was computationally investigated. TESCOM is a research compressor rig designed at the Air Force Research Laboratory (AFRL), and its first stage (inlet guide vane and rotor only) was the subject of this research. TESCOM Stage 1 has configurations designated 1A and 1B, and configuration 1A will be investigated in this research. TESCOM represents several aspects of modern compressor design in that each stage is highly loaded, and the blades are of low aspect ratio. A further description of this compressor rig and its associate blade geometry can be found in Chapter 2.

The flow field over the TESCOM geometry was calculated using a three-dimensional Navier-Stokes program called ADPAC (Advanced Ducted Propfan Analysis Codes). ADPAC is a research code developed by Allison Engine Co. in cooperation with NASA Lewis Research Center. A detailed discussion of ADPAC can be found in Chapter 3.

To generate ADPAC solutions, a computational mesh was generated using the TIGER™ (Turbomachinery Interactive Grid generation) grid generator developed by Catalpa Research, Inc. TIGER™ is designed for generating H-type and C-type turbomachinery grids, including grids with sufficient resolution to adequately model viscous effects. A detailed description of the TIGER™ software follows in Chapter 4.

Using a computational mesh that has appropriate resolution for a viscous solution, a steady state solution was generated. This steady-state solution was input as a starting

solution for the unsteady calculations. Once the tuned case was investigated in both the steady state and unsteady analyses, a detuned rotor was analyzed. In order to accurately model a detuned rotor, a new computational mesh will be generated. This computational mesh models an alternately spaced ten percent detuned rotor geometry. The results from the unsteady calculations for the detuned rotor were then compared to the baseline tuned case. ADPAC generates output that describes the unsteady forces and moments on the blade. These unsteady forces and moments were analyzed to determine the potential HCF effects of aerodynamic detuning on a compressor rotor.

## II. TESCOM

### HSL Program

TESCOM is a low aspect ratio, 3.5 stage axial flow compressor designed at the Air Force Research Laboratory (AFRL), Wright-Patterson AFB, Ohio. This rotor design was part of what is now called the High Stage Loading (HSL) project. The goal of the HSL program was to generate an 8:1 pressure ratio in three stages. Currently, two of these stages have been manufactured and tested. This compressor is to have an inlet corrected tip speed of 1250 ft/s, and a mass flow rate of 24.5 lb<sub>m</sub>/s (other performance data is given in Table 2, below). The HSL program took a stage-by-stage approach, in which one stage was designed, built and tested before the next stage design was undertaken [11]. To achieve the desired compression ratio, counterswirl was to be employed in each stage. This approach resulted in rotor sections with a combination of significant camber and high inlet relative Mach numbers. An axial view of the TESCOM rig is show in Figure 1, pg. 52.

### TESCOM Design

The first stage (configuration 1A) was developed in 1979 [12]. This first stage includes an inlet guide vane, rotor and stator, and was designed for high stage loading. The performance objectives of the compressor were selected to reduce the required number of stages to generate a certain pressure ratio without compromising stage efficiency. A preliminary study was conducted, and it was determined that maximum

compressor efficiency would occur with an optimum balance of diffusion losses and shock losses. This condition determined the velocity diagrams at the rotor leading edge. For this research, an IGV blade row was included in the analysis in order to generate upstream wakes that would provide a forcing function to the downstream rotor blade row.

The first stage (configuration 1A) was designed using a well-known streamline curvature through flow program, UD0300M [13]. An initial estimate of the blade geometry was known from the preliminary study, and was used as the starting point for UD0300M. This program utilizes the method of streamline curvature for aerodynamic analysis and analyzes compressor performance for a given blade geometry.

UD0300M is divided into an aerodynamic analysis section and a blade geometry definition section. Using the initial estimate of the blade geometry from the preliminary study, the aerodynamic analysis was completed. The calculated relative flow angles are used to generate the resulting blade geometry. This blade geometry was input into the aerodynamic section to generate new flow angles. The program was iterated in this fashion a number of times to optimize the aerodynamic behavior and blade geometry. The geometry that results from this iteration is the “hot” geometry, i.e., a geometry that is untwisted with rotation. A correction for the rotation and blade untwist is applied to generate the “cold” geometry used for manufacturing. The resulting “hot” geometry of the TESCOM IGV rotor 1A can be seen in Figure 2. Other performance data of the TESCOM rig is given in the following table.

Table 1. TESCOM performance

Rotor tip speed (corrected):	1250 ft/s
Rotor hub speed (corrected):	803.62 ft/s
Rotor mean speed (corrected):	1026.69 ft/s
IGV Inlet Mach Number	0.2224
Rotor Inlet Mach Number	0.5204
Rotor total pressure ratio:	2.2631
Rotor isentropic efficiency:	0.8893

### Previous TESCOM Research

The one-stage TESCOM configuration 1A was tested in the Compressor Aero Research Lab (CARL) facility in 1983 [14]. It was tested at various equivalent speeds and flow rates to generate a detailed compressor map. This compressor map can be seen in Figure 3. This compressor map (at 100% speed) shows a very narrow operating region (where the curve begins to flatten out) before reaching the stall line. This is characteristic of this configuration of high stage loading and a low aspect ratio.

More recently, a CFD analysis of the TESCOM rig was conducted in the CARL facility [11]. In this analysis, two different first stage rotors were tested, rotors R1A and R1B. Rotor R1A was designed by Air Force personnel, while Garrett Turbine Engine Company (currently Honeywell Corp.) designed R1B. In their work, Car and Puterbaugh [11] tested both configurations in the CARL facility. The experimental results showed that both configurations had acceptable performance, but 1A showed a slight shortfall in design-point mass flow and pressure ratio. Configuration 1B achieved the design points in all aspects. Therefore, configuration R1B was selected for further CFD analysis by Car and Puterbaugh [11]. No further analysis has been conducted on the TESCOM (configuration 1A) compressor rig.

### III. ADPAC

#### General Concepts

ADPAC (Advanced Ducted Propfan Analysis Codes) was developed by the Allison Engine Company under NASA sponsorship. It is a three-dimensional time-marching Navier-Stokes solver for the aerodynamic analysis of modern turbomachinery components. These components can have single or multiple blade rows. It is capable of generating either steady state or time-dependent solutions, and it can be executed in either serial or in parallel.

ADPAC utilizes a multiple-block solution concept. This means that the solution domain is divided into logical blocks that can be solved simultaneously. An example of using multiple solution blocks would be dividing compressor or turbine stage geometry into two blocks, one block containing the rotor blade and one block containing the stator blade. ADPAC allows for an arbitrary number of solution blocks, which allows the user a lot of flexibility in specifying the solution domain.

To generate a solution for multiple blade rows, there must be some method for predicting the interaction of relatively rotating blade rows. ADPAC offers two methods. For steady-state solutions, a mixing plane (an arbitrarily imposed boundary) is defined in the region between the two blade rows. In the mixing plane, the flow is circumferentially averaged. This mixing is designed to approximate the time-averaged conditions at the mixing plane and allows the for a steady-state solution for each blade passage to be performed. The flow variables on either side of the mixing plane are averaged circumferentially and passed to neighboring blade rows. This averaging smears out

circumferential non-uniformities, and because of this is only suitable for steady-state flows.

For unsteady solutions, predicting the interaction of neighboring blade rows is much more involved and computationally expensive. To do this, multiple blade passages per blade row may need to be modeled. Multiple blade passages would be necessary in many unsteady situations, such as differing blade counts in neighboring blade rows, or in the case of non-uniform spacing of the blades in a blade row. If the blade counts for both blade rows are identical and the spacing between blades is uniform, then only one blade passage per blade row need be modeled.

### Numerical Algorithm

The numerical algorithm employed by ADPAC is based on an integral representation of the strong conservation law form of the 3-D Reynolds-Averaged Navier-Stokes equations. It is a finite-volume technique, and the solution can be applied in either a cylindrical or Cartesian coordinate system [3]. ADPAC contains four different turbulence models that the user can select from. The Baldwin-Lomax algebraic turbulence model and a mixing-length turbulence model are the simplest and least computationally expensive. ADPAC can also employ the one-equation Spalart-Allmaras turbulence model or the two-equation  $k-\bar{\mathcal{R}}$  turbulence model, which are more accurate, but also more computationally expensive.

A multistage Runge-Kutta integration technique is used to step the solution in time. For simplicity, viscous flux contributions to the discretized equations are only calculated for the first stage (at each time level) of the Runge-Kutta integration, and the

values are frozen for the remaining stages. This reduces the overall computational effort, and does not significantly alter the solution. ADPAC offers the user three different Runge-Kutta schemes (two four-stage methods, and one five-stage method).

For steady flow calculations, a local time-stepping method is employed. Local time-stepping allows for the maximum allowable time step to be utilized at each solution point. This greatly enhances convergence for steady-state problems. Global time-stepping is used for time-dependent calculations.

### Convergence Acceleration Techniques

To improve solution quality, and to accelerate convergence, artificial dissipation terms must be added to the discretized form of the governing equations. A blend of fourth and second differences is used to provide a third order background dissipation in smooth flow regions and first order dissipation near discontinuities. The dissipation coefficients are pressure-based, and therefore can “sense” discontinuities such as shock waves. This allows the dissipation model to prevent non-physical oscillations that can occur near shock waves. The discrete dissipation function is given as follows:

$$D_{i,j,k}(Q) = (D_i^2 - D_i^4 + D_j^2 - D_j^4 + D_k^2 - D_k^4)Q_{i,j,k} \quad (1)$$

The second and fourth order dissipation operators are determined by:

$$D_\xi^2 Q_{i,j,k} = \nabla_\xi ((\lambda_\xi)_{i+\frac{1}{2}, j+\frac{1}{2}} \epsilon^2) \Delta_\xi Q_{i,j,k} \quad (2)$$

$$D_\xi^4 Q_{i,j,k} = \nabla_\xi ((\lambda_\xi)_{i+\frac{1}{2}, j+\frac{1}{2}} \epsilon^4) \Delta_\xi \nabla_\xi \Delta_\xi Q_{i,j,k} \quad (3)$$

where  $\Delta_\xi$  and  $\nabla_\xi$  are forward and backward difference operators in the  $\xi$  direction. To maintain the damping properties of the scheme, a variable scaling is employed. This scaling is given by the following:

$$(\lambda_\varepsilon)_{i+\frac{1}{2},j,k} = (\lambda_\varepsilon)_{i+\frac{1}{2},j,k} \Phi_{i+\frac{1}{2},j,k} \quad (4)$$

The function  $\Phi$  controls the relative importance of dissipation in the three coordinate directions as:

$$\Phi_{i+\frac{1}{2},j,k} = 1 + \max \left( \left( \frac{(\lambda_\eta)_{i+\frac{1}{2},j,k}}{(\lambda_\xi)_{i+\frac{1}{2},j,k}} \right)^\alpha, \left( \frac{(\lambda_\xi)_{i+\frac{1}{2},j,k}}{(\lambda_\xi)_{i+\frac{1}{2},j,k}} \right)^\alpha \right) \quad (5)$$

The directional eigenvalue scaling functions are defined by:

$$(\lambda_\xi)_{i+\frac{1}{2},j,k} = U_{i+\frac{1}{2},j,k} (S_\xi)_{i+\frac{1}{2},j,k} + c(S_\xi)_{i+\frac{1}{2},j,k} \quad (6)$$

$$(\lambda_\eta)_{i+\frac{1}{2},j,k} = U_{i+\frac{1}{2},j,k} (S_\eta)_{i+\frac{1}{2},j,k} + c(S_\eta)_{i+\frac{1}{2},j,k} \quad (7)$$

$$(\lambda_\zeta)_{i+\frac{1}{2},j,k} = U_{i+\frac{1}{2},j,k} (S_\zeta)_{i+\frac{1}{2},j,k} + c(S_\zeta)_{i+\frac{1}{2},j,k} \quad (8)$$

For three-dimensional grids, a value of  $\alpha=0.5$  was found to generate a robust scheme [3].

This is because three-dimensional grids generally have large variations in cell aspect ratio, which reduces the freedom in choosing a value of  $\alpha$ .

The coefficients in the dissipation operator use the solution pressure as a sensor for the presence of shock waves in the solution and are defined as:

$$\varepsilon_{i+\frac{1}{2},j,k} = K_2 \max(v_{i-1,j,k}, v_{i,j,k}, v_{i+1,j,k}, v_{i+2,j,k}) \quad (9)$$

$$v_{i,j,k} = \frac{|(p_{i-1,j,k} - 2p_{i,j,k} + p_{i+1,j,k})|}{(p_{i-1,j,k} + 2p_{i,j,k} + p_{i+1,j,k})} \quad (10)$$

$$\varepsilon_{i+\frac{1}{2},j,k}^4 = \max(0, \kappa_4 - \varepsilon_{+\frac{1}{2},j,k}^2) \quad (11)$$

where  $\kappa_2, \kappa_4$  are user-defined constants. Typical values for these constants are:

$$\kappa_2 = \frac{1}{2} \quad (12)$$

$$\kappa_4 = \frac{1}{64} \quad (13)$$

The dissipation operators in the  $\eta$  and  $\zeta$  directions are defined in a similar manner.

ADPAC also uses an implicit residual smoothing method to accelerate convergence of the Runge-Kutta integration scheme. Jameson *et al.* [15] first applied this method to the Runge-Kutta scheme. This technique can be incorporated into a time-accurate explicit method without adversely affecting the unsteady results [16]. Residual smoothing is applied at each time step of the Runge-Kutta integration, and permits the use of larger time increments.

The standard implicit residual smoothing operator can be written as:

$$(1 - \varepsilon \Delta \nabla) R_m^* = R_m \quad (14)$$

To simplify the numerical implementation, this standard operator is traditionally approximately factored into the following coordinate specific form:

$$(1 - \varepsilon_\xi \Delta_\xi \nabla_\xi)(1 - \varepsilon_\eta \Delta_\eta \nabla_\eta)(1 - \varepsilon_\zeta \Delta_\zeta \nabla_\zeta) \bar{R}_m = R_m \quad (15)$$

where the residual  $R_m$  is defined as:

$$R_m = \alpha_m \frac{\Delta t}{V} (Q_m - D_m), \quad m=1, m \text{ stages} \quad (16)$$

for each of the  $m$  stages in the Runge-Kutta multistage scheme. Here  $Q_m$  is the sum of the convective and diffusive terms,  $D_m$  the total dissipation at stage  $m$ , and  $R_m$  the final (smoothed) residual at stage  $m$ .

The smoothing reduction is applied sequentially in each coordinate direction as:

$$R_m^* = (1 - \varepsilon_\xi \Delta_\xi \nabla_\xi)^{-1} R_m \quad (17)$$

$$R_m^{**} = (1 - \varepsilon_\eta \Delta_\eta \nabla_\eta)^{-1} R_m^* \quad (18)$$

$$R_m^{***} = (1 - \varepsilon_\zeta \Delta_\zeta \nabla_\zeta)^{-1} R_m^{**} \quad (19)$$

$$\bar{R}_m = R_m^{***} \quad (20)$$

The coefficients ( $\varepsilon$ ) are allowed to vary in this scheme. This method was described for three-dimensional flows by Radespiel *et al.* [17].

To accelerate convergence, a multi-grid technique is incorporated into ADPAC. A multi-grid approach generates a coarser mesh from an initial, fine mesh by removing every other mesh line in each coordinate direction. This multi-grid method calculates the solution on the fine mesh, and copies it to the next coarser mesh. The appropriate forcing functions are calculated from the differences between the coarse mesh residual and the residual that results from a summation of the fine mesh residuals for the coarse mesh cell. The solution is then advanced on the coarse mesh. This sequence is repeated until the coarsest mesh is reached. A correction to the solution is then interpolated to the next finer mesh, and a new solution is defined for that mesh. This interpolation is repeated until the finest mesh is reached.

For starting a solution, a different multi-grid technique is employed. Once a coarser mesh is generated, the solution is generated on the coarse mesh, and then that

solution is applied to the next finer mesh by interpolation. The solution procedure is then iterated on the finer mesh. Since a good approximation to the solution now exists on the finer mesh, convergence of the solution is more rapid. This multi-grid technique can be applied repetitively, resulting in coarser and coarser meshes. The solution procedure starts on the coarsest mesh, and the solution for one grid level is applied to the next finer one. Starting on the coarse mesh and applying the solution to successively finer meshes is called a “full” multi-grid startup procedure. This applies to starting a solution only, and is different from a typical multi-grid technique.

In steady-state flow calculations, the solution algorithm is an explicit method. In time-dependent calculations, ADPAC utilizes an implicit time-marching procedure. This algorithm can utilize all the convergence acceleration methods given above for the explicit time-marching procedure. For a further discussion of this implicit method see the ADPAC documentation [3].

### Boundary Conditions

Inlet and exit boundary conditions are applied using characteristic theory. This method is essentially a reference plane method of characteristics based on Riemann invariants. This method uses a local rotated coordinate system, which is normal to the bounding cell face. Solid surface boundary conditions have either a no-slip condition applied (viscous flow) or a no flow-through condition (inviscid flow). Values of the variables in the phantom cells are calculated so as to satisfy these conditions. ADPAC can utilize both standard reflecting boundary conditions and non-reflecting boundary

conditions. The non-reflecting boundary condition method follows the method described by Giles [18] and Sixer [19].

To communicate results between blocks in a multiple-block solution, the boundary data from one block is simply copied to the phantom cells of the neighboring block. This method works for adjoining blocks that have coincident points along the block-to-block interface. Communicating data in this way uniformly enforces the conservation principles present in the governing equations.

### Turbulence Modeling

The algebraic turbulence model used by ADPAC is a relatively standard version of the Baldwin-Lomax turbulence model. This model is computationally efficient and has been successfully applied to a wide range of geometries and flow conditions. For more details on this model, see the ADPAC documentation [3]. This turbulence model is valid provided that there is adequate grid density near solid surfaces to capture the viscous flow behavior. Typically, this implies that the first point off the wall should have a  $y^+$  value of one or less. ADPAC is very sensitive to mesh expansion ratios (basically the ratio of the lengths of two adjacent grid cells in any coordinate direction), and in order to keep mesh expansion ratios below a certain limit (around 1.3 for ADPAC), it may not be possible to comply with the  $y^+$  value of 1.0 without using an inordinately large number of grid points. As a result, the wall function method is used to empirically specify the wall shear stress. This method results in a large savings in computational time with only a minor sacrifice in accuracy.

The wall function method used in ADPAC involves manipulation of the near-wall eddy viscosity. Normally, the no-slip condition is relaxed in the wall function method. However, in this implementation, the no-slip condition was preserved. An overview of the development of this method follows. A shear stress at the wall such as:

$$\tau_{xy} = \mu \frac{\partial u}{\partial y} \quad (21)$$

is calculated numerically as:

$$\tau_{xy} = \mu_{wall} * \frac{\Delta u}{\Delta y} \quad (22)$$

where, in this case,  $\mu$  represents the combined turbulent and laminar viscosities:

$$\mu_{wall} = \frac{1}{2} (\mu_{i,2} + \mu_{i,1}) \frac{(\mu_{i,2} - \mu_{i,1})}{\Delta y} \quad (23)$$

The subscript i,j indicates a mesh oriented cell-centered flow value, where i,1 is the value in the phantom cell, and i,2 is the value at the first interior cell near the wall. The ADPAC implementation instead modifies the wall turbulent viscosity boundary condition through manipulation of the single term  $\mu_{i,1}$ . This implies that the turbulent viscosity at the wall is non-zero, which violates the normal specification. However, since the turbulent viscosity is used exclusively in the calculation of the wall shear stress and heat conduction terms, the resulting calculations are consistent with the desired shear stress specification. This formulation, in effect, also implies a wall function based on heat flux. For calculations in which heat transfer is unimportant, this effect is negligible.

The shear stress specification used by ADPAC is based on the following formula for the wall shear stress coefficient:

$$c_f = -0.001767 + 0.03177 / \text{Re}_n + 0.25614 / \text{Re}_n^2 \quad (24)$$

The term  $Re_n$  is the Reynolds number based on near-wall velocity, density, and viscosity, where the length scale is the normal distance from the wall to the first interior domain calculation cell. The wall shear stress may then be calculated from:

$$\tau_{wall} = \frac{1}{2} c_f \rho V_{rel}^2 \quad (25)$$

where  $V_{rel}$  is the near-wall relative flow total velocity.

## IV. TIGER

### General Concepts

To successfully generate an ADPAC solution, a mesh for the solution domain must be generated. ADPAC does not generate its own mesh, so the grid must be generated by another method. For this research, the TIGER™ (Turbomachinery Interactive Grid generation) grid generator was used. TIGER™ is a commercial software package developed by Catalpa Research, Inc. It was designed specifically for turbomachinery applications, and has been used successfully for both internal and external flow fields.

TIGER™ employs a graphical user interface (GUI) that allows the user to easily input geometry and generate a mesh [20]. It includes options that allow the user to specify the distribution of points (i.e. clustering near solid surfaces for a viscous grid). TIGER™ also includes options to allow the user to select from various grid solution techniques (elliptic, Laplace, TIGER, etc.). It can be run either interactively or in batch mode. Batch mode allows the user to specify the various input parameters in two input files. These files are then read and the input parameters are placed in the appropriate fields in the GUI. Executing TIGER™ in batch mode is the fastest way to get a grid generated, as the user can quickly step through the various input panels.

## Grid Generation

To generate grids in TIGER™, the points that define the geometry are input into a TIGER™ format geometry input file. The first part of this geometry file contains two axial-radial curves that define the flow path geometry. The second part of the geometry file reads in the coordinates that define the blade geometry. For a cylindrical coordinate system, the geometry file contains axial, radial and meridional coordinates for the suction and pressure surfaces.

TIGER™ expects these points to be divided into several “slices” (at least five). These slices should stack up from hub to tip in the radial direction, but each slice need not be at a constant radial coordinate. Also, TIGER™ expects the points to be ordered from leading edge to trailing edge for both the pressure and suction surfaces. After much trial and error, it was determined that for best performance of the mesh generator, the first point in the file for both the pressure and suction surfaces should be the point which is farthest upstream in the axial direction, and the last point should be the point which is farthest downstream in the axial direction. These two points may or may not correspond to the actual leading and trailing edges of the blade geometry. Since TIGER™ requires the same number of points along both the pressure and suction surfaces, some reordering and interpolation of points along the blade may be required.

The second input file required by TIGER™ supplies various input parameters for the generation of the grid. These parameters can also be input into the GUI. This history file defines the total number of points in each coordinate direction, the number of grid blocks represented by the associated geometry file (usually one for one), the number of

blades around the hub and what type of flow field (internal or external). This file also contains a flag that controls whether or not the blade needs to be cut or extended to the boundaries defined by the flow path, and the indices for the blade leading and trailing edges, the blade hub and tip, etc.

From the input geometry, TIGER™ fits a spline to generate its grid boundaries. If there are not enough points present in regions of curvature (or in linear regions as well), the spline will produce oscillations that are not present in the actual geometry. To solve this problem, a few points can be linearly interpolated into the region of oscillations, and once there are enough points (this typically required around five new points to be interpolated), the oscillations in the spline fit will disappear. At this point, TIGER™ also determines if the blade geometry spans the entire flow path. If not, the program extends the blade geometry to the radial limits of the flow path through interpolation. If the blade geometry extends beyond the radial limits of the flow path, TIGER™ cuts the geometry to the exact radial dimensions required by the flow path.

### Grid Modification

As stated earlier, TIGER™ allows the user to specify spacing along grid boundaries. For blade boundaries, a packing file is generated that contains the spacing coefficients along the blade leading and trailing edges, and along the blade hub and tip boundaries. To specify spacing along flow path boundaries (inlet, exit, hub, case), the spacing coefficients are input into TIGER™ interactively. In both the packing file and the GUI, the user can select a spacing method as well. The available methods are even

spacing, exponential clustering, or hyperbolic tangent clustering. The exponential and hyperbolic tangent methods can be selected to cluster toward the lower index, the upper index, or both.

Once the spacing methods and coefficients are input, TIGER™ allows the user to view the proposed mesh before it is actually written to an output file. This view also allows the user to switch between various grid generation methods such as Laplace, elliptic, TIGER, etc. By inspecting the grid in a cascade view, the user can see where potential problem areas (such as highly skewed cells, or cells with negative volumes) in the grid might be. TIGER™ allows the user to shift major grid lines (such as the line connecting adjacent leading or trailing edges in a cascade view) to “fix” problem areas in the grid. These problem areas often occur near blade leading or trailing edges, where the geometry has a high degree of curvature.

Once manual inspection and adjustment of the grid is done, TIGER™ can then actually generate the grid. During this process, all cell volumes are calculated, and if there are negative volumes, their locations are reported in an output file. TIGER™ outputs grids in PLOT3D format.

## V. Grid Generation

### Geometry Modifications

To generate a grid for this research, the TESCOM 1A configuration (IGV and rotor) geometry (blade and flow path geometry) was acquired from the CARL facility. This geometry was given in streamline curvature format (Figure 2). This format is Cartesian (X,Y,Z) points separated into pressure surface, suction surface, and leading edge points. These points were given along eleven different streamlines in a left-handed coordinate system. To prepare this geometry for use in TIGER™, several FORTRAN programs were written to read in the points and then output them in the proper format.

The given flow path geometry included the entire length used in actual testing of the TESCOM rig. Since this research only involves the IGV and rotor blades, the flow path was cut off approximately sixty percent chord downstream of the rotor trailing edge. Upstream, the flow path was cut off approximately one chord upstream of the IGV leading edge. In order to accurately model the boundary layer growth in the bell mouth of the inlet, a grid was generated for this upstream region as well. Since this region contains no blade geometry, it could be modeled as a two-dimensional region that is symmetric around the centerline of the flow path (Figure 4). For clarity, this figure only includes the lines of constant radial location and not the lines of constant axial location.

The blade geometry was converted to a right-handed coordinate system for use in TIGER™. An axial shift was applied so that the IGV and rotor would be in their proper locations relative to one another along the TESCOM flow path. To insure that the blade

geometry spanned the entire radial height of the flow path, the inner and outer blade streamlines were copied and shifted in the radial direction. This generated two new streamlines that were outside the radial limits of the flow path.

As the blade geometry was given, the trailing edge of the IGV and rotor was a "block" trailing edge. TIGER™ requires a closed surface around the blade geometry. Using a three-dimensional vector approach, three trailing edge points were generated and appended to the pressure and suction surfaces. This created a closed trailing edge on the blade geometry.

TIGER™ is very sensitive to abrupt changes in cell aspect ratio. This means that the spacing between one pair of points cannot differ greatly from the spacing between the next pair of points. Due to the nature of the given points, there was a large difference in spacing where the leading edge points joined the pressure and suction surfaces. To correct this problem, approximately ten points were interpolated using a three-dimensional vector approach between the last point of the leading edge and the first point of the pressure and suction surfaces. To gently smooth out the spacing across these ten points, the interpolated points were clustered slightly toward the leading edge.

The original TESCOM geometry contains 36 IGV blades and 34 first stage rotor blades. A limitation of ADPAC is that it does not employ phase-lagged boundary conditions. Therefore, to model blade rows with dissimilar blade counts, it is necessary to model enough blade passages so that the entire circumferential span of the modeled portion of both blade rows is identical. In this case, that would require modeling 18 IGV passages and 17 rotor passages. This would result in a very large computational mesh, and the time required to generate a solution would be inordinately large. For this

research, it was assumed that both blade rows had 34 blades so that one IGV passage and one rotor passage could be modeled for a tuned geometry.

These changes were applied to the TESCOM IGV and rotor geometry. Through trial and error, it was determined that the points describing the rotor blade needed to be modified. As mentioned in the previous section, it was found that for best performance of the mesh generator, the first point in the file for both the pressure and suction surfaces should be the point which is farthest upstream in the axial direction, and the last point should be the point which is farthest downstream in the axial direction. Since these points do not correspond to the actual leading and trailing edges of the rotor blade, a cubic spline interpolation routine was used to generate points along the suction and pressure surfaces of the rotor blade. These interpolated points were based on the given rotor geometry once the various modifications described above had been applied. To adequately resolve the curvature at the leading and trailing edges, these points were distributed in the axial direction using a cosine function. This cosine function clustered points to both the leading and trailing edges.

To make the geometry compatible with TIGER™ format, the meridional coordinate was calculated using the formula:

$$\theta = \arctan\left(\frac{z}{y}\right) \quad (26)$$

The coordinates for both the flow path (axial, radial) and the blade geometry (axial, radial, meridional) were input into a TIGER™ input file.

## Tuned Grid Generation

As stated earlier, ADPAC uses a multi-grid technique to accelerate solution convergence. This means that any interval in the grid (inlet to blade leading edge, hub to case, etc.) needs to have an appropriate number of cells so that it can be divided into smaller pieces by removing every other mesh line. Typically, three levels of multi-grid are desired. This means that in any interval, the number of cells must be a number that can be divided in half at least twice and still remain an integer value. Typically integers that are a power of two are best at this, as they can be divided in half several times before becoming non-integer. TIGER™ allows the user to specify the indices for the various boundaries (blade leading edge, hub, case, etc.). This allows the user to set up the intervals so that the multi-grid technique can be used. These indices are specified in the history file.

As mentioned before, TIGER™ accepts a packing file that indicates how the grid points are to be distributed along the blade surfaces, and it also accepts GUI input to apply point distribution to any other surface (inlet, hub, case, etc.). To generate a grid suitable for viscous calculations, a  $y^+$  value of 1.0 was assumed. Using standard day conditions and experimental data from the TESCOM data report [14], an actual  $y$  coordinate based on this  $y^+$  value could be calculated. This technique is outlined in Appendix A.

TIGER™ expects a non-dimensional spacing coefficient in the packing file and in the GUI. This spacing coefficient is determined by dividing this actual  $y$  coordinate by the  $y$  value necessary to produce even spacing across the region of interest. Using a spreadsheet, this value could be computed for various locations, such as the inlet, the

IGV trailing edge, the rotor leading edge, etc. Applying these spacing coefficients at the proper locations in the packing file and in the GUI generated a grid that accurately represents the hub and case boundary layers. The chosen clustering method was a hyperbolic tangent function. This approach was also used for the blade-to-blade boundary layer in the circumferential direction. In this case, the Reynolds number was based on one-half chord length for the blade of interest.

To accurately resolve flow properties near the leading and trailing edges of the blade, it is necessary to cluster points in the axial direction toward the leading and trailing edges of both blades. For the blade hub and case surfaces, this is accomplished by specifying a clustering method and spacing coefficient in the packing file. For the flow path surfaces, this is accomplished by inputting the desired clustering method and spacing coefficients into the GUI. In all cases, the clustering method used was a hyperbolic tangent method. To generate a smooth mesh, an appropriate spacing coefficient across the blade was assumed, and the coefficients for the neighboring sections of the flow path were determined by trial and error so that the spacing to the first point on either side of the blade edges would be identical.

Final adjustments to the grid were made by using TIGER™ to curve some of the major gridlines (i.e. the line connecting the leading edges of neighboring blades in a cascade view). These lines were bowed in order to avoid the possibility of negative volumes, and to reduce the mesh expansion ratios. These modifications served to effectively “relax” the grid, so as to create a smoother mesh. Also, it was here that the grid generation solver (elliptic, Laplace, etc.) could be selected. For this grid, the TIGER

generation method was chosen. The TIGER method is a combination of algebraic and elliptic grid generation methods.

After inputting this grid to the ADPAC solver, it was found that the ADPAC solution diverged once the multi-grid procedure reached the finest mesh level. After much trial and error, it was determined that ADPAC is extremely sensitive to mesh expansion ratios. It was found that the only way to prevent this from happening was to relax the viscous spacing present in the grid.

TIGER™ only allows for two different clustering methods (exponential and hyperbolic tangent). In order to keep computational time down, only a certain number of points in each coordinate direction could be used. With a relatively small number of points and a very small spacing coefficient near solid boundaries, the mesh expansion ratios became too large for ADPAC to handle. To keep these ratios down, a compromise was reached by utilizing a larger spacing coefficient. This was chosen based on an approximate  $y^+$  value of ten instead of one. This value was chosen to agree with the empirical wall function implementation described in the ADPAC documentation [3]. In order to adequately model the boundary layer effects, wall functions were then set to always be on in the ADPAC solution routine, since a  $y^+$  value of ten does not produce adequate grid resolution near solid boundaries.

With an estimated  $y^+$  value of ten, the mesh expansion ratios were reduced to less than 1.35 in each coordinate direction. ADPAC generates a warning message when the expansion ratios are greater than 1.3, but after much experimentation, it seems that the solution will converge with expansion ratios less than 1.35. The IGV and rotor grid were then converted to a left-handed coordinate system for use in ADPAC. These

modifications completed our mesh for the TESCOM first stage IGV and rotor. The IGV and rotor grid can be seen in Figure 5. Again, for clarity, only the lines of constant radial location are shown.

### Detuned Grid Generation

Solving the detuned problem required a new mesh to be generated. ADPAC does not employ phase-lagged boundary conditions. Therefore, in order to model a detuned rotor blade, it was necessary to generate a computational mesh that modeled multiple blade passages. In the specific case of 10% alternate detuning, the circumferential span of two rotor passages (one narrow, one wide) exactly matches the circumferential span of two IGV passages. Therefore, two IGV passages were modeled as well as one narrow and one wide rotor passage.

To create the two different IGV passages, two identical grids were generated (the same as the one for the tuned case). One of these grids was shifted in the negative circumferential direction by one IGV blade passage ( $360^\circ/34 \text{ blades} = 10.588^\circ$ ). To generate a mesh for the narrow rotor passage, the inputs to TIGER™ were modified from the tuned rotor geometry by applying a 90% scaling factor in the circumferential direction. The geometry in the axial and radial directions was unchanged. For the wide rotor passage, a 110% scaling factor was applied in the circumferential direction to the tuned rotor geometry. Once again, the axial and radial geometry was unchanged. The wide passage was shifted in the negative circumferential direction by an amount equal to

one circumferential span of the narrow rotor passage ( $0.9*360^\circ/34$  blades =  $9.529^\circ$ ).

These four grids were converted to a left-handed coordinate system for use in ADPAC.

The two IGV passages together with the wide and narrow rotor passages describe a solution domain that repeats seventeen times around the circumference of the compressor geometry. This repeating geometry can be used by ADPAC to generate results for an alternately detuned rotor geometry. This computational mesh can be seen in Figure 6. Again, for clarity, only the lines of constant radial location are shown.

## VI. Methodology

### Tuned Rotor Case

The overall computational procedure consisted of preparing boundary condition and input files for a given mesh for a steady-state solution. The steady-state option is used to generate a first approximation to the solution. This steady-state solution is actually a quasi-steady solution that time-averages flow variable between the blade rows. The unsteady solution can then be started using the steady-state solution as an initial condition. The unsteady solution is then iterated until convergence is obtained. Overall convergence is determined by comparison of the inlet and outlet mass flow values.

The full geometry consists of three sections, the upstream inlet, the IGV, and the first rotor. The upstream inlet section of the flow path does not contain any blade geometry, therefore it is symmetric around the centerline of the flow path. This symmetry enabled the solution for the upstream inlet to be run in two dimensions, which greatly improved the computational time. The solution was started using standard day stagnation conditions at the inlet (for both the tuned and detuned cases), and all walls were considered no-slip boundary conditions in order to generate the proper boundary layer growth. This two-dimensional solution produced a pressure and temperature profile at the exit of the upstream inlet. This profile could be used as the inlet condition for the IGV and rotor grid. This upstream inlet produced an inlet Mach number to the IGV of approximately 0.224. This solution of the upstream inlet was used for both the tuned and detuned cases.

For the tuned rotor case, the original computational mesh contained two blocks, one for the IGV passage and one for the rotor passage. To generate the appropriate boundary conditions, a utility called PATCHFINDER (included with ADPAC) was run and a boundary data file was generated. This file was modified to fit our problem precisely. An input file was also created that dictated the rotational speed of the rotor, the number of iterations to perform, the CFL number, etc. These two files were specific to a steady-state calculation.

To determine the operating condition, the rotor rotational speed was obtained from TESCOM experimental data [14]. The point selected was one of maximum stage efficiency at 100% corrected speed. This data also included a mass flow rate, which was used for later comparisons. ADPAC requires an exit static pressure ratio to be specified for a steady-state solution. To determine what pressure ratio should be used, a compressor map was generated for the tuned geometry. This compressor map and efficiency plot can be seen in Figures 7 and 8.

It was decided that the operating point would be located near the peak efficiency point. As can be seen from Figures 7 and 8, this point is located at an exit static pressure ratio of 1.35. However, in order to allow for some stall margin, the operating point was chosen to be at an exit pressure ratio of 1.3. This choice allowed for some stall margin, as points past 1.35 were in the stall region (the steady-state solution diverged). This choice does not reduce the efficiency very much. The mass flow rate for this point is 30.522 lb<sub>m</sub>/s. This value is not equal to the mass flow rate given in the TESCOM data report (24.5 lb<sub>m</sub>/s), but it is of a similar magnitude.

The steady-state solution was set up to use three levels of multi-grid. A solution is first obtained on the coarsest level. This coarse solution is then interpolated to the next finest mesh level and a solution is obtained there. This solution is then interpolated to the finest mesh level and the final steady-state solution is obtained. For the tuned case, each of the coarser mesh levels was run for 1000 iterations, and the fine mesh for approximately 400 iterations. At this point the root mean square of the residuals had decreased by about six orders of magnitude. This convergence plot can be seen in Figure 9.

An oddity of ADPAC is that if a converged solution is continually iterated, then instabilities will develop and the solution will diverge. This divergence happens in an abrupt fashion, and that is why the fine mesh steady-state solution was not iterated for any longer than it was. This behavior has been observed and was documented in initial ADPAC testing.

At the completion of a run, ADPAC generates a restart file that can be used to start a solution again at a later time. The restart file generated by the steady-state solution was used to start an unsteady solution. An unsteady boundary data file and input file were generated and the restart file from the steady-state solution was used as the initial condition for the unsteady solution.

The unsteady solution algorithm used in ADPAC is an implicit procedure. This means that the solution is obtained for all points in the solution domain simultaneously at each global (physical) time step before moving on to the next global time step. The time-marching algorithm is comprised of computational time steps that are embedded in each global (physical) time step. The user sets the maximum number of computational time

steps that are taken inside each global time step. For our calculations this value was set to 20 iterations. Also, the user can also specify a residual convergence level for each global time step. If the base ten logarithm of the root mean square of the residuals becomes less than this value before the maximum number of inner iterations is reached, then the solution is deemed to be converged at that global time step and the solution advances to the next global time step. For our calculations, this value was set to -6.5. Setting the maximum number of iterations and the convergence level to appropriate values can significantly improve computational time, especially on the coarser mesh levels.

The unsteady solution does not use a full multi-grid startup routine as the steady-state solution did, since a solution already exists on the finest mesh level from the steady-state restart file. However, it has been shown [3] that by interpolating the steady-state fine mesh solution back to the next coarsest mesh level and iterating on that mesh level first, convergence can be significantly accelerated. Therefore, this procedure was followed for the unsteady solution.

From prior research with ADPAC, it was known that a typical unsteady solution generally takes about one rotor revolution in time to converge. In the global sense, solution convergence is determined when the inlet mass flow value approaches the same value as the outlet mass flow (at least in a periodic sense), and the residuals have been reduced by approximately five orders of magnitude. Mass flow values are output by ADPAC, and the user can examine these values to determine whether convergence has been achieved.

A convergence plot of the tuned unsteady solution can be seen in Figure 10. The inlet mass flow rate has approached asymptotically the mean of the outlet mass flow rate, which exhibits periodic behavior. The mass flow rate at this point is approximately 25.792 lb<sub>m</sub>/s, which compares favorably with the value of 24.554 lb<sub>m</sub>/s given in the TESCOM data report.

#### Detuned Rotor Case

For the detuned rotor geometry, the procedure was similar to the tuned case. Once again, an operating point had to be determined by using the steady-state solution. A compressor map was not generated, as the exit static pressure ratio was altered until the mass flow rate at convergence of the steady-state solution was the same as the mass flow rate at convergence for the steady-state tuned case (the mass flow rates matched within 1.5%). This equality of mass flow rates insured that we were operating at approximately the same Reynolds number. An exit pressure ratio of 1.2 (as compared to 1.3) was needed to match these mass flow rates. A convergence plot of the steady-state detuned case can be seen in Figure 11. This steady-state solution was used to start an unsteady calculation on the detuned geometry. The detuned case was run until convergence was achieved, the same as for the tuned case.

All computations were performed on a cluster of five desktop PCs running under the Linux operating system. Parallel capability was obtained by using the MPI message-passing interface. The various machines were either Pentium II or Pentium III architecture, ranging in clock speed from 350 MHz to 1 GHz. Each machine contained at least 256 MB of RAM. These machines communicated with one another through a 100-Mbit Ethernet connection.

## VII. Results

The goal of this research was to determine the effects of detuning on high-cycle fatigue in turbomachinery blades. This requires an accurate analysis of the loading on the blades to be performed. The loading on the blade is due to a pressure distribution and viscous forces acting on the surface of the blades that gives rise to the six forces and moments contained in a 3-D solution. In order to facilitate this discussion of a detuned case versus a tuned case, Figure 12 shows a schematic of the method of detuning that was used, where the spacing differences are exaggerated for the sake of emphasis. Figure 12 only shows the relative positioning of each blade in the computational mesh so the reader can identify where the various blades are located. It is not representative of the actual blade shapes used. Also, each IGV and rotor blade is labeled either A or B. These blades are referred to as such throughout this analysis.

### Grid Sensitivity

In any CFD calculation, it is important to verify the sensitivity of the solution to different grid sizes. For this research a grid-sensitivity study was performed by using the multi-grid meshes generated by ADPAC and examining the forces and moments on the blades in a steady-state calculation. This technique is similar to a grid-independence study. Figure 13 shows a portion of the study, as the results for the other blades are essentially identical. The tuned case shows that at the finest mesh level, there is little or no sensitivity to grid size, which adds confidence to the results at the finest mesh level. Unfortunately, the detuned geometry shows that grid independence may not be

established, although only one force and one moment show this, so it may still be an acceptable mesh to use.

### Steady-State Results

In order to generate an accurate unsteady solution, it is beneficial in terms of computational time to generate a converged steady-state solution to be used as a starting point for future unsteady calculations. The steady-state  $C_p$  distribution shows the average pressure distribution across the surface of the IGV. Figure 14 shows this distribution over the IGV for the tuned case at three radial locations. The jagged quality of the plot at the leading and trailing edge is due to poor grid resolution in that region. The mean appears to be around zero (as we would expect for a symmetric IGV), but the  $C_p$  profile at the tip is very strange, most likely due to boundary layer effects. Figures 15 and 16 show the same steady-state profile for the detuned case. These figures are practically identical to that for the tuned case, indicating that detuning had little effect on the steady-state performance of the IGV (see Table 2, later).

Figure 17 shows the steady-state  $C_p$  profile over the tuned rotor at three radial locations. There is also a jagged quality at the edges of the profile, once again due to poor grid resolution at the leading and trailing edges. The highly curved nature of these profiles is due to the presence of a shock located at about 30 percent chord. This shock is not being accurately defined in this region (it is “smeared out”), due to poor grid resolution in the axial direction. Figures 18 and 19 show the  $C_p$  profile for the two detuned rotor blades. For rotor A at the mean radius the shock has shifted slightly

towards the mid-chord of the rotor blade, and for rotor B, it has shifted slightly upstream to about 20 percent chord. From Figure 19 it can also be seen that rotor B may be operating off-design. This can be seen due to the crossing of the pressure and suction surface traces at the mean radius. This is reasonable to expect, as this IGV and rotor geometry was not designed for detuning. This moving of the shock should be expected in the detuned case as detuning creates passages of unequal width. In a narrow passage the point where the shock from a neighboring blade impinges on another blade will be farther upstream, and for a wider passage it will be farther downstream.

Figure 20 shows the steady-state Mach number contours for both the tuned and detuned cases. There is a discontinuity between the IGV and rotor regions because at that interface, the reference frame shifts from the absolute frame to the relative frame. Also, the rotor blade can still be seen in the contour plot, because in the relative frame, the observer is effectively “sitting” on the rotor blade, and therefore appears not to have moved. The flow reaccelerates after it passes through the shock attached to the leading edge of the rotor, and that there is another shock further down in the passage. This two-shock system was also shown by Car and Puterbaugh [11]. Figure 20 indicates the source of the highly curved nature of the steady-state rotor  $C_p$  profiles.

It can also be seen from the contour legend in Figure 20 (both tuned and detuned cases) that there may be a region of flow that is trying to separate near the trailing edge of the blade. At that point, the Mach number is very low, and therefore some separation would be expected to occur near this point somewhere in the flow field. Upon investigation of a contour plot of axial velocity (Figure 21), this region of separation was found to be near the hub at the trailing edge of the rotor. Figure 21 shows this aspect of

the flow field for both the tuned and detuned cases. The separation occurs (in both the tuned and detuned cases) very near the hub at the trailing edge of the rotor (where axial velocity becomes negative). Modern blade designs that have a low aspect ratio and high loading typically exhibit some small regions of separation, especially near the hub.

### Unsteady Results

The unsteady  $C_p$  profiles for the IGV are shown for the tuned and detuned cases in Figures 22 and 23 respectively. The time levels shown represent one blade passage for the tuned case (ensuring that periodicity has been achieved), and two full blade passages in the detuned case (also ensuring periodicity). For the tuned case, the first time level ( $t/T=0$ ) is defined as when the trailing edge of the IGV and the leading edge of the rotor are aligned in the axial direction. For the detuned case, the first time level ( $t/T=0$ ) is defined as when the outer blades (IGV B and rotor B) are perfectly aligned (see Figure 12). Only IGV A is included for the detuned case, as IGV B has a profile identical to IGV A (as expected). These plots show that the pressures over the IGV surfaces fluctuate in time. Also, there is a region of maximum pressure on either surface at about 96 percent chord. The pressure fluctuation shown is caused by the shock attached to the leading edge of the rotor blade passing the trailing edge of the IGV. When this shock passes, it generates a weak pressure fluctuation (much weaker than a shock) that passes upstream and impinges on the suction surface of the IGV. The suction surface of the IGV is defined as the side of first approach of the rotor. This pressure fluctuation then “releases” from the pressure surface of the IGV and moves on towards the next IGV.

Since this pressure fluctuation first impinges on the suction surface, the fluctuations should be larger on that surface, and that is exactly what Figures 22 and 23 show.

From Figures 22 and 23, it can also be seen that the pressure fluctuation travels from the trailing edge of the IGV towards the leading edge. Using the flow condition in this region, the distance between two peaks of the pressure wave and the rotational speed of the rotor, it was determined that this wave is an acoustic wave, traveling upstream. The point of maximum pressure is not exactly the same for the pressure and suction surfaces. The traveling waves along each surface are therefore slightly out of phase, owing to the difference in time necessary for the pressure fluctuation to move from one side of the IGV to the other.

Figures 22 and 23 also show that the pressure fluctuations seem to attenuate as they travel upstream. This should be expected since a small pressure fluctuation will do a small amount of work on the IGV (some small amount of energy will be generated). As the fluctuation travels upstream, the energy is acting over a larger and larger area and therefore as it moves toward the leading edge of the IGV there will be less and less energy to act over the surface of the IGV. The pressure surface shows a region (Figure 22) where the  $C_p$  profiles appear to "cross," and then expand slightly again as they travel downstream. This crossing occurs around 50 percent chord, and it may be caused by the fact that the 50 percent chord point is very near the point of maximum thickness on the blade, and the flow is accelerating slightly again around the IGV curvature toward the leading edge, causing the pressure fluctuations to be reduced.

Figure 23 shows the unsteady  $C_p$  profiles for the detuned case. They are very similar to the tuned case profiles, although the fluctuations are larger on both surfaces.

This owes to the fact that there is some non-uniformity already present in the geometry due to the detuning. The only real effect that detuning has had for these plots is that it has increased the magnitude of the pressure fluctuation on the IGV.

The pressure fluctuation on the IGV caused by the passing of the shock attached to the leading edge of the rotor can be seen in five time “snapshots” in Figure 24. This contour plot shows pressure contours at five time levels (normalized by the tuned one-blade-passage period). The pressure fluctuation can be seen traveling away from the rotor leading edge and moving upstream and impinging on the surface of the IGV. This pressure fluctuation is a very weak one, as can be seen from the contour legend.

The rotor unsteady  $C_p$  profiles are shown for the tuned and detuned cases in Figures 25-27. The first thing to note here is that there is very little fluctuation of the rotor pressures with time (more fluctuation on the pressure surface than the suction surface). This is due to the fact that there is no forcing function for the rotor coming from downstream blades as there is for the IGV. There is a forcing function for the rotor coming from the upstream IGV wake, but it obviously has only a very small effect on the surface pressures on the rotor blade. The similarity of the detuned pressure profiles to the tuned pressure profile over the rotor blade indicates that there is probably only a very small overall performance change across the rotor blade due to the aerodynamic detuning (more discussion on this follows).

Another important factor to consider when investigating unsteadiness is the amplitude of the fluctuations in any given property. The pressure fluctuations on the blades have some amplitude, and this amplitude was estimated (Figure 28) by taking half of the difference in the minimum and maximum pressures for the each surface at any

given point along the blades. This calculation generates an estimate for the amplitude of the fluctuation (the differencing removes the mean value). This calculation was conducted for both blade rows for the tuned and detuned cases. It is immediately apparent (Figure 28) that the magnitude of the fluctuations on the IGV is much greater than those on the rotor (this has already been shown with the  $C_p$  profiles). Also, there is a peak in the amplitude of the fluctuations near the trailing edge of the IGV at about 90 percent chord, and a much smaller peak on the rotor at about 95 percent chord. These peaks are also present when the detuned case is run. Once again, for the rotor, there appears to be very little difference between the tuned and detuned cases, and for the IGV, the magnitude of the fluctuations are increased slightly from about 50 percent chord on downstream to the trailing edge.

A final factor to consider regarding the unsteady pressures on the blades is the loading profile. The loading is defined as the difference in the pressures on the suction surface and the pressure surface at any given time level. Plotting the loading value over the surface of the blade (Figures 29-31) can show where the location of maximum loading is. The loading for the IGV and rotor at the mean radius for both the tuned and detuned cases are shown in Figures 29-31. In all three cases the location of maximum loading on the IGV is not constant. It moves in time from about 65 percent chord to near the trailing edge and then back upstream until it repeats. If the point of maximum loading on Figure 29 (tuned case) is marked at each time step, the path traced is a single loop. This is due to the fact that the peak pressure point for the suction and pressure surfaces is not exactly at the same axial location along the blade surface (see Figures 22 and 23). This means that the pressure fluctuations along each surface are slightly out of

phase and therefore the location of maximum loading is a traveling wave along the surface of the IGV.

In the detuned case, IGV A and B have a nearly identical loading profile (as should be expected), and the location of maximum loading travels along the surface of the blade from about 50 percent chord to out near the trailing edge and then back upstream until it becomes periodic (see Figure 30). If the location of maximum loading in Figure 30 is marked at each time step, the path traced appears to be a smaller loop folded inside of a larger loop. These two loops are periodic. The smaller loop inside of the larger loop is most likely due to the fact that we have a narrow blade passage and a wide blade passage. Each of them form a single loop (just as in the tuned case) and they are linked when periodicity is achieved.

Figures 29 and 31 also include the unsteady loading on the rotor. As was seen in the rotor  $C_p$  profiles (Figures 25-27), there is very little variation in time of the loading on the rotor. The location of maximum pressure is approximately constant at about 10 percent chord (the spike near the leading edge is probably due to poor grid density and should not be considered). Detuning the rotor does shift the loading profile (Figure 31) toward the trailing edge, although the loading profile still has very little time dependency. Detuning does appear to influence the magnitude of the fluctuations, as they appear to be slightly larger than for the tuned case. This should be expected, as detuning has introduced some non-uniformity into the solution domain.

## Force and Moment Analysis

In determining what effect detuning has on the high-cycle fatigue problem, it is also necessary to examine the unsteady forces and moments on the blades. ADPAC generates a time history of the axial, radial and tangential forces and moments on each blade. These values represent the net force or moment on the blade in each direction, where the moment is calculated about the quarter-chord point.

The time histories of the blade forces and moments and their associated Fourier transforms are shown in Figures 32-35. For each of these plots, the tuned case time history and Fourier analysis are the upper two plots, blade A's time history and Fourier analysis are in the middle two plots, and blade B's time history and Fourier analysis are in the lower two plots. From the time histories, it is obvious that the tangential force varies much more than any other force, and the radial moment varies much more than any other moment. The tangential force is the force that deflects the blade around the compressor hub, and the radial moment is the moment that causes blades to twist. It can also be seen that when the rotor is detuned (Figures 34 and 35), the axial and radial forces do not change by any significant amount, and that the axial and tangential moments do not change very much either. Therefore the tangential force and radial moment are the two quantities that will be most useful in this analysis.

The time histories shown represent two full blade passages in both the tuned and detuned cases. This ensures that the entire solution domain has been swept through in time and periodicity has been achieved. Therefore, it is acceptable to take the discrete Fourier transform of these time histories to perform a frequency analysis.

From the time histories (Figures 32 and 34), detuning seems to reduce the mean of the tangential force on both the rotor and the IGV. It does not seem to have any effect on the mean of the radial moment (Figures 33 and 35). Upon examination of the Fourier transforms, it can be seen that in the tuned case the IGV exhibits the fundamental frequency that corresponds to the blade passing frequency. Detuning generates frequency energy in both the plus and minus half-harmonic side bands on the IGV. The 0.5 harmonic is due to the fact that the geometry now consists of a pair of 17-blade sets (one with wide spacing and one with narrow spacing), and the half-harmonic is at the frequency that would correspond to one blade passage of a 17-bladed geometry. The 1.5 harmonic could be due to the fact that detuning generates some of the frequency energy that would result from a rotor that had blades with spacing equal to the narrow passage spacing. This would effectively create a larger number of blades around the circumference, and hence a higher blade pass frequency. Since the level of detuning was fairly small, a lot of energy in the 1.5 harmonic side-band would not be expected.

In the Fourier analysis (Figures 34 and 35), the tuned rotor exhibits the fundamental frequency that corresponds to the blade pass frequency, and it also exhibits a second-order harmonic (of a smaller magnitude). Detuning seems to shift some of the frequency energy into the neighboring half-harmonic side-bands, both around the fundamental and around the second harmonic. It seems that there is less energy in the half-harmonic side-bands for the rotor than for the IGV (Figures 32 and 33), and this could be due to the fact that there is no downstream forcing function on the rotor as there is for the IGV.

Figures 36 and 37 present a summary of the Fourier analysis for both the IGV and the rotor, and the effects of detuning on the tangential force and radial moment. These charts plot the amplitude in the frequency domain of the first (fundamental) harmonic. It is clear from the charts that the fundamental of tangential forces on the IGV are reduced, but the fundamental of the radial moment has increased. Conversely, for the rotor, detuning has increased the fundamental of the tangential forces, and reduced the fundamental of the radial moment.

#### Overall Performance Analysis

From the  $C_p$  profiles, it was hypothesized that detuning had little effect on the overall performance of the IGV and first rotor. This was due to the fact that the  $C_p$  plots for the rotor changed very little from the tuned case to the detuned case. Table 2 summarizes the overall performance data along with the data given in the TESCOM data report [14].

Table 2. Overall Performance Comparison

	TESCOM	Tuned	% Diff.	Detuned	% Diff.
Mass Flow Rate ( $lb_m/s$ )	24.5	25.7	4.90	26.5	8.16
Rotor total pressure ratio	2.2631	2.199	2.83	2.159	4.60
Rotor isentropic efficiency	0.8893	0.875	1.61	0.8518	4.22

### **VIII. Conclusions and Recommendations**

The goal of this research was to investigate high-cycle fatigue effects in a detuned compressor rotor. It was hypothesized that detuning could result in a compressor that would maintain the overall performance of a tuned configuration while reducing high-cycle fatigue effects on the blades. Detuning effects have been investigated by many other researchers, but the author could not find any published papers where a three-dimensional computational model was used. The three-dimensional computation undertaken in this research provided an accurate prediction of the overall performance characteristics of a tuned compressor geometry as compared to experimental data.

The detuned geometry showed very similar performance characteristics to the tuned case (see Table 2) and to the experimental data. This provides reassurance that detuning has had very little effect on the overall performance of the compressor. The force and moment analysis of the detuned case showed that detuning could change the unsteady aerodynamic forces on the blades. On the IGV the tangential force was decreased while the radial moment was increased, and for the rotor, the tangential force was increased while the radial moment was decreased. This implies that detuning affects each problem differently, depending on the specific blade geometry and the flow regime under investigation. The frequency analysis also showed that there were some higher harmonics generated on the blades, which may or may not be beneficial to the high-cycle fatigue problem.

In conclusion, this research has shown that detuning has had very little overall effect on the performance characteristics of a compressor. It has also shown that

detuning could result in some reduction in the forced response of the blades. This reduction is a trade-off though, as decreasing a force or moment in one direction may increase one in another direction. This means that detuning should be applied to each problem individually, and a determination must be made about which force or moment should be reduced, and would it be acceptable for another to be increased as a result.

This research has also shown that further investigations of detuning are needed, as only one level of detuning was investigated here. Also, the grid independence study suggested that some of the forces and moments could be very sensitive to the mesh size, and therefore a more dense computational mesh should be applied to the problem to generate a potentially more accurate solution.

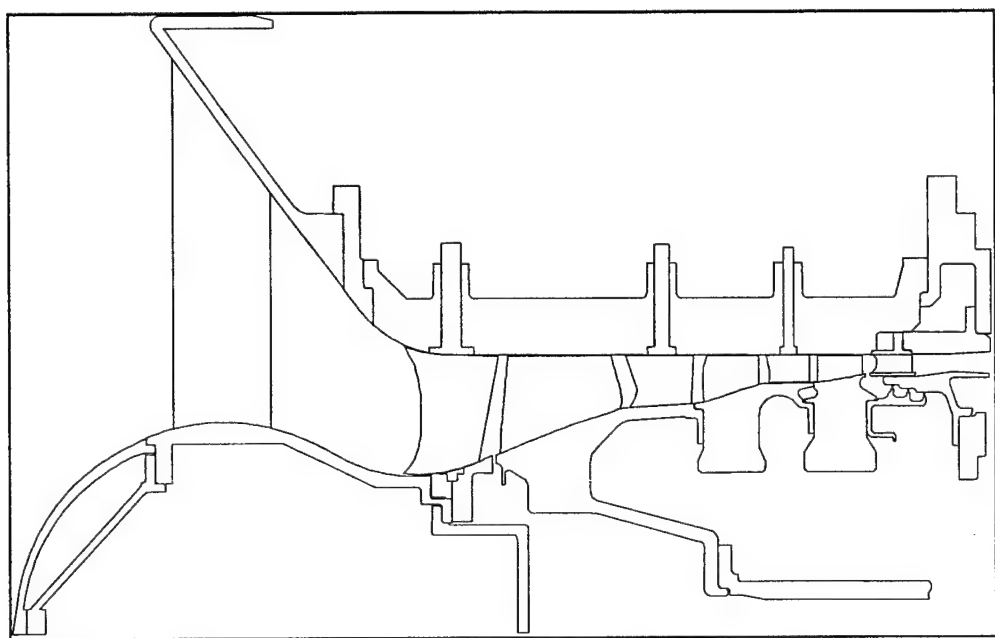


Figure 1. CARL TESCOM Three-Stage Compressor Rig (Meridional View)

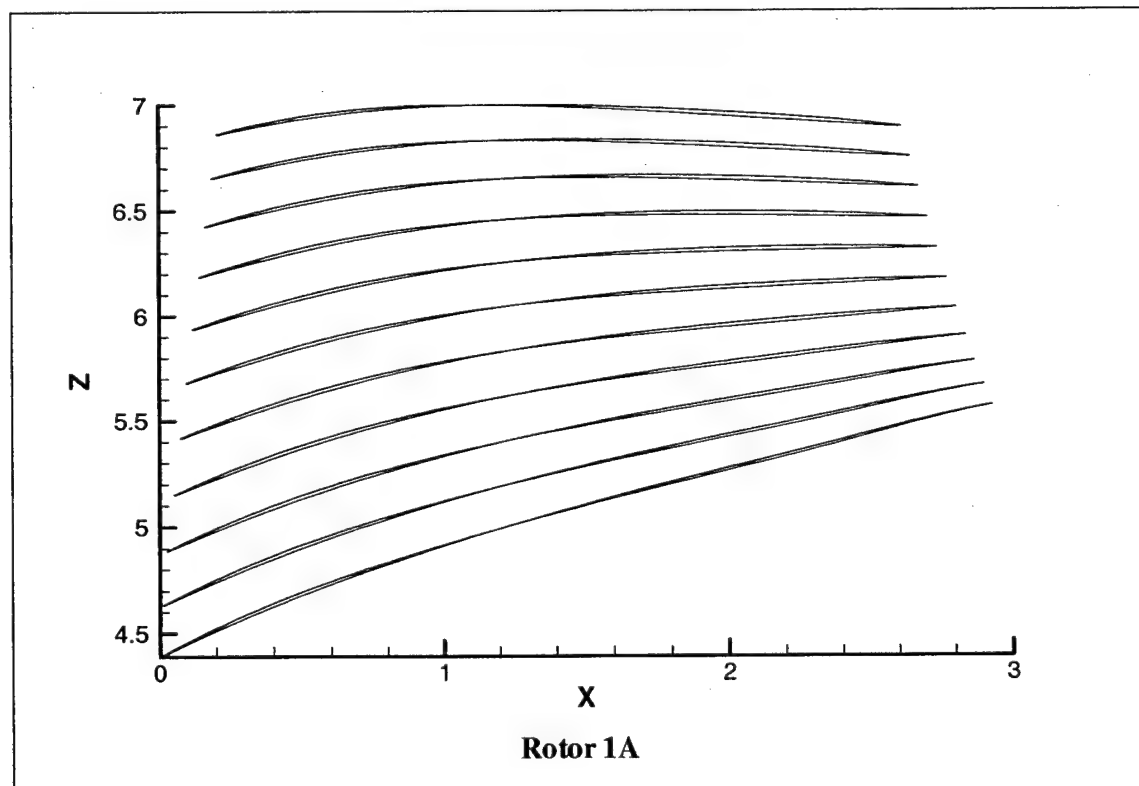
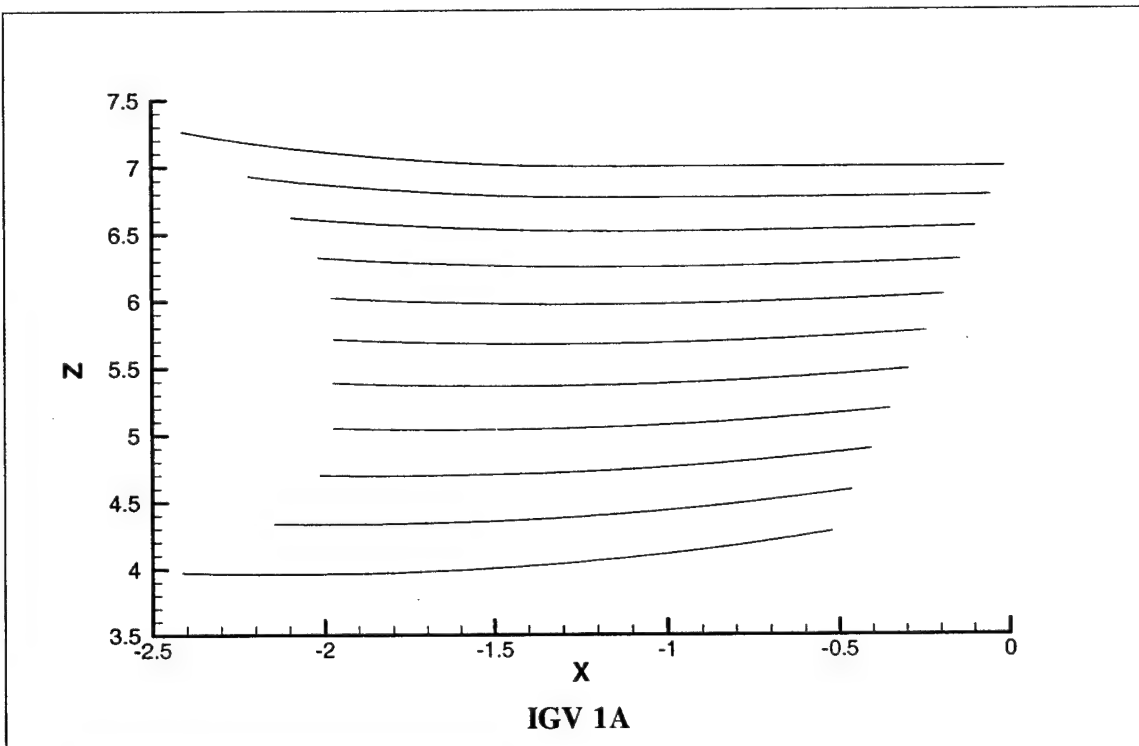


Figure 2. TESCOM Configuration 1A Streamline Geometry

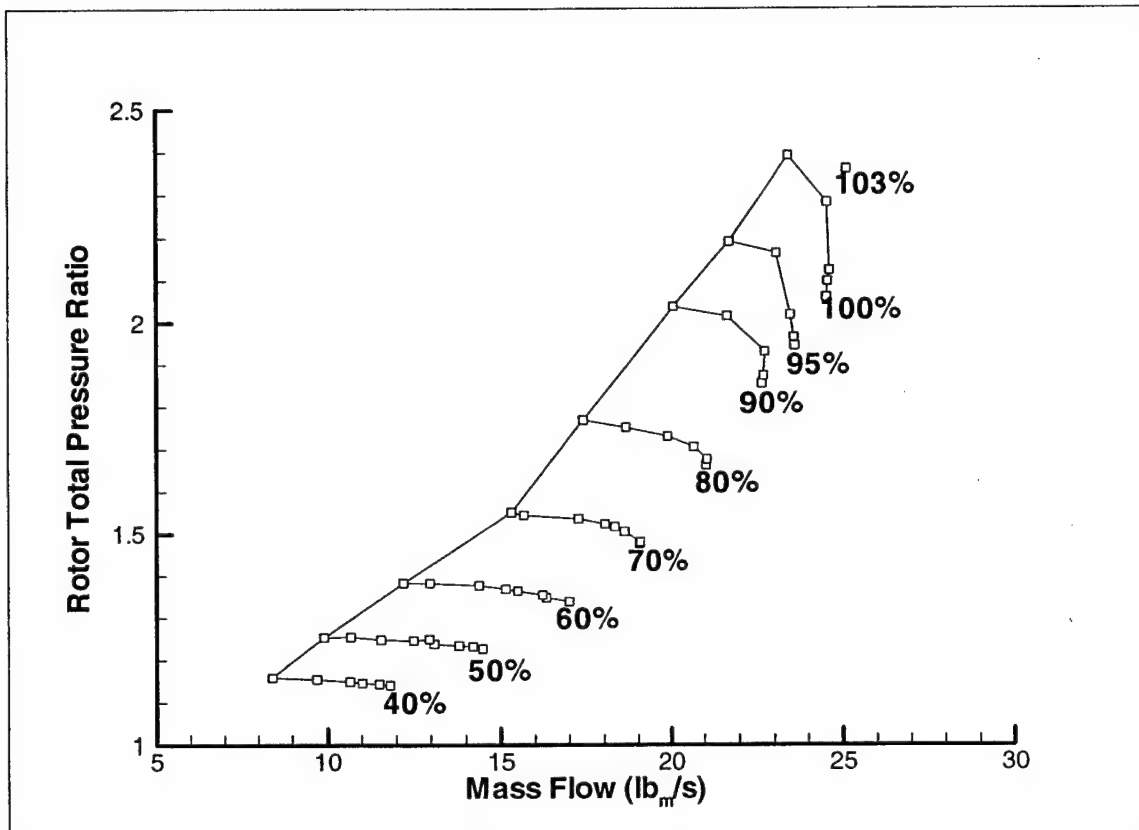


Figure 3. TESCOM Stage 1 (Configuration 1A) Performance Map

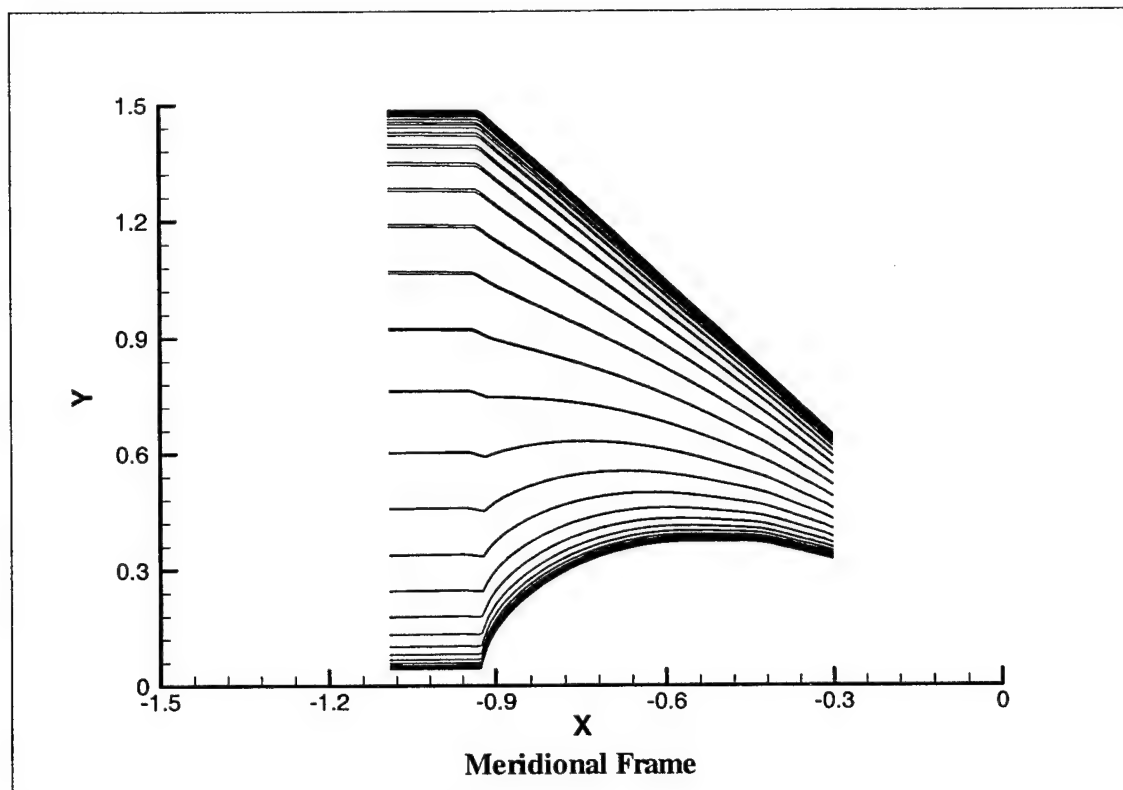
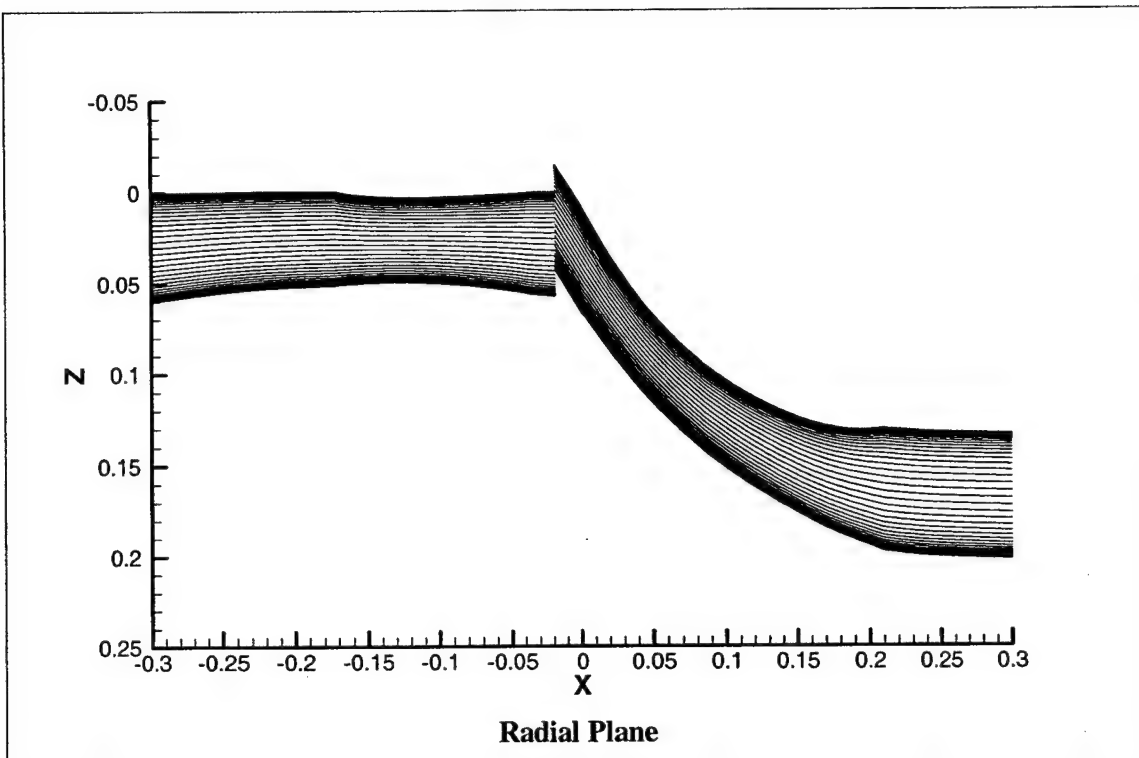
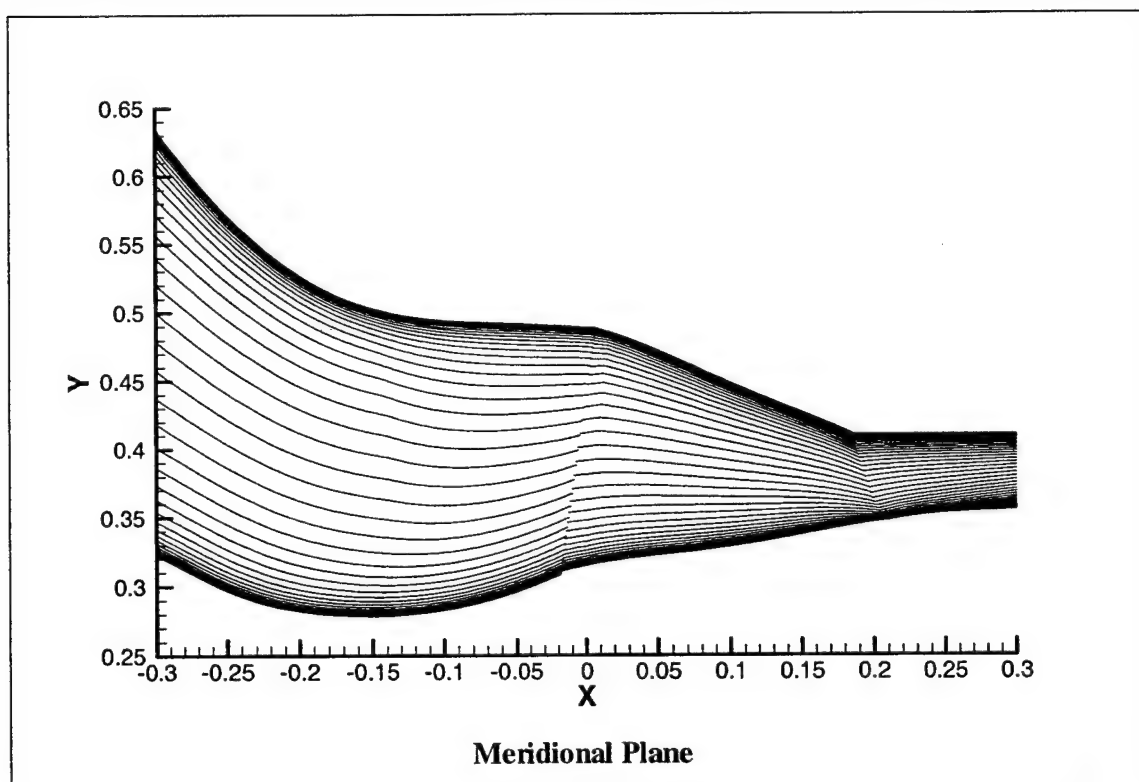


Figure 4. Upstream Inlet Computational Mesh (two-dimensional)



Radial Plane



Meridional Plane

Figure 5. Tuned Computational Mesh

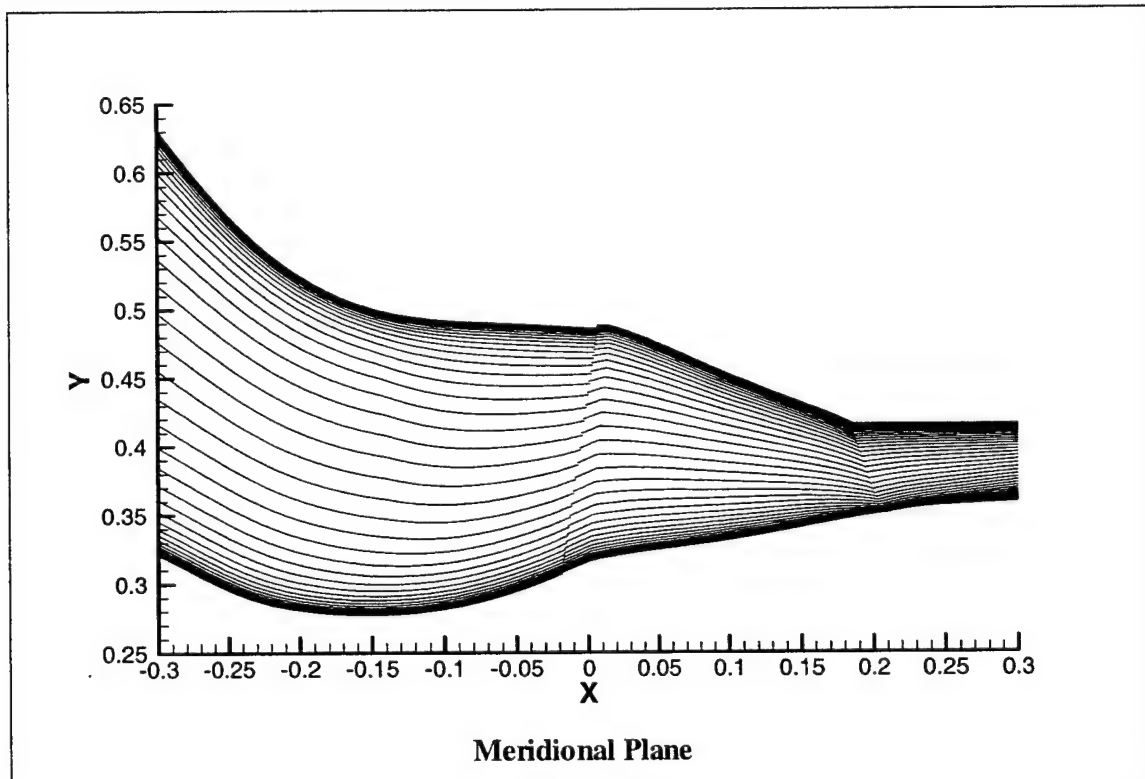
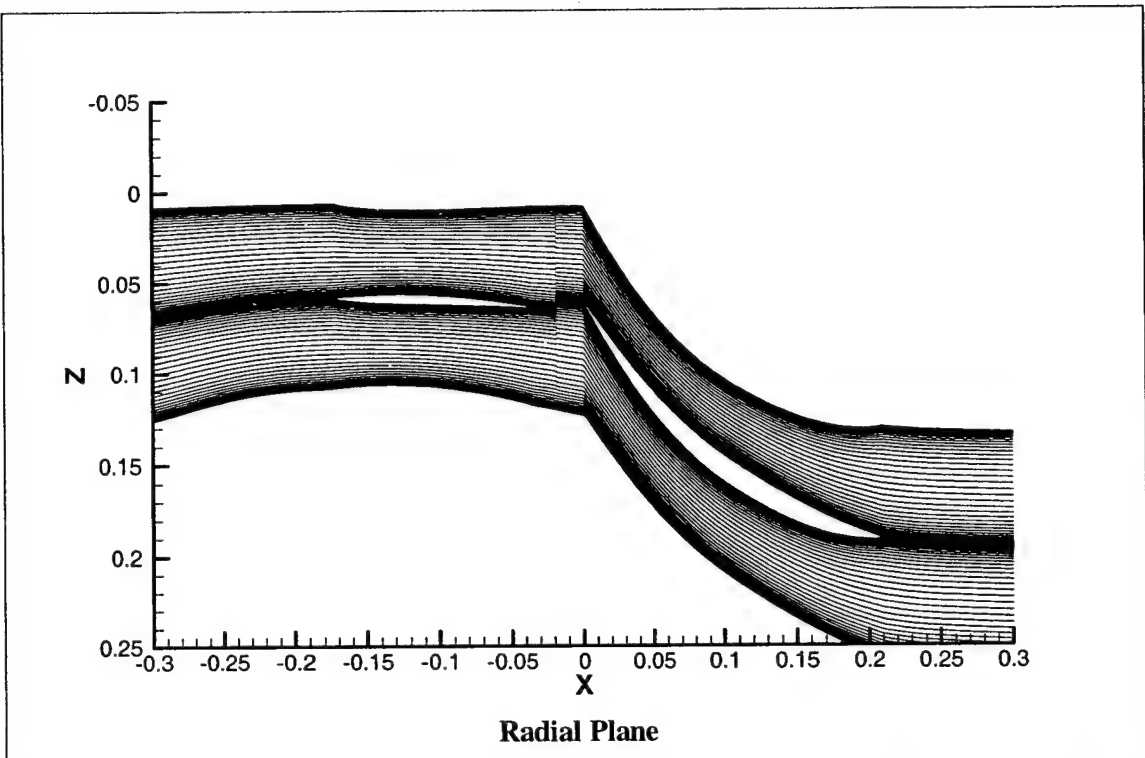


Figure 6. Detuned Computational Mesh

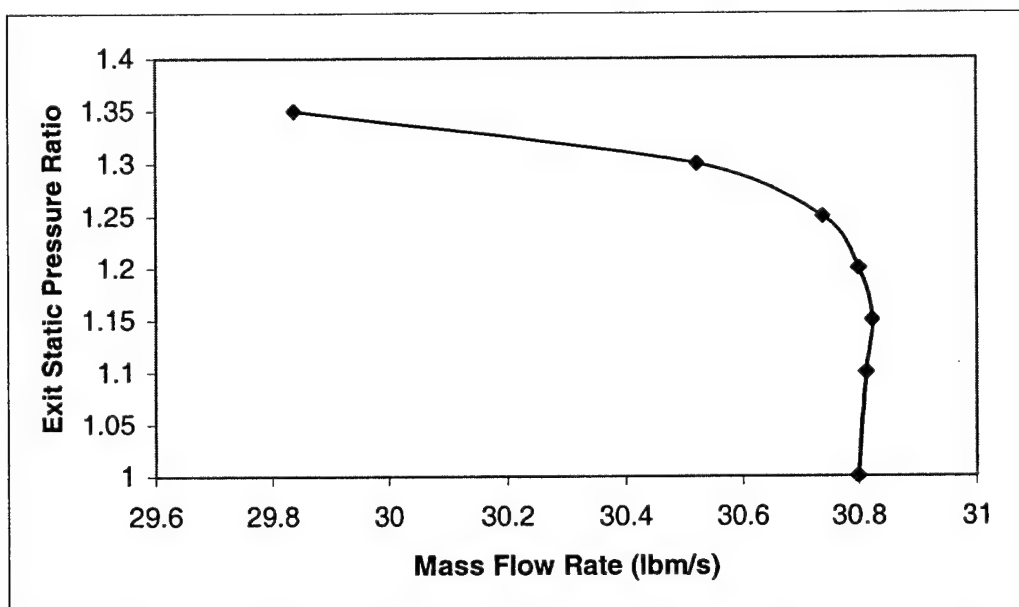


Figure 7. Tuned Compressor Map (Steady-State)

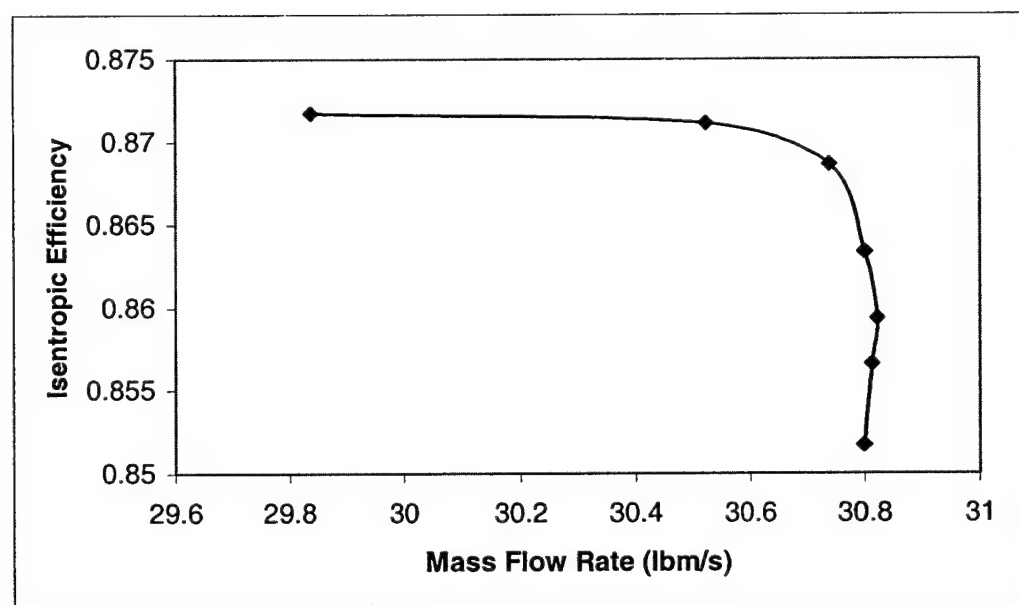


Figure 8. Tuned Efficiency Map (Steady-State)

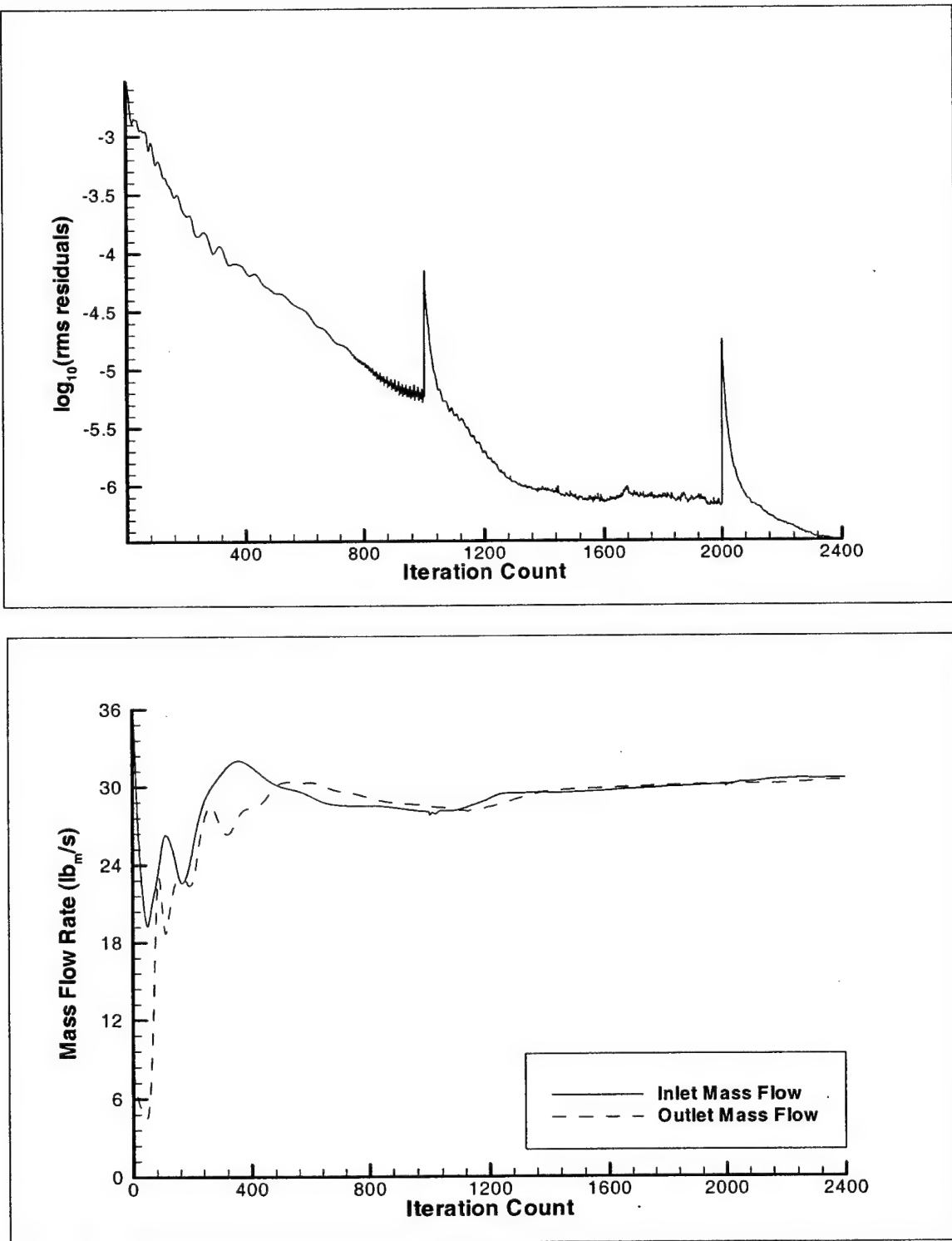


Figure 9. Tuned Steady-State Convergence Plot

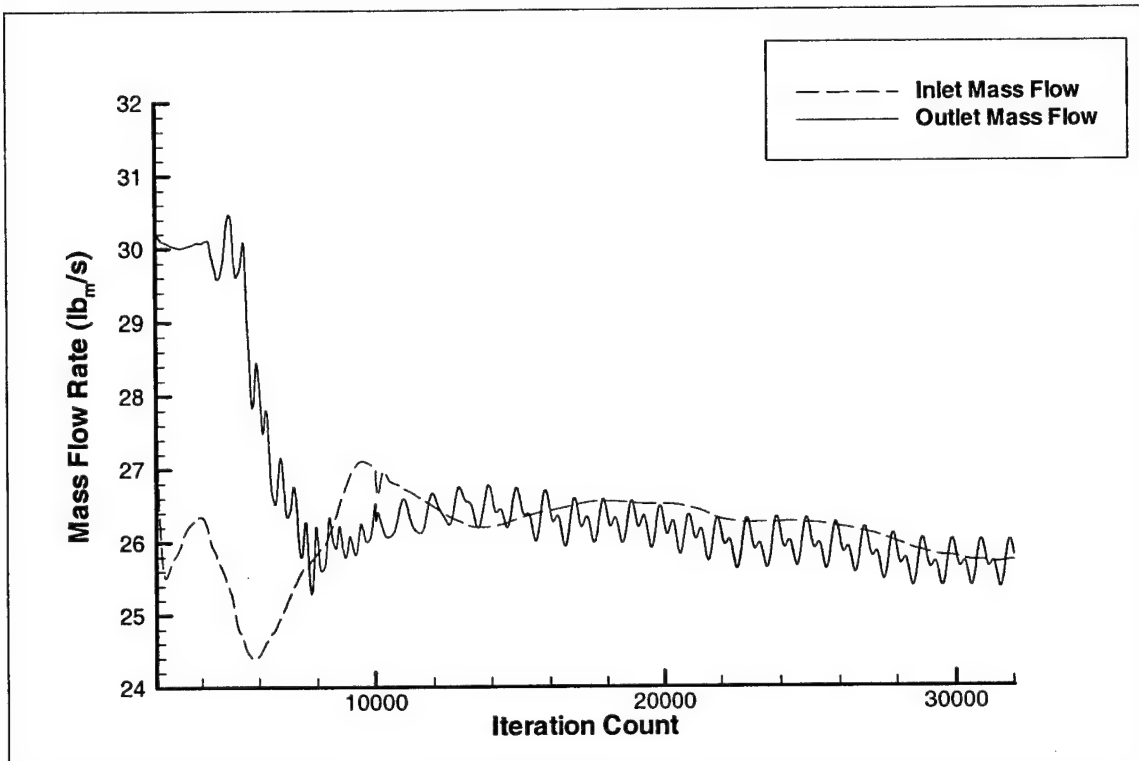


Figure 10. Tuned Unsteady Convergence Plot

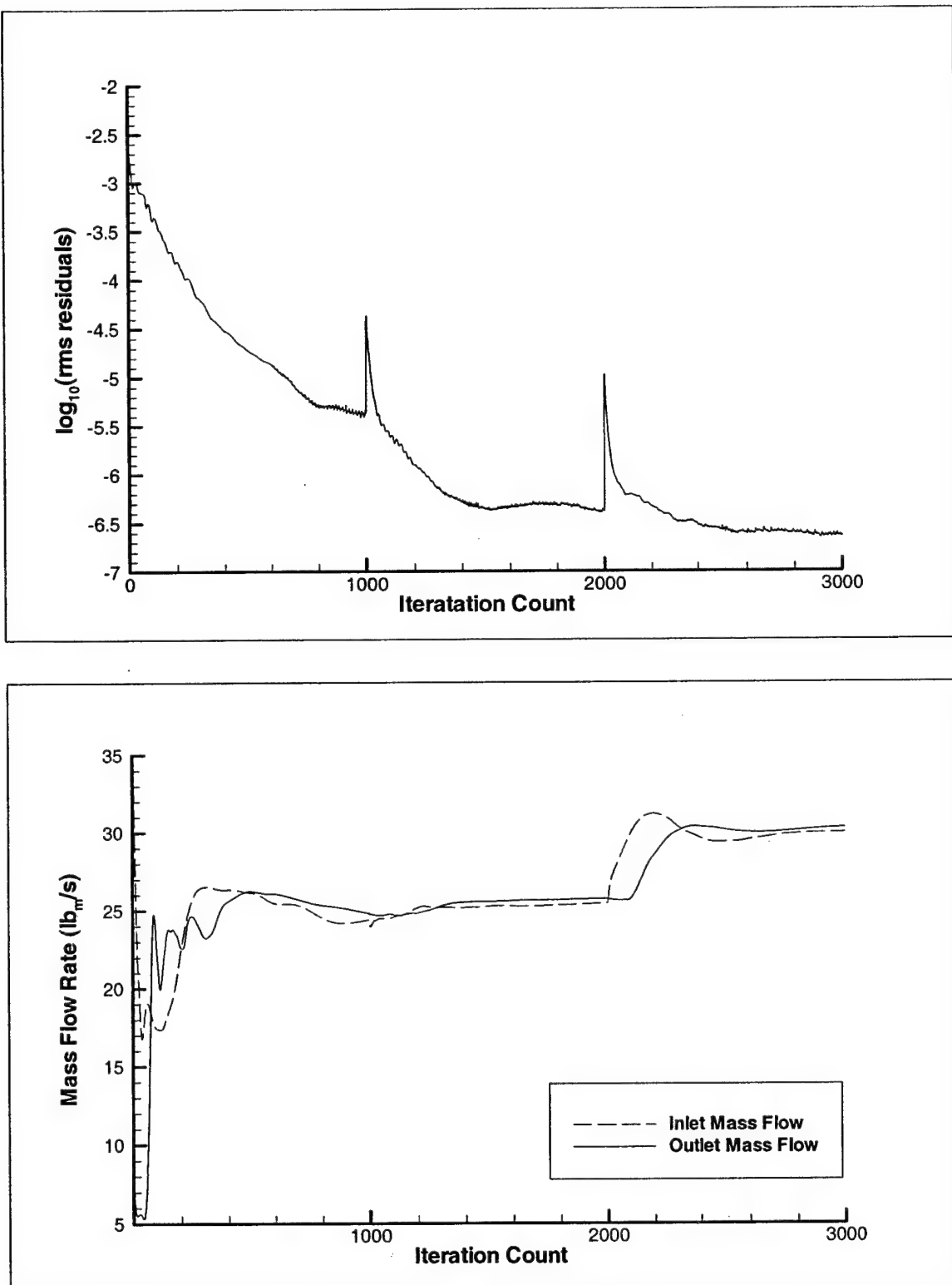


Figure 11. Detuned Steady-State Convergence Plot

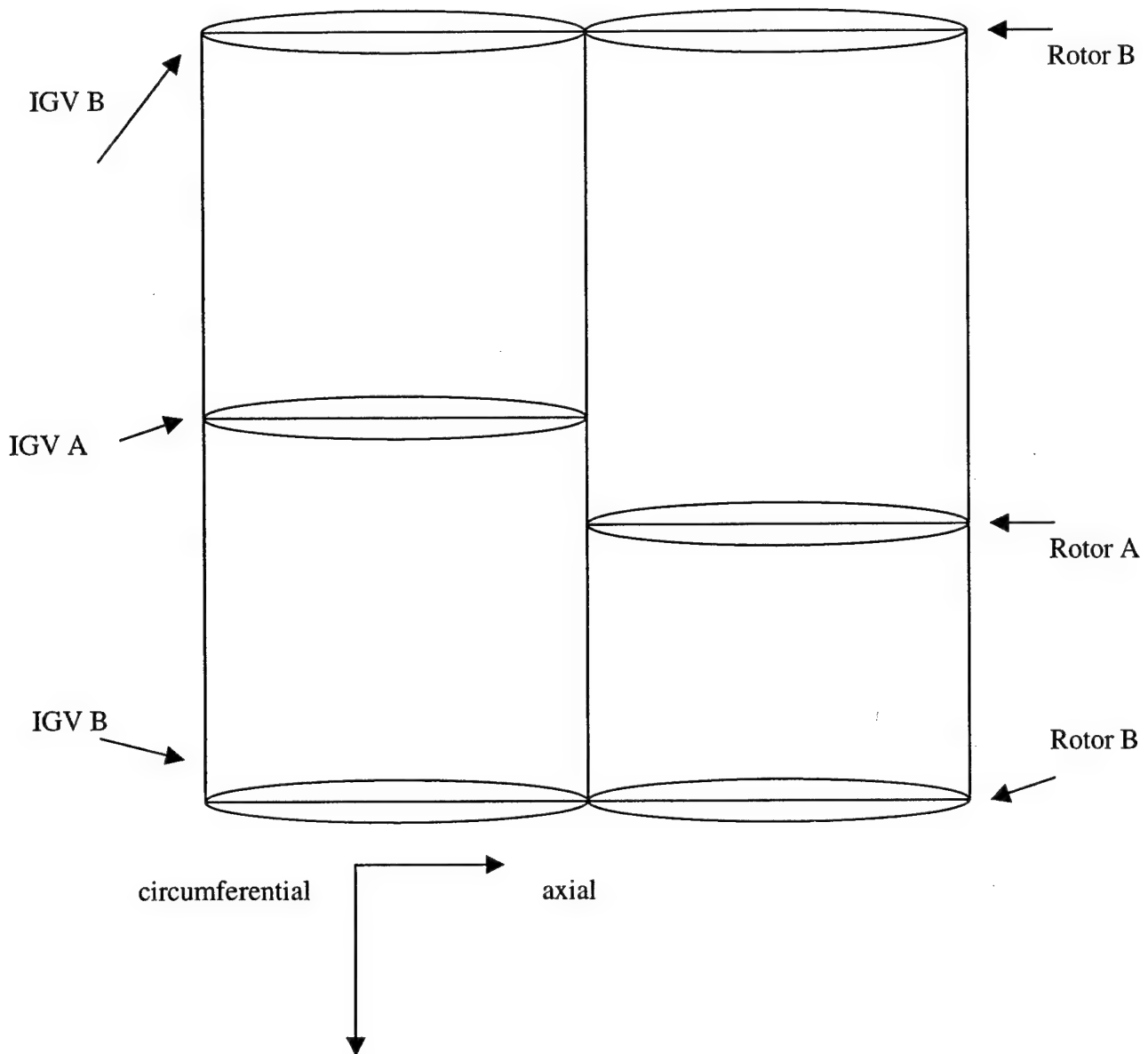


Figure 12. Schematic of the Detuned Geometry

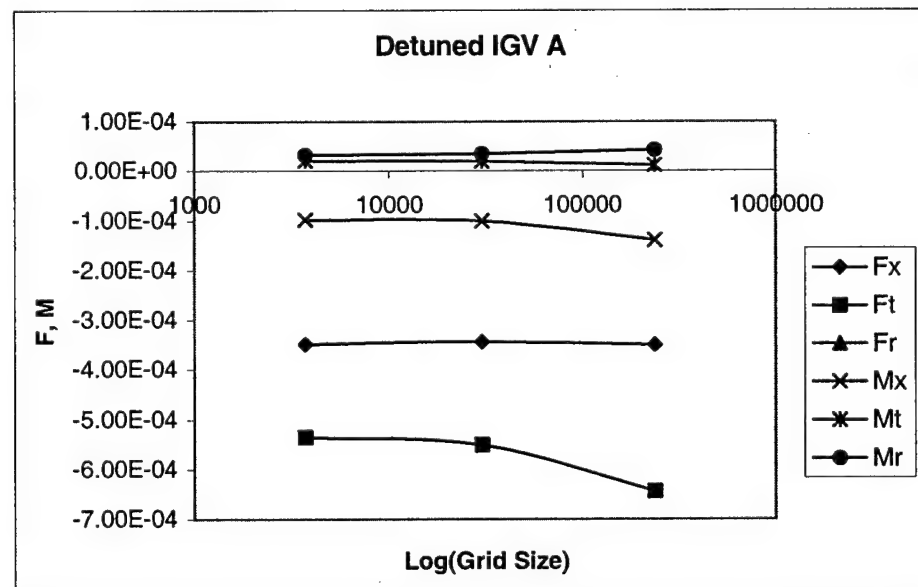
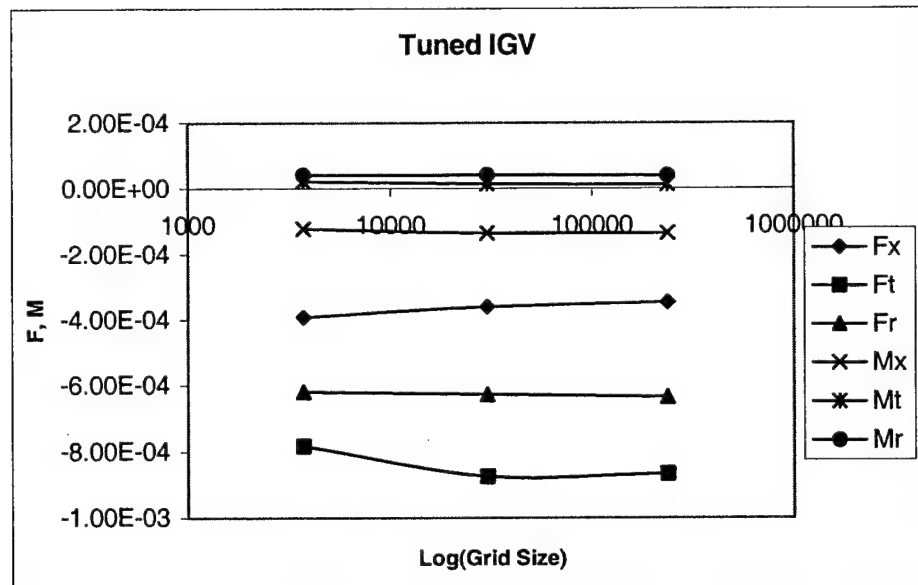


Figure 13. Grid Independence Study

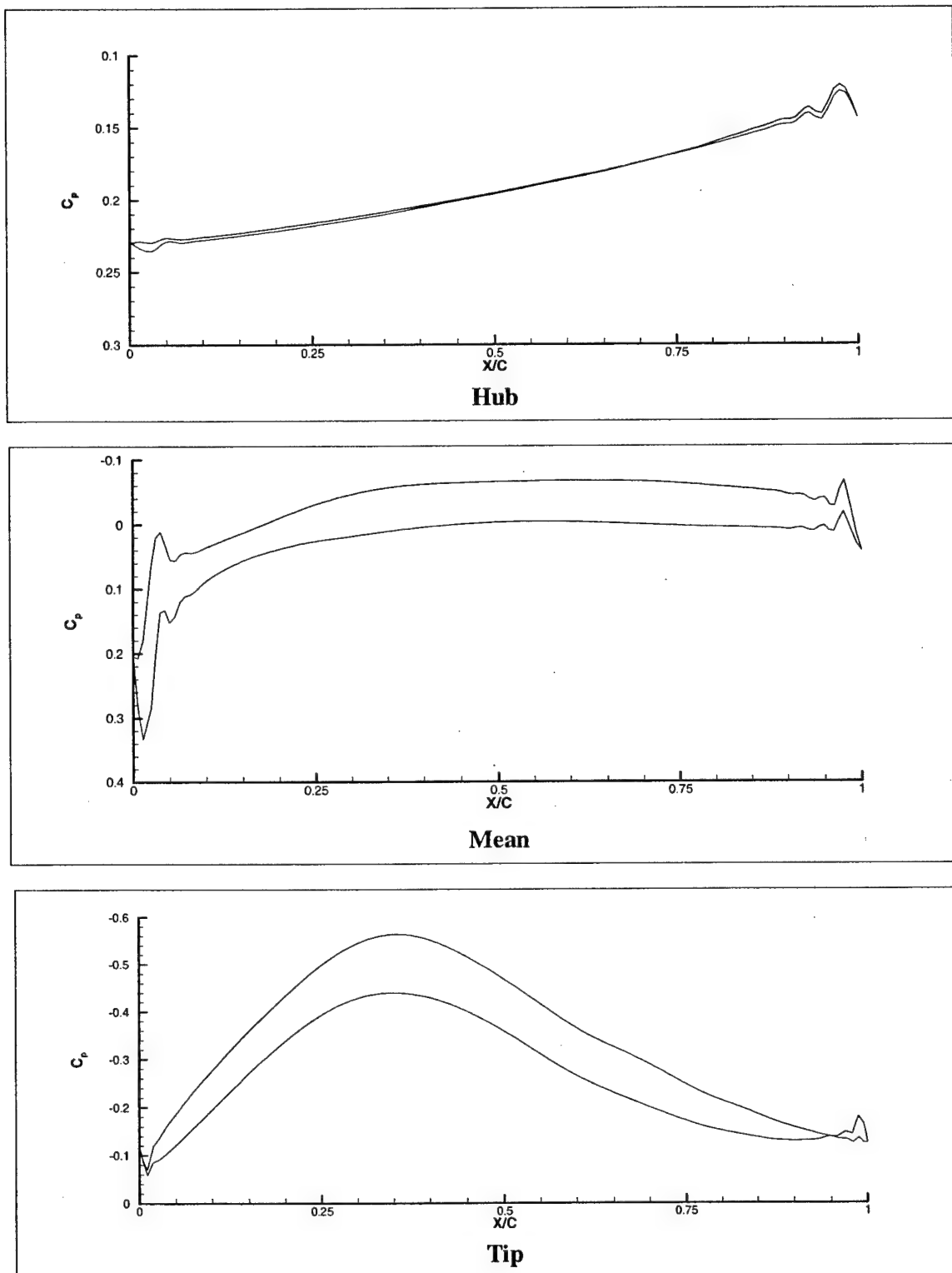


Figure 14. Tuned IGV  $C_p$  Steady-State Profiles

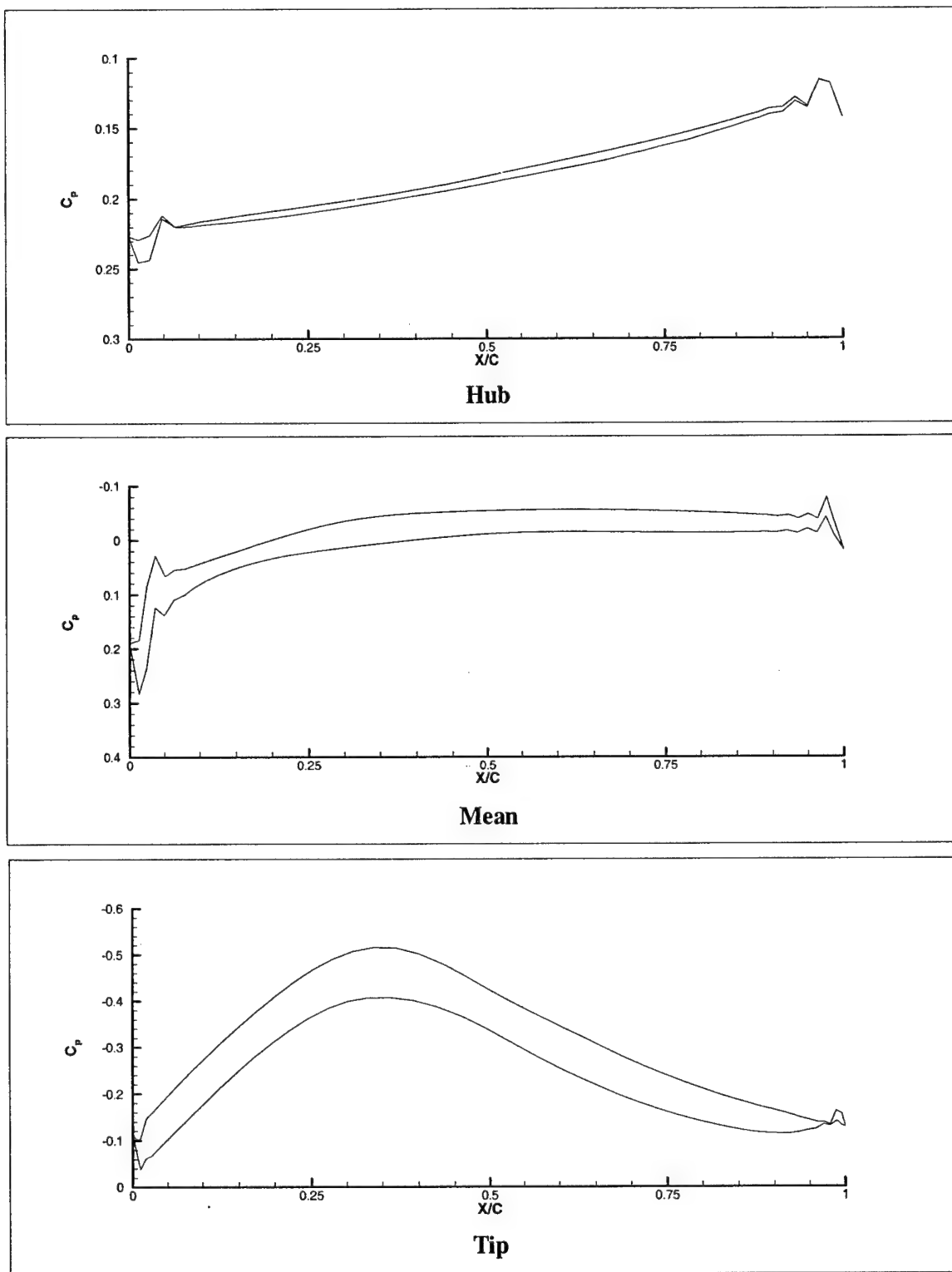


Figure 15. Detuned IGV A Steady-State  $C_p$  Profiles

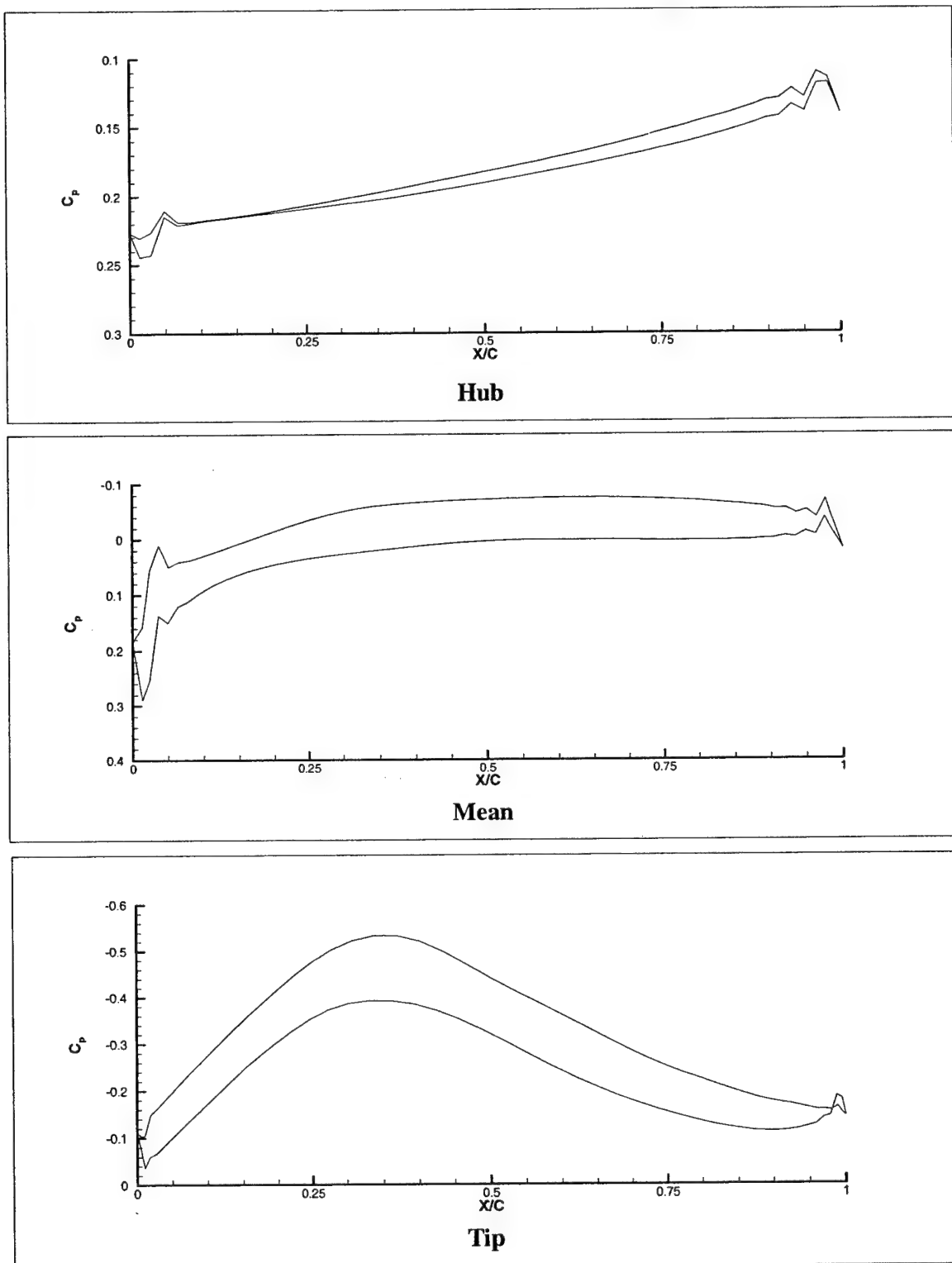


Figure 16. Detuned IGV B Steady-State  $C_p$  Profiles

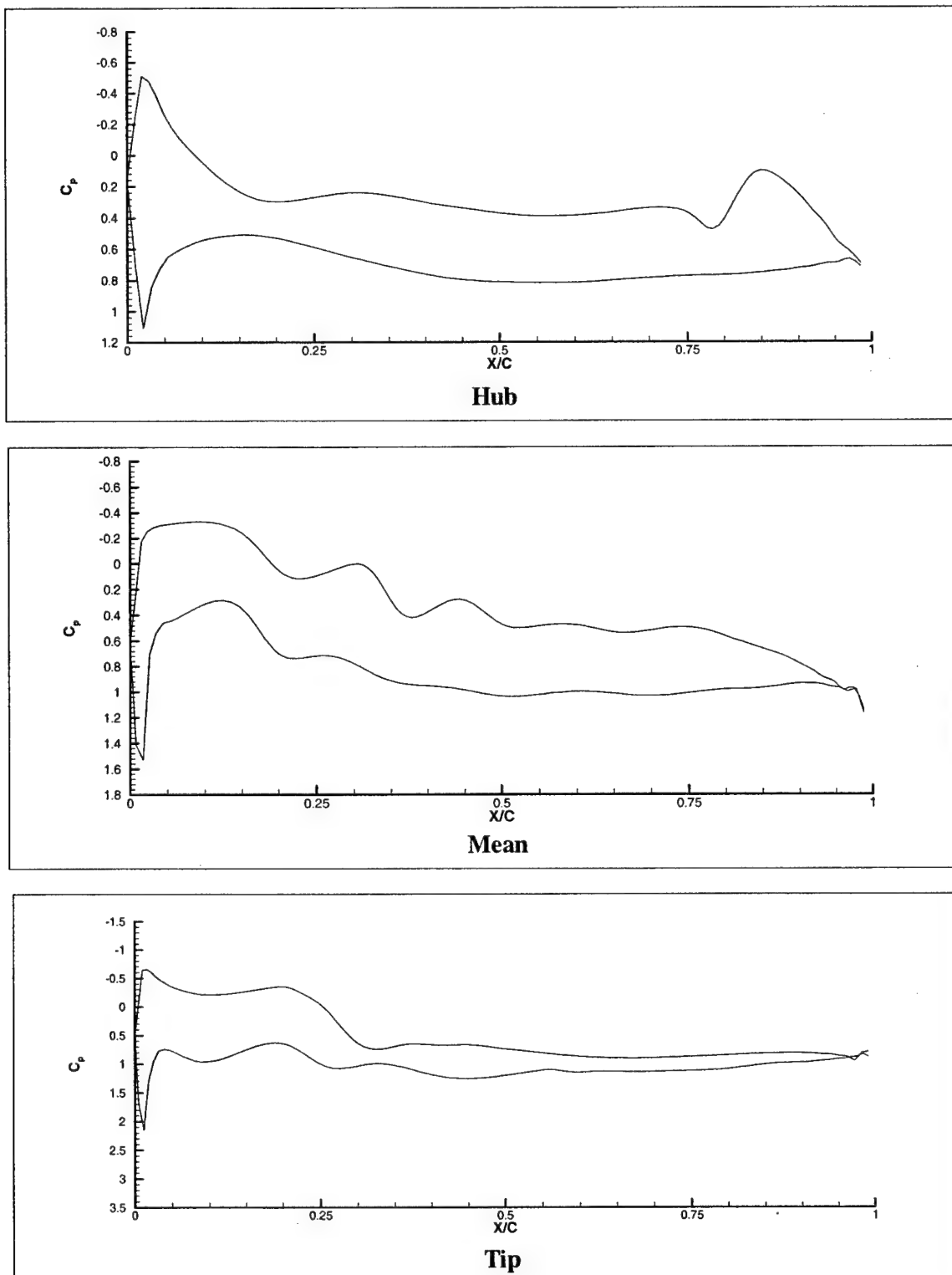


Figure 17. Tuned Rotor Steady-State  $C_p$  Profiles

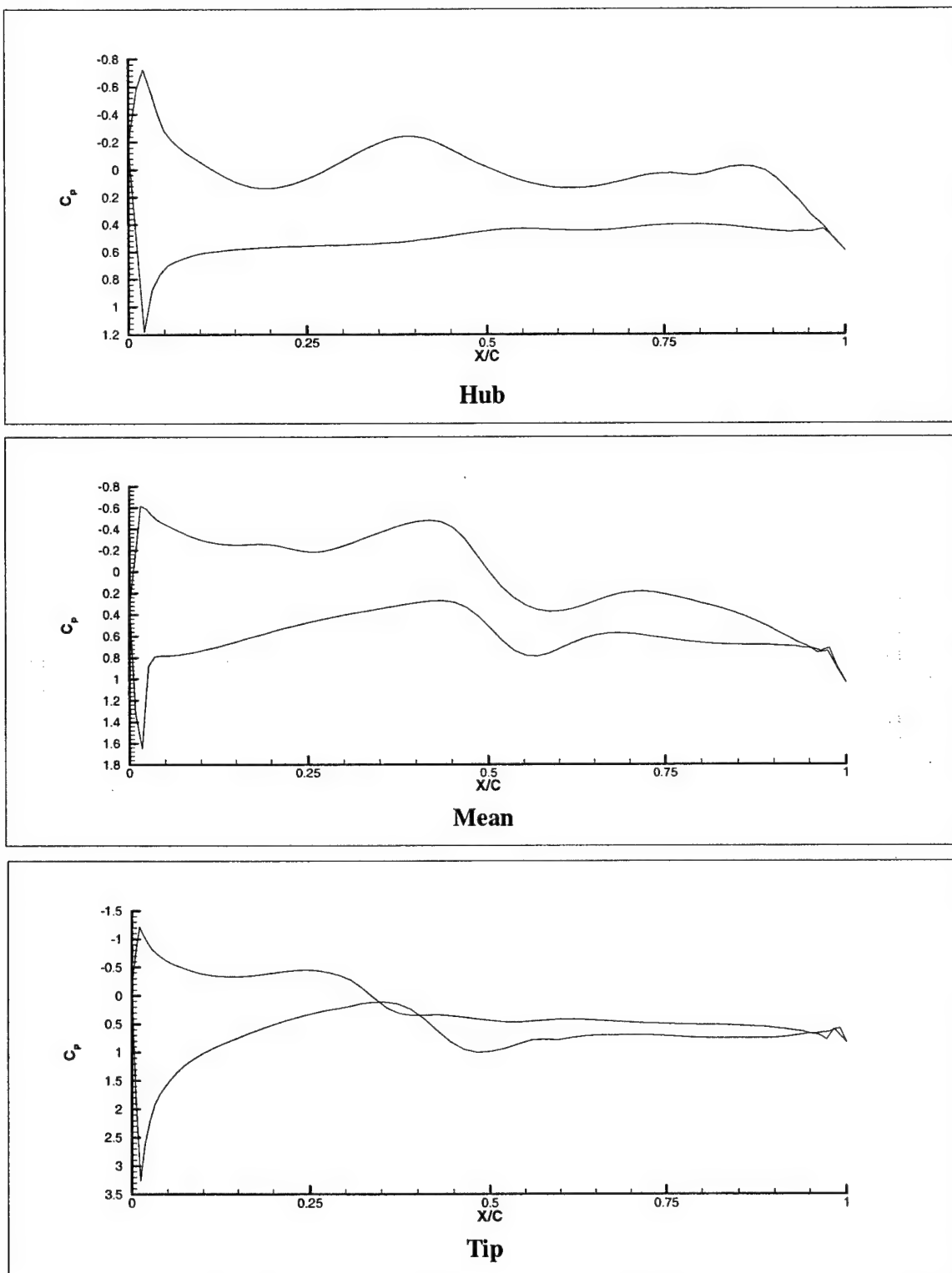


Figure 18. Detuned Rotor A Steady-State  $C_p$  Profiles

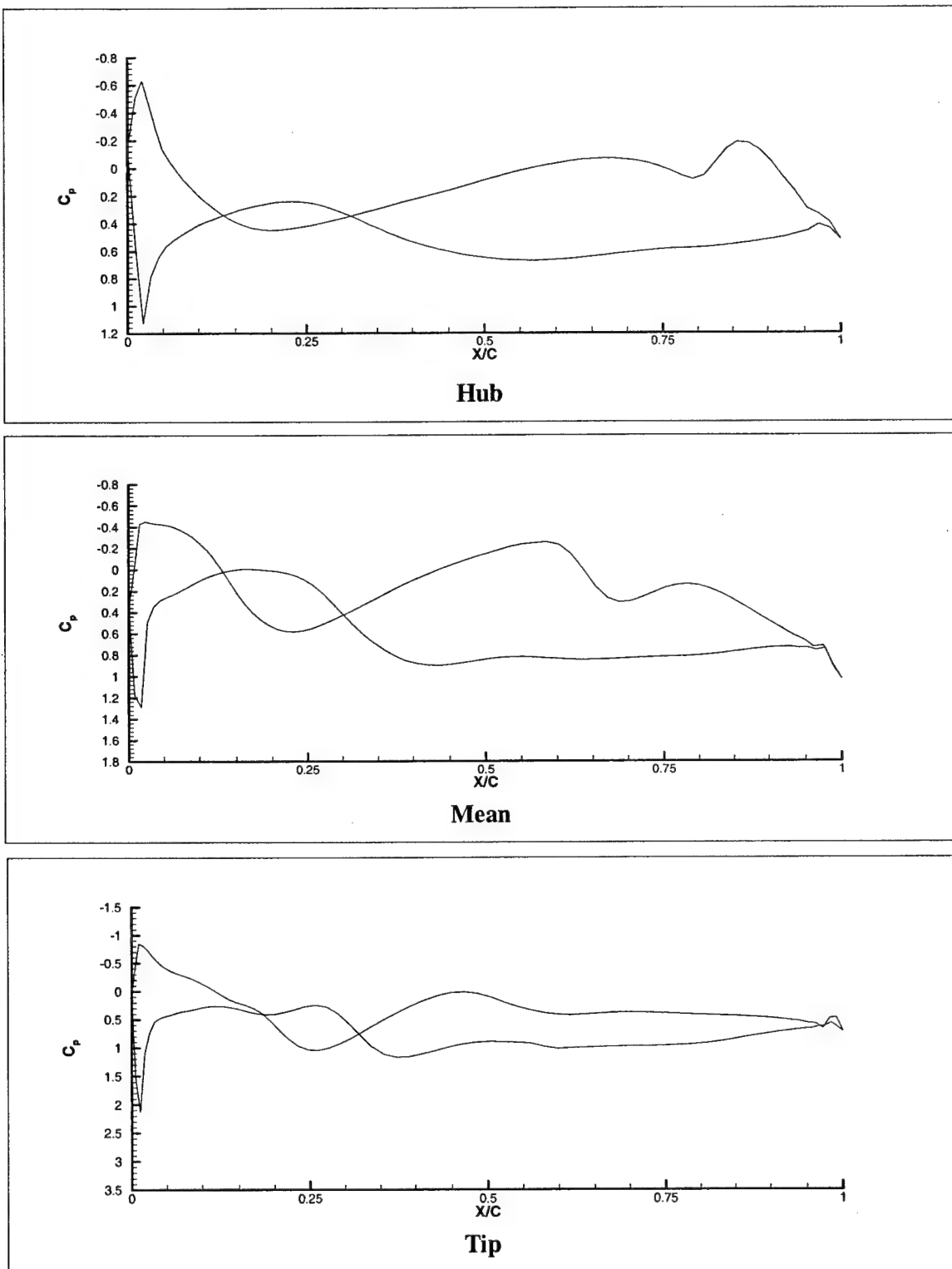


Figure 19. Detuned Rotor B Steady-State  $C_p$  Profiles

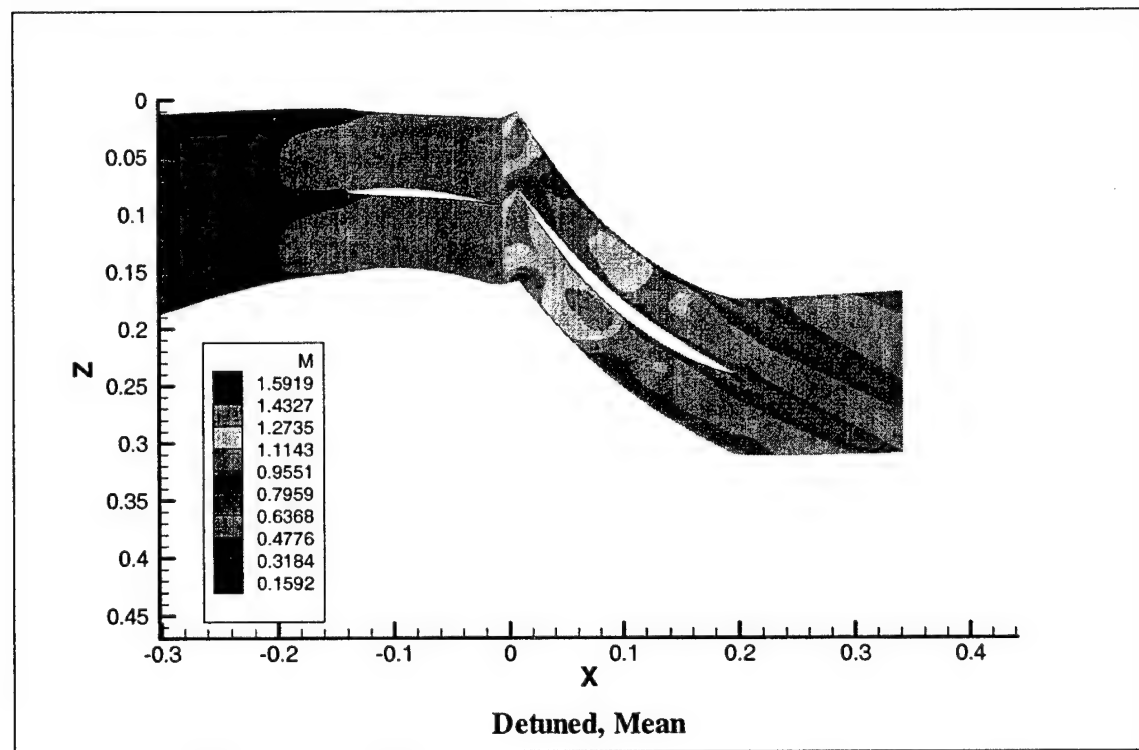
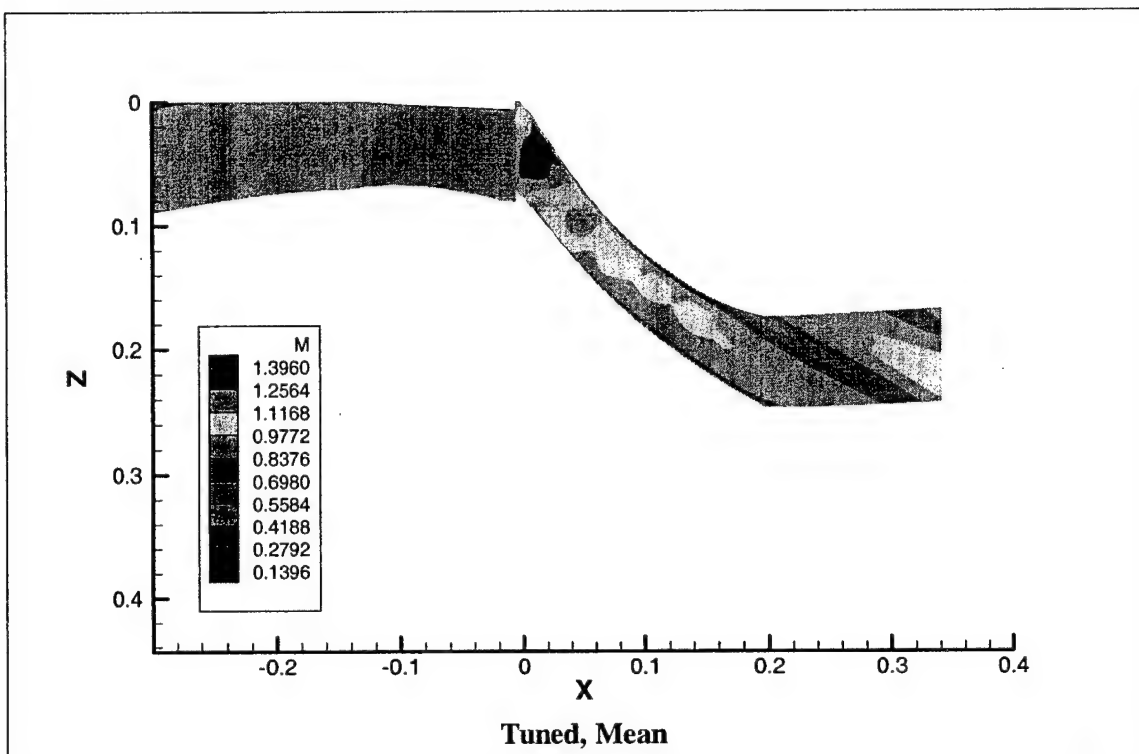


Figure 20. Steady-State Mach Contours, Tuned and Detuned Cases

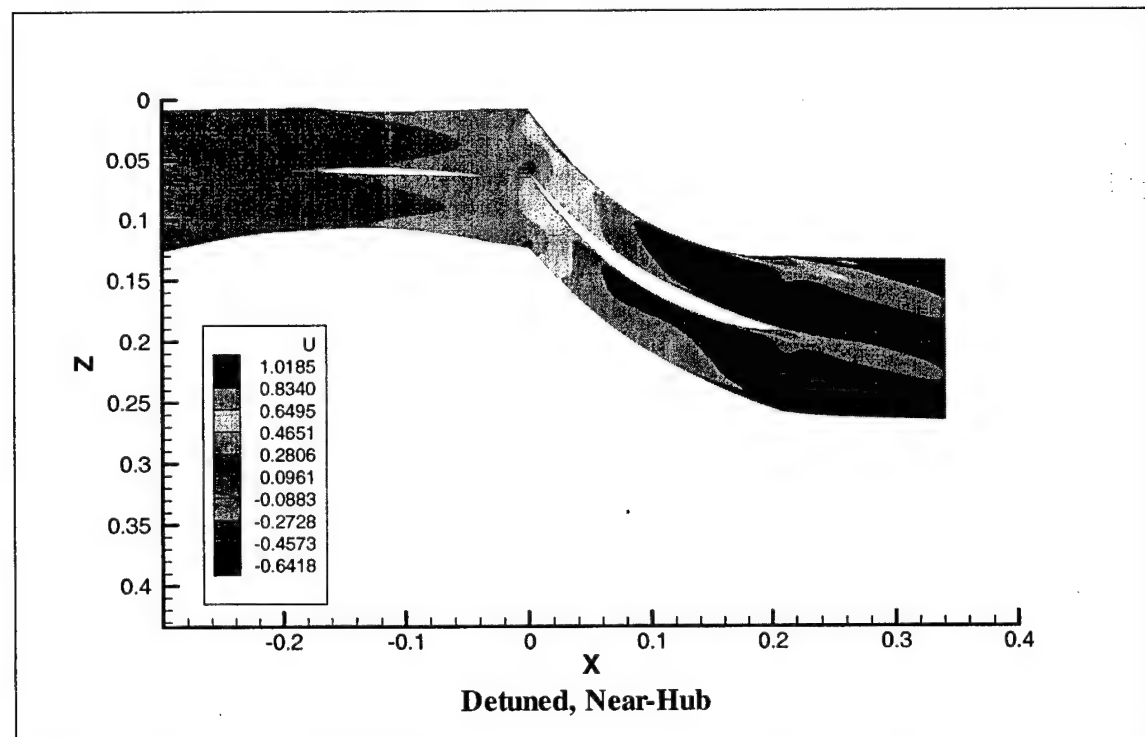
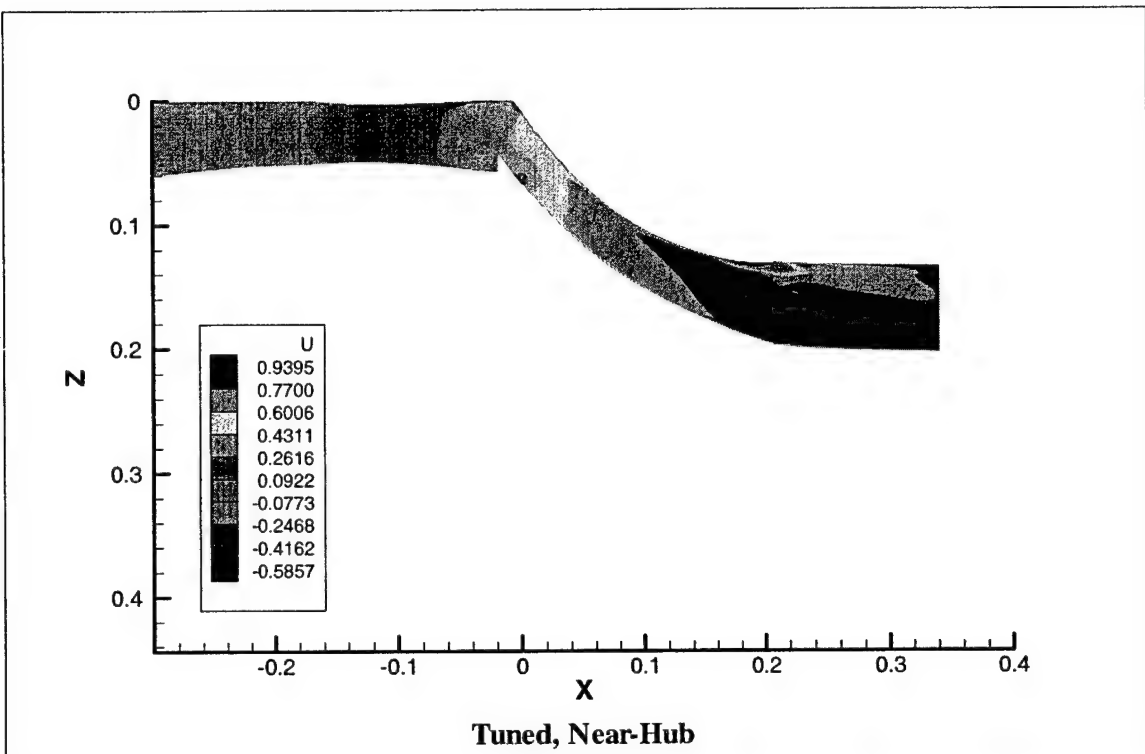


Figure 21. Axial Velocity Contours, Tuned and Detuned Cases

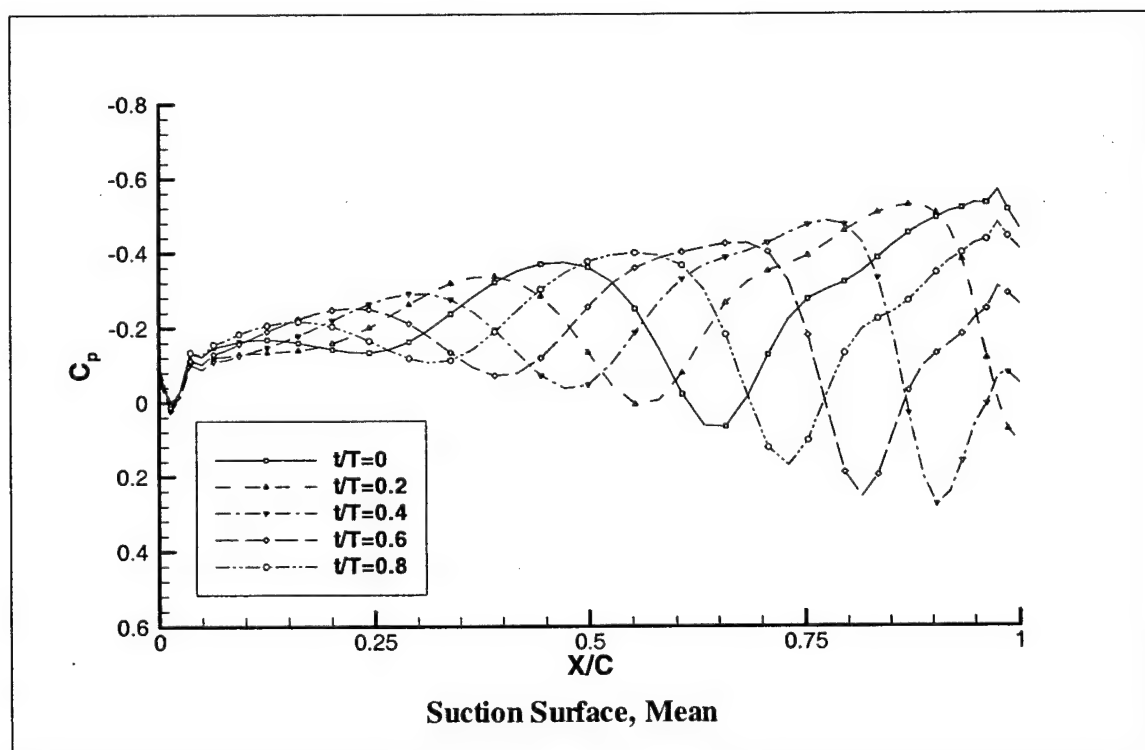
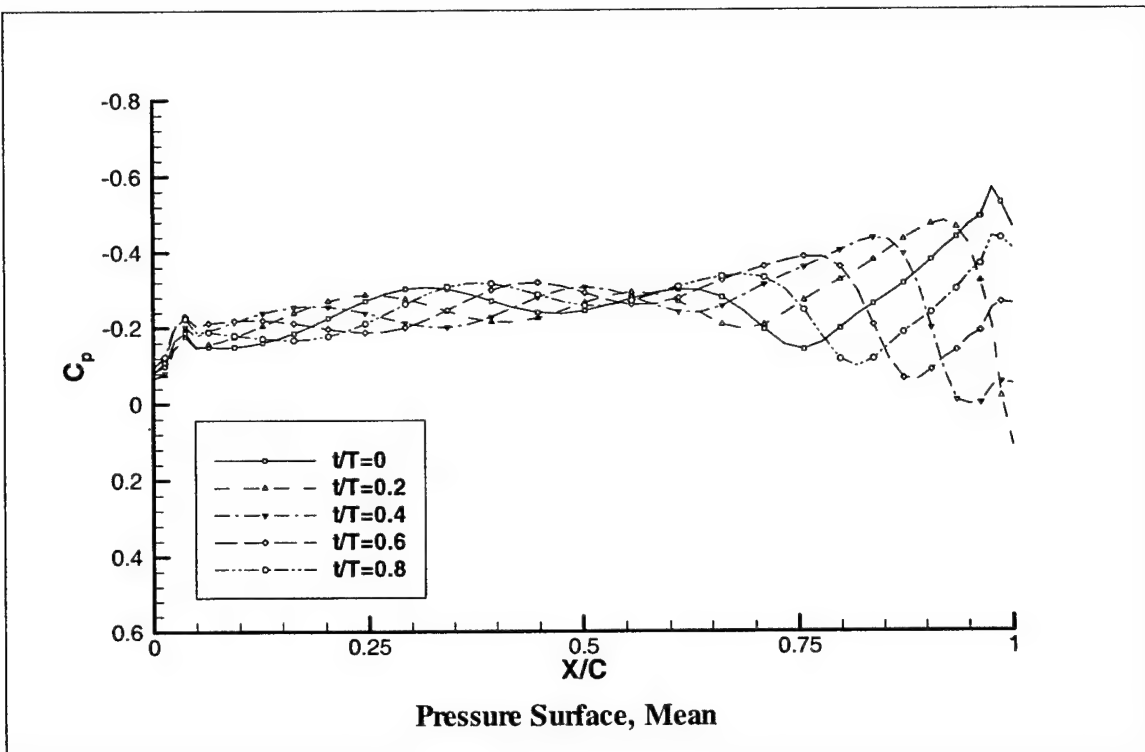


Figure 22. Tuned IGV Unsteady  $C_p$  Profiles

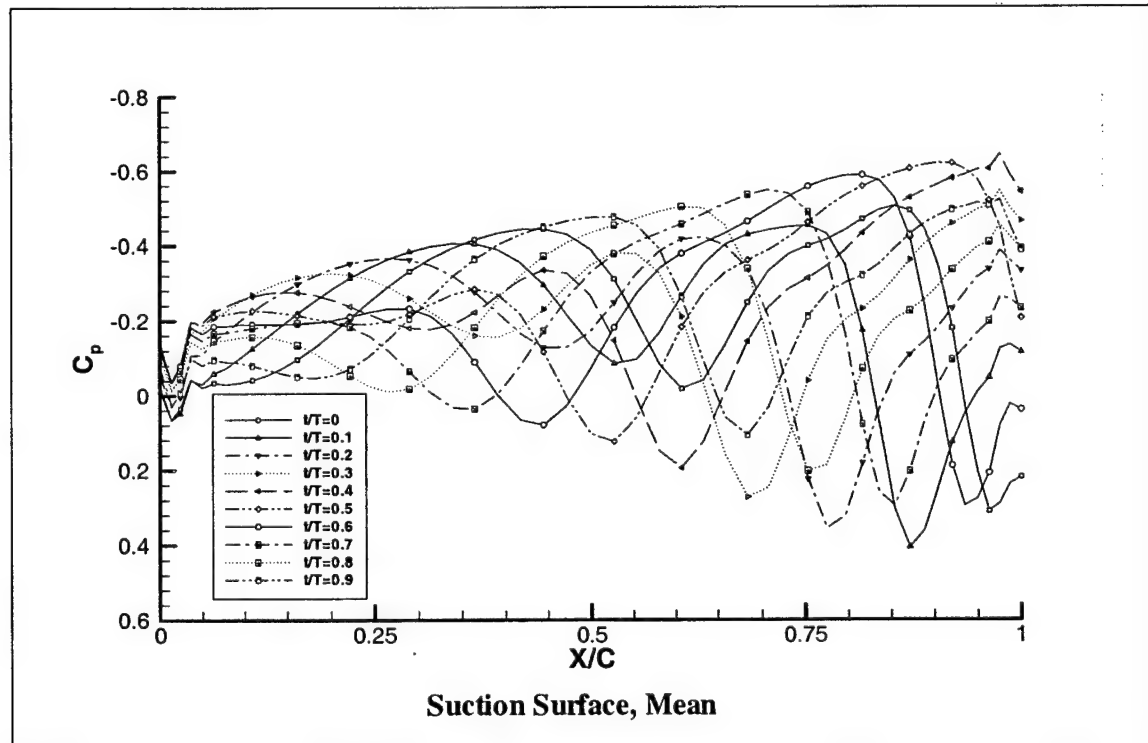
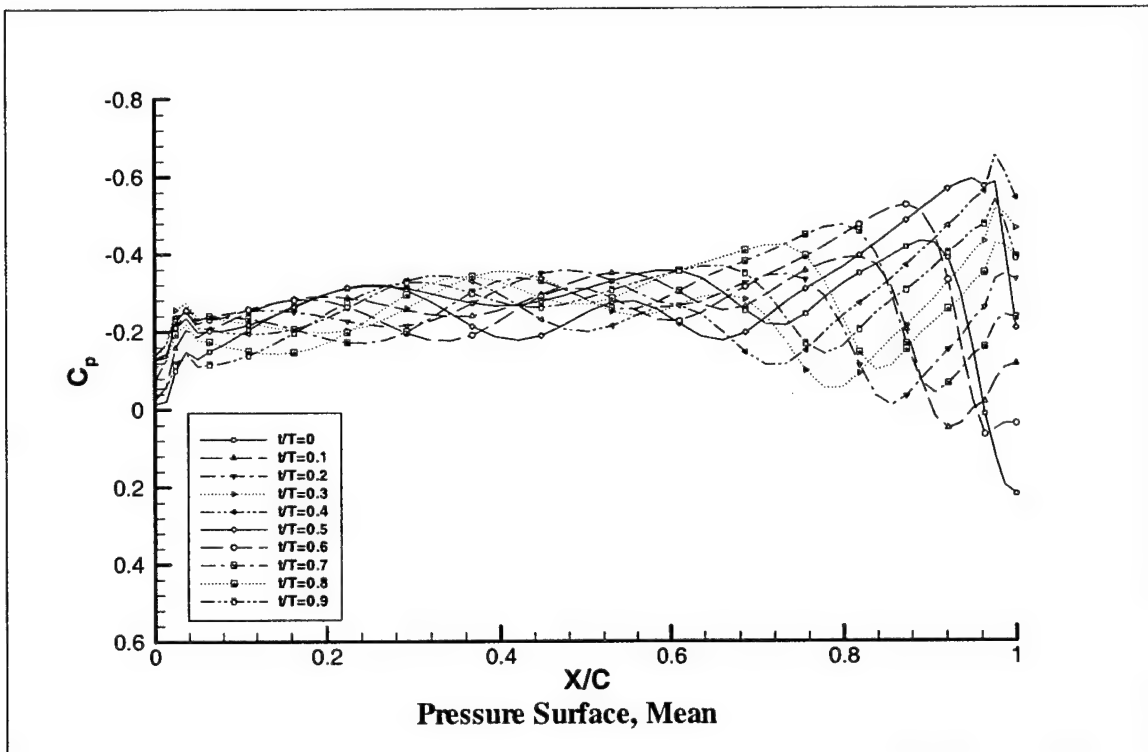


Figure 23. Detuned IGV A Unsteady  $C_p$  Profiles

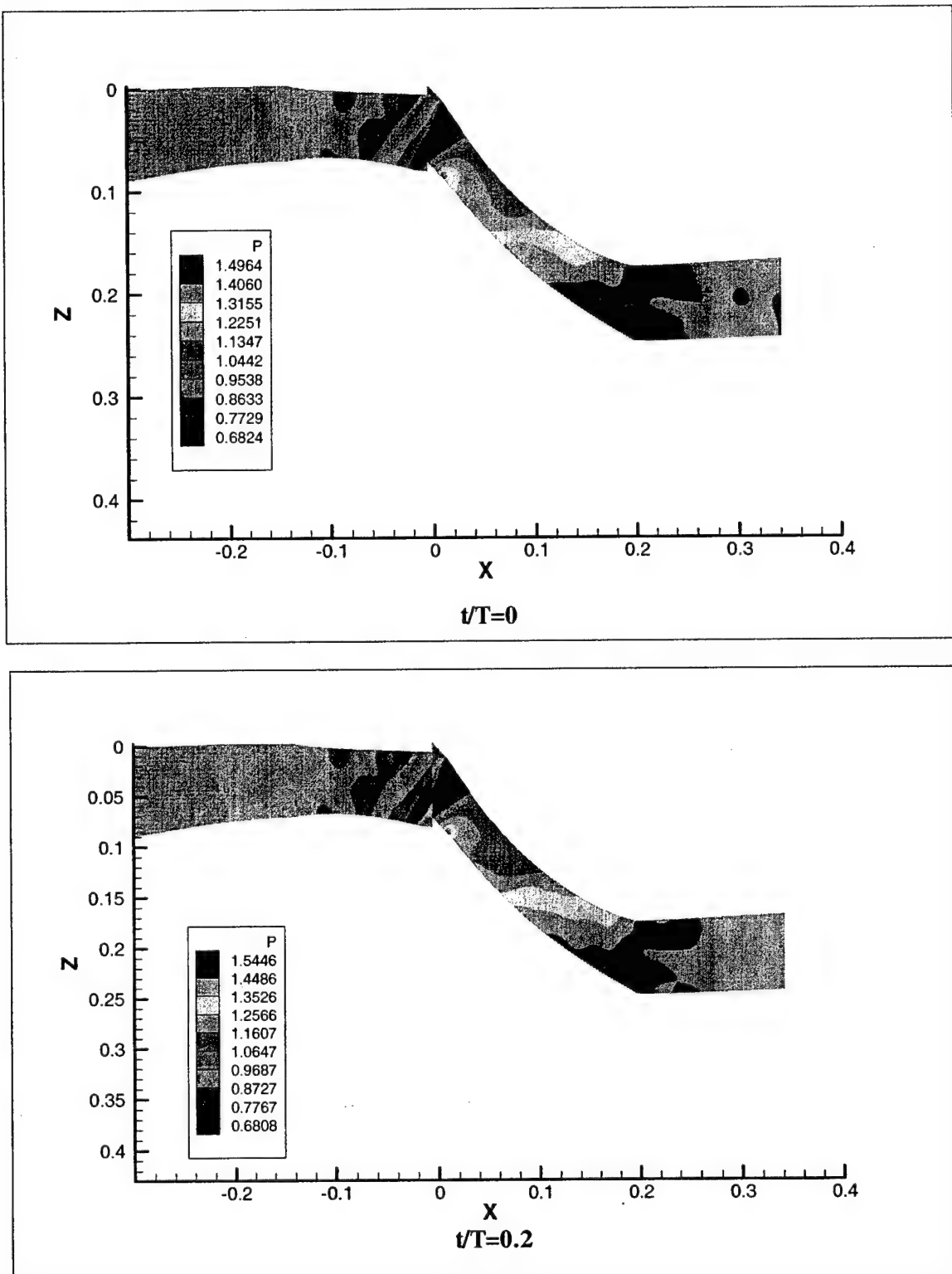


Figure 24. Tuned Case Unsteady Pressure Contours

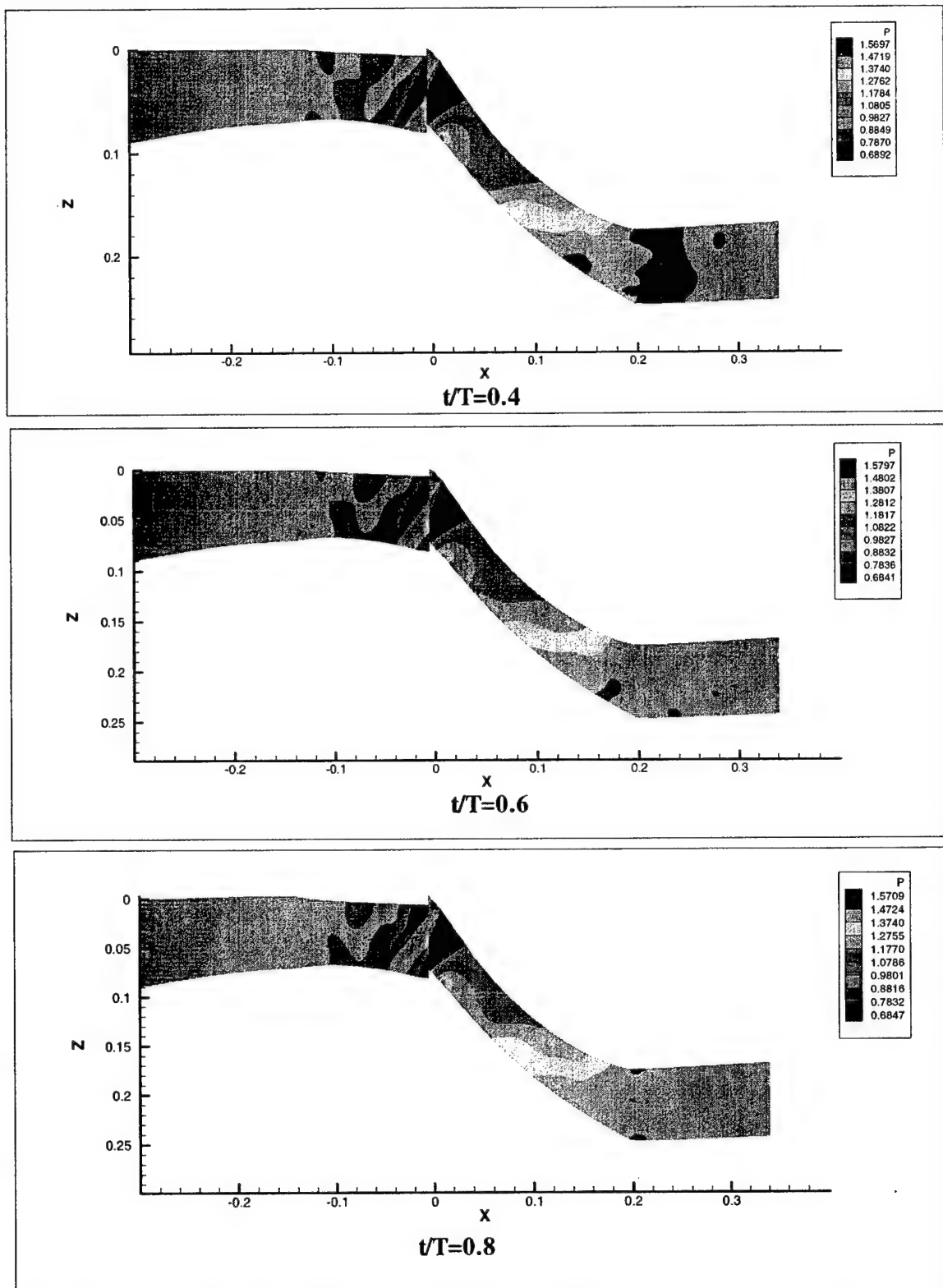


Figure 24 (cont). Tuned Case Unsteady Pressure Contours

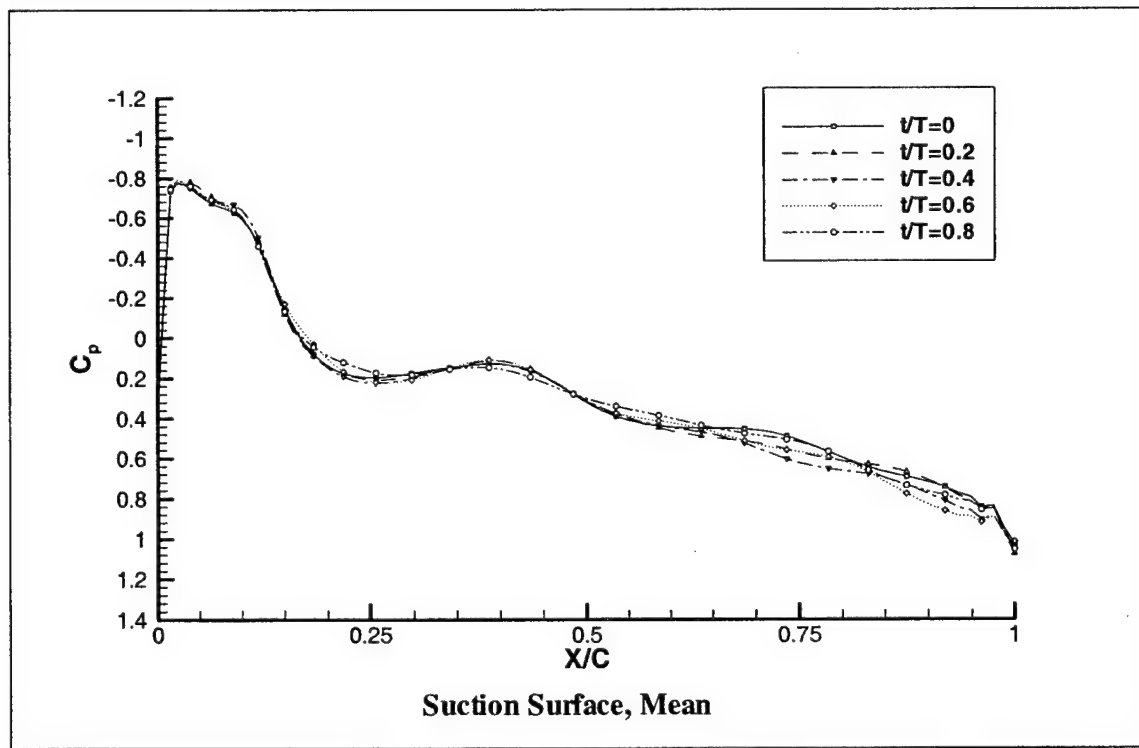
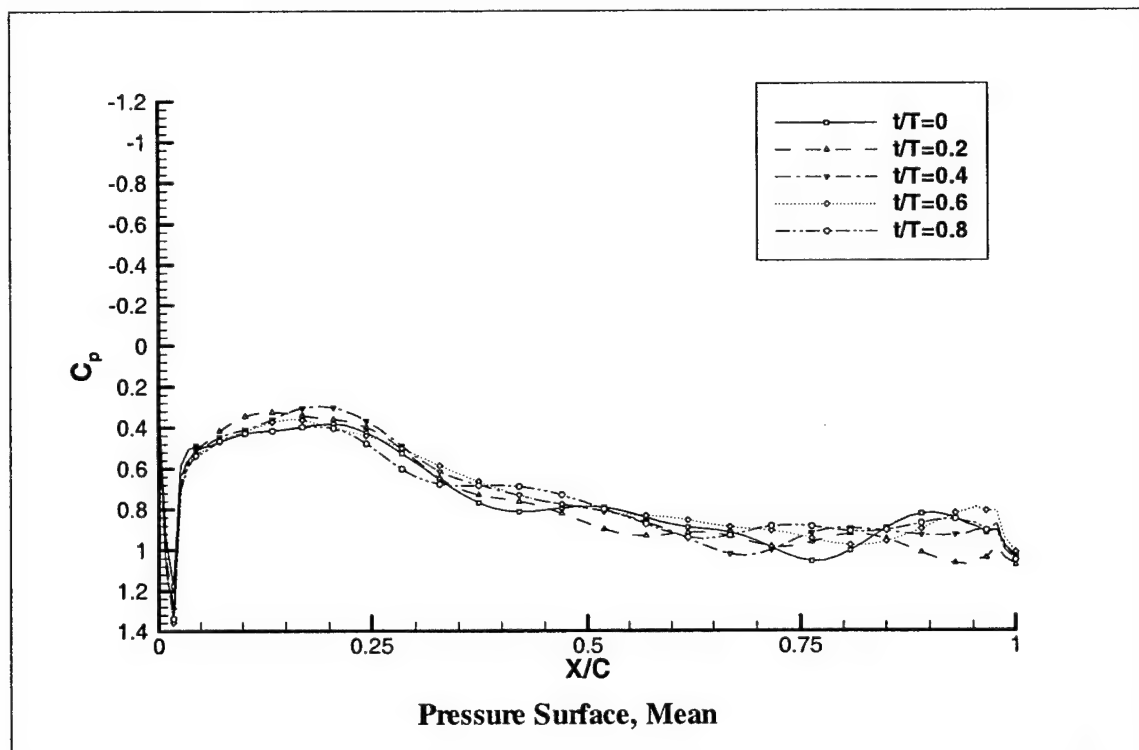


Figure 25. Tuned Rotor Unsteady  $C_p$  Profiles

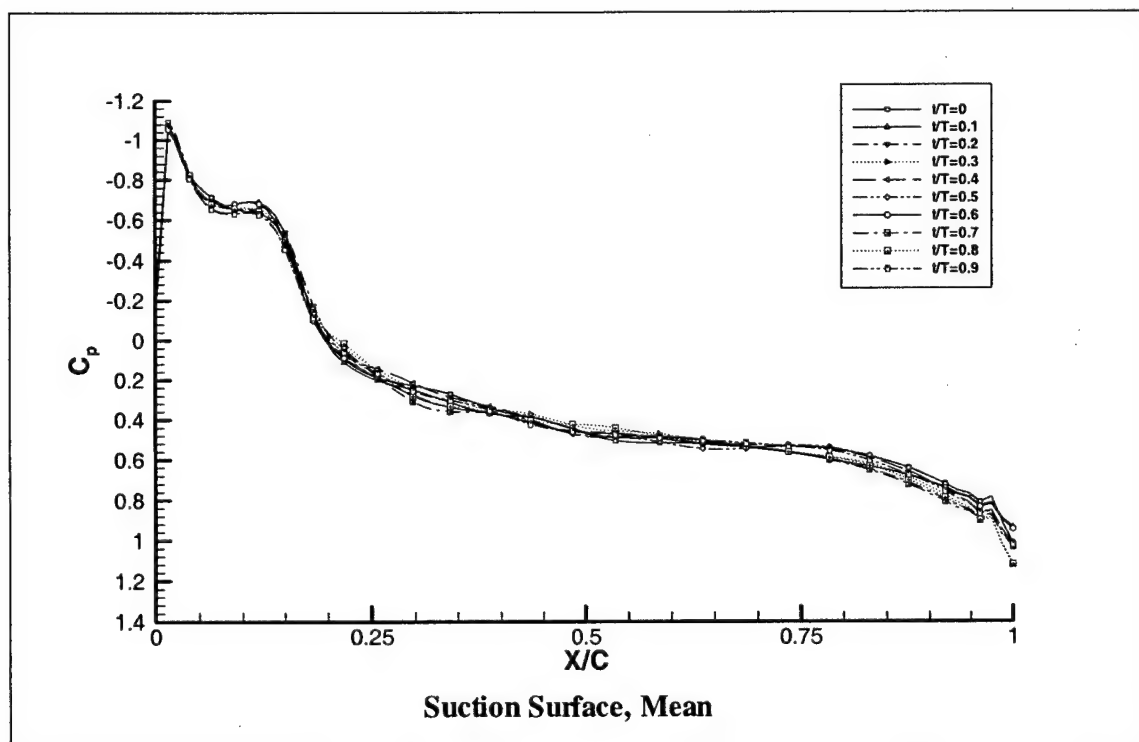
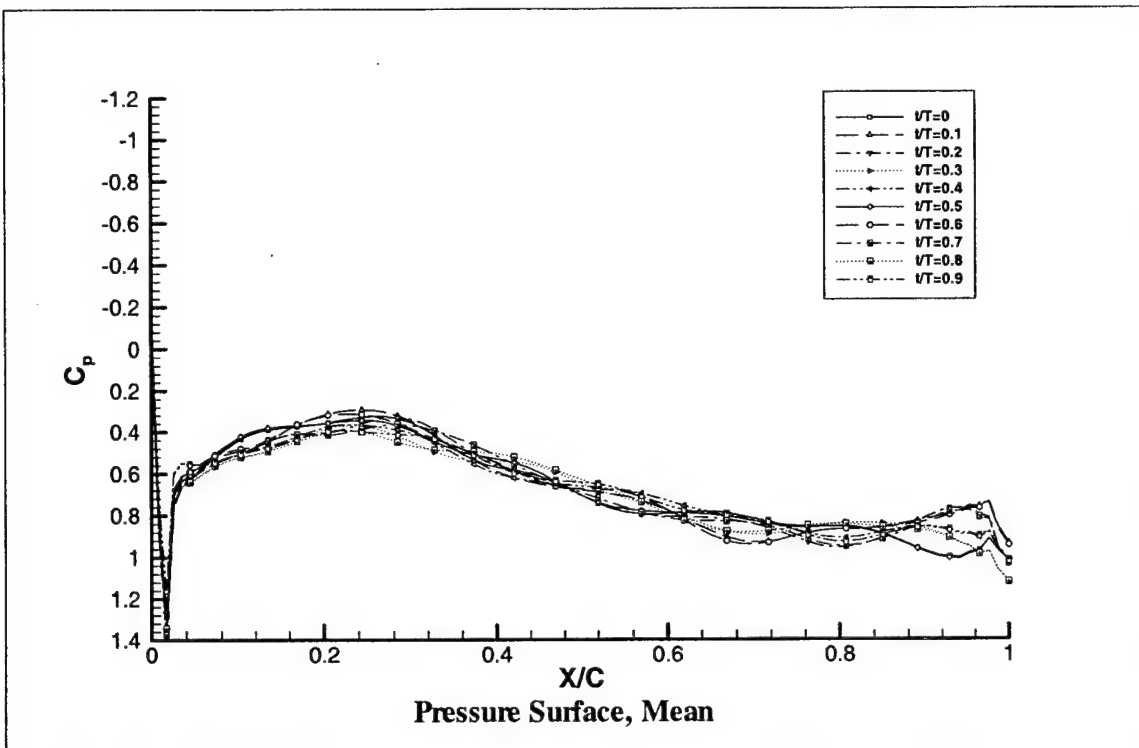


Figure 26. Detuned Rotor A Unsteady  $C_p$  Profiles

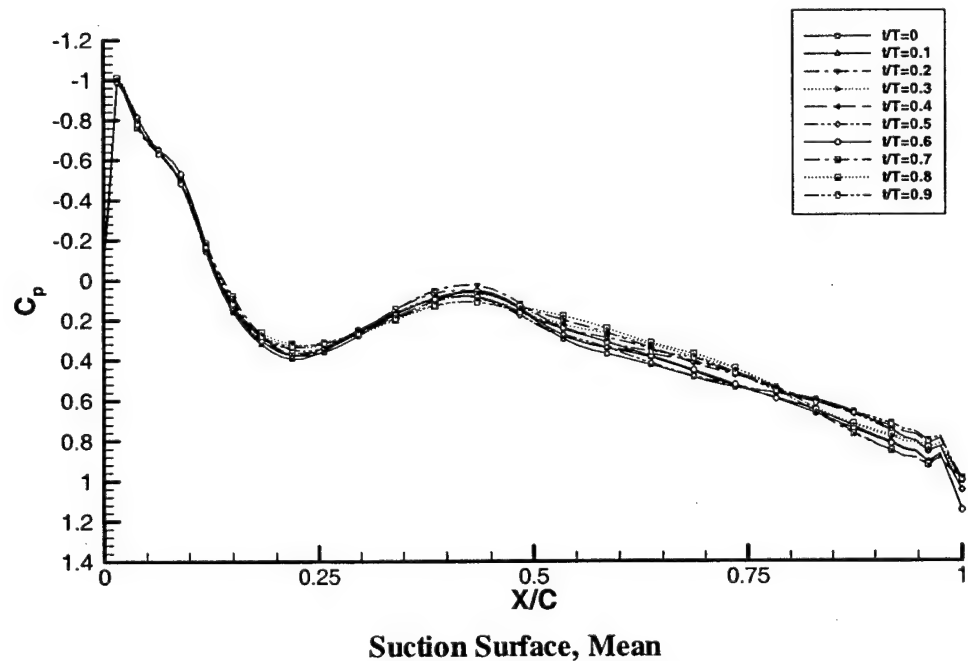
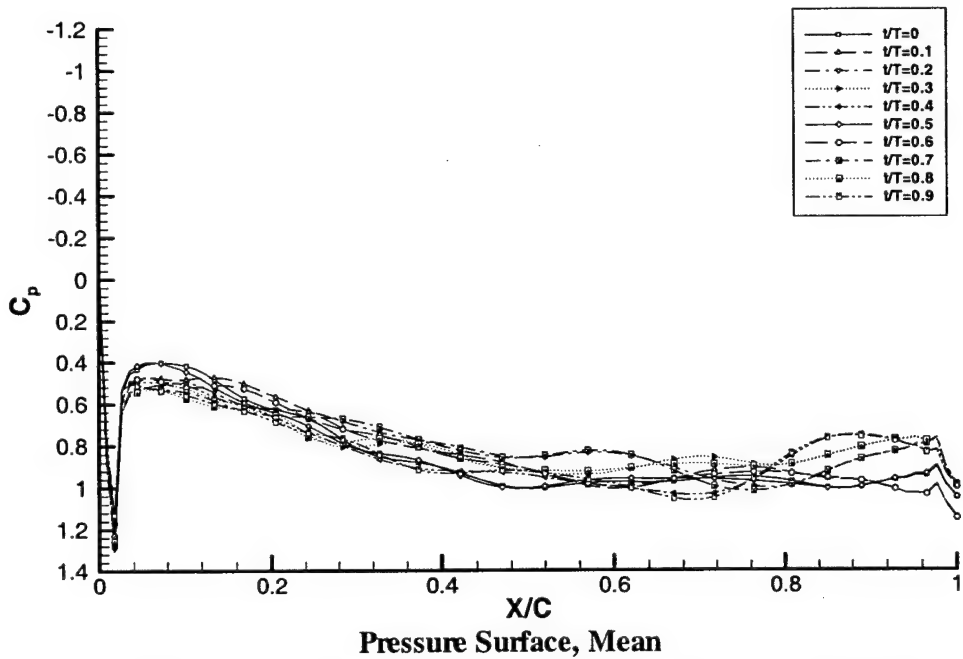


Figure 27. Detuned Rotor B Unsteady  $C_p$  Profiles

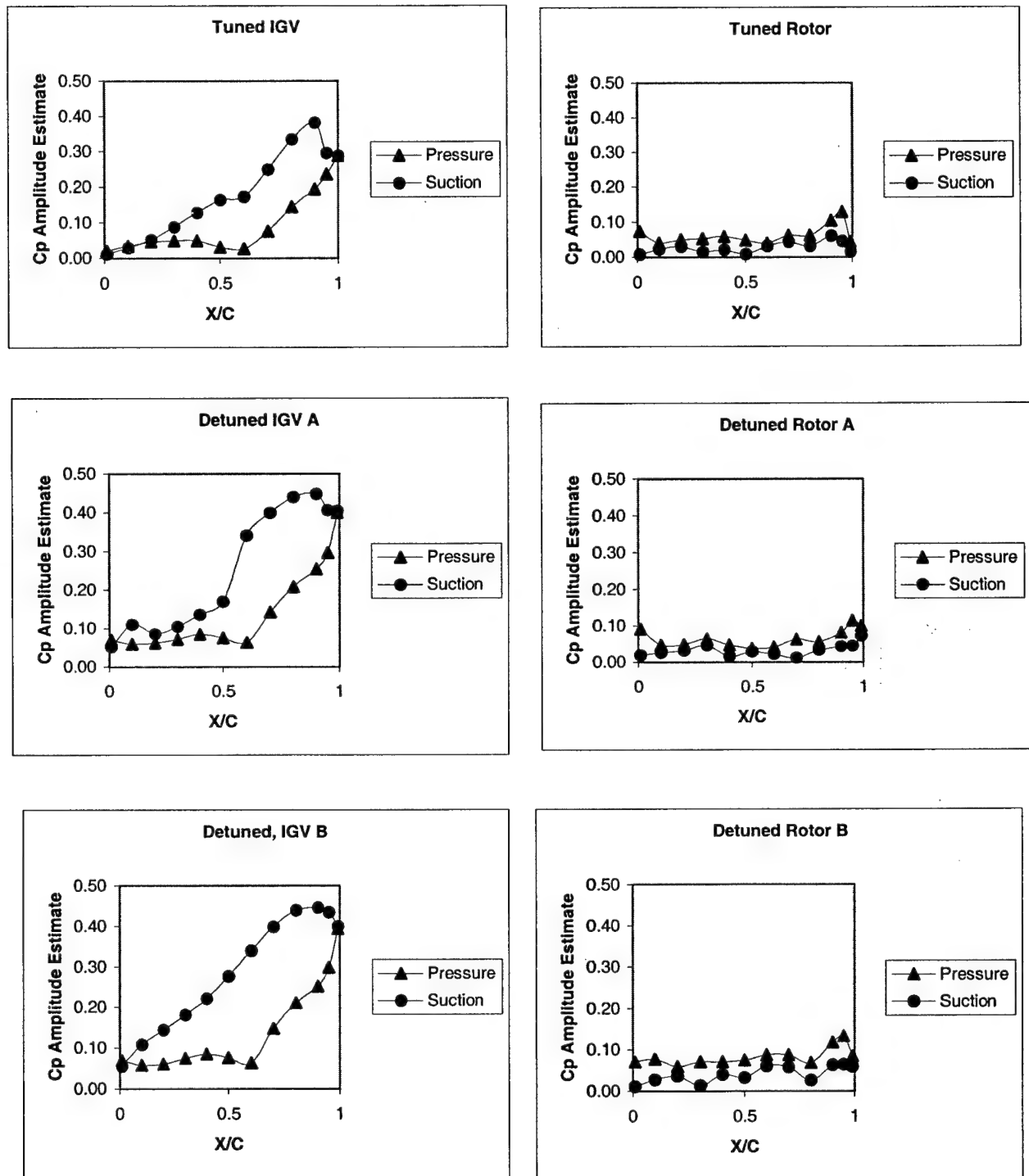


Figure 28. Unsteady  $C_p$  Amplitude Estimates, Tuned and Detuned Cases

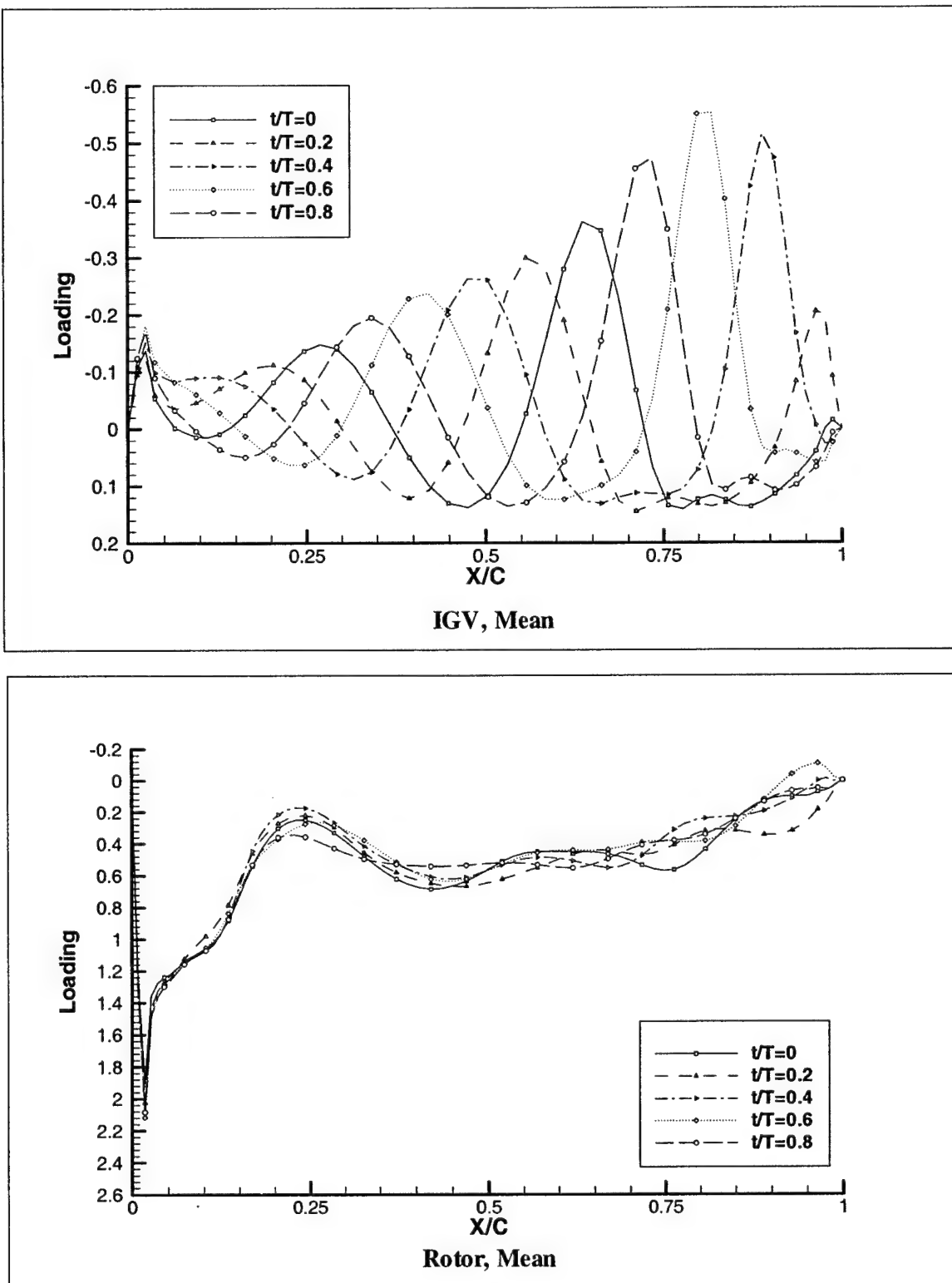


Figure 29. Unsteady Loading, Tuned Case

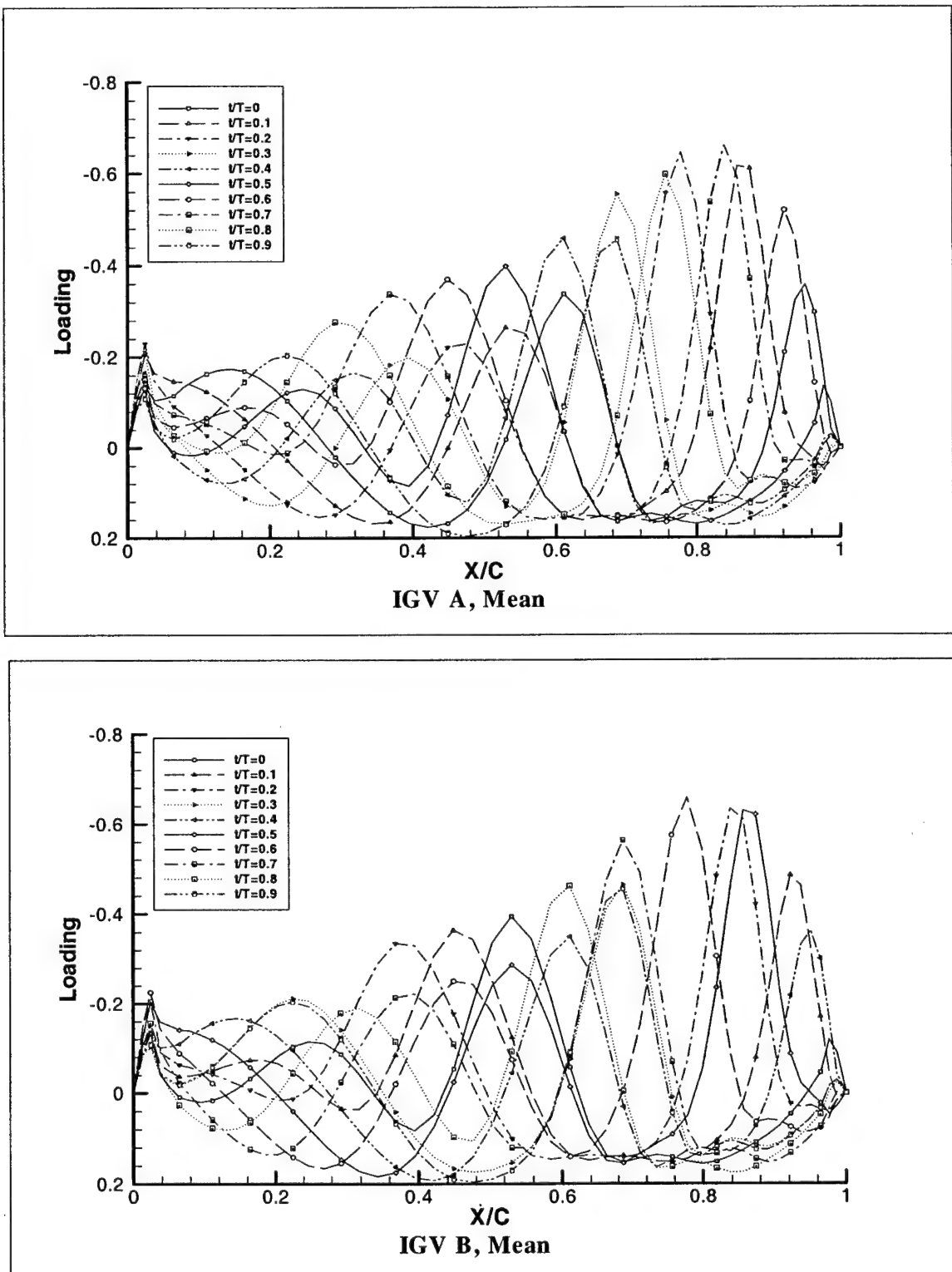


Figure 30. Unsteady IGV Loading, Detuned Case

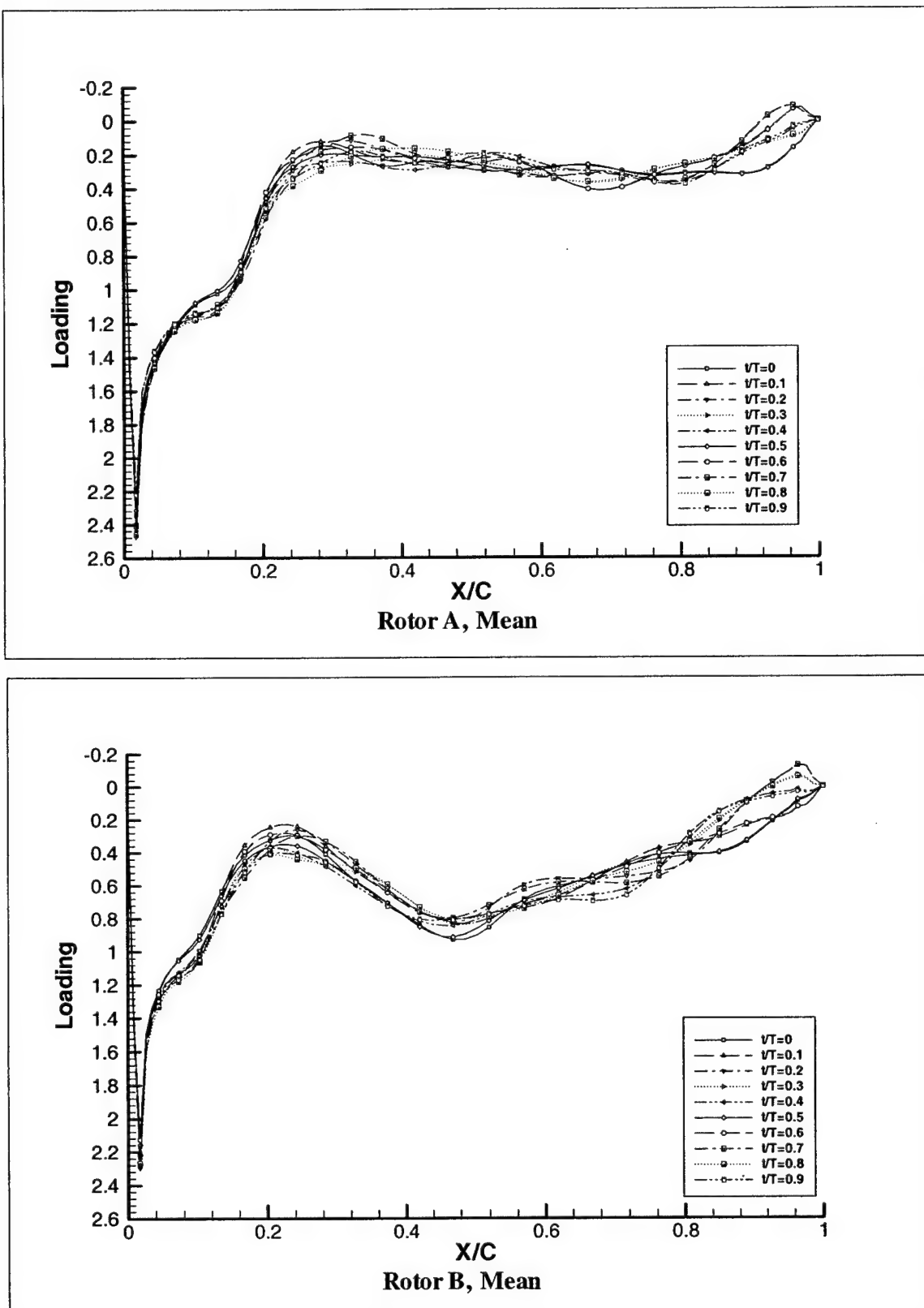


Figure 31. Unsteady Rotor Loading, Detuned Case

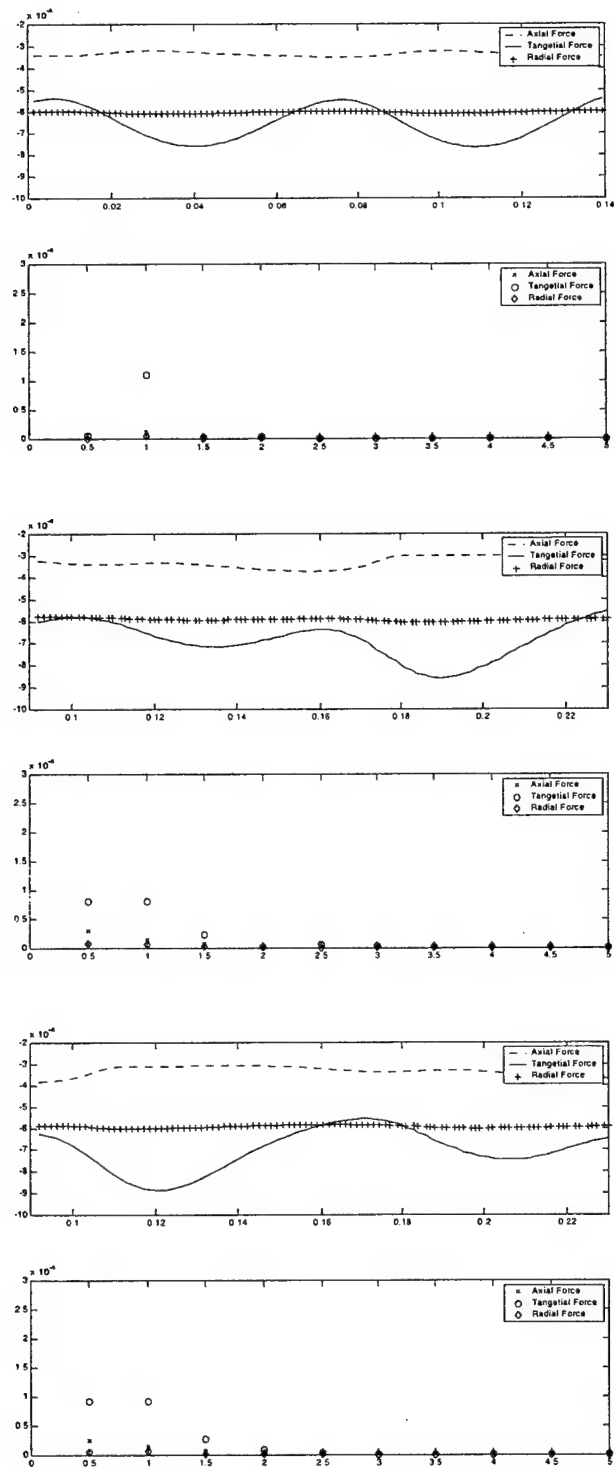


Figure 32. IGV Forces Time History and Fourier Analysis; Tuned, IGV A, IGV B

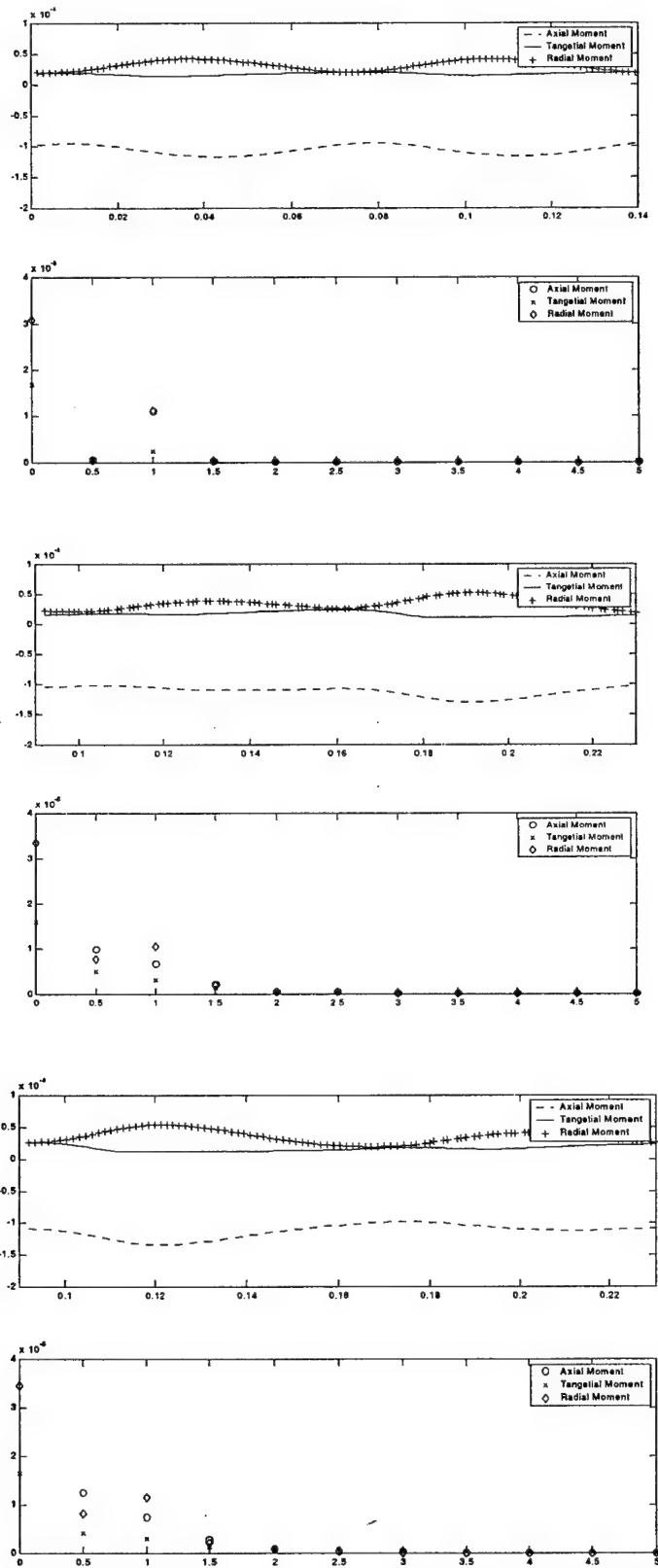


Figure 33. IGV Moment Time History and Fourier Analysis; Tuned, IGV A, IGV B

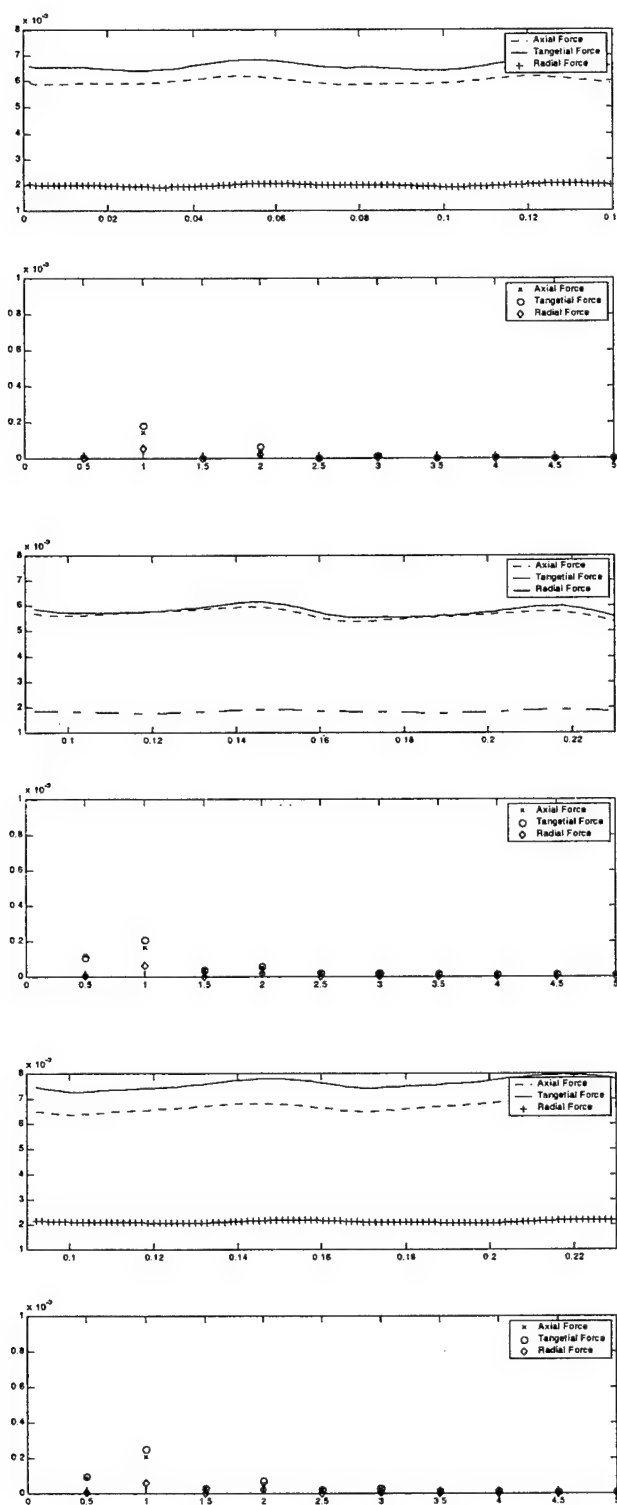


Figure 34. Rotor Forces Time History and Fourier Analysis; Tuned, Rotor A, Rotor B

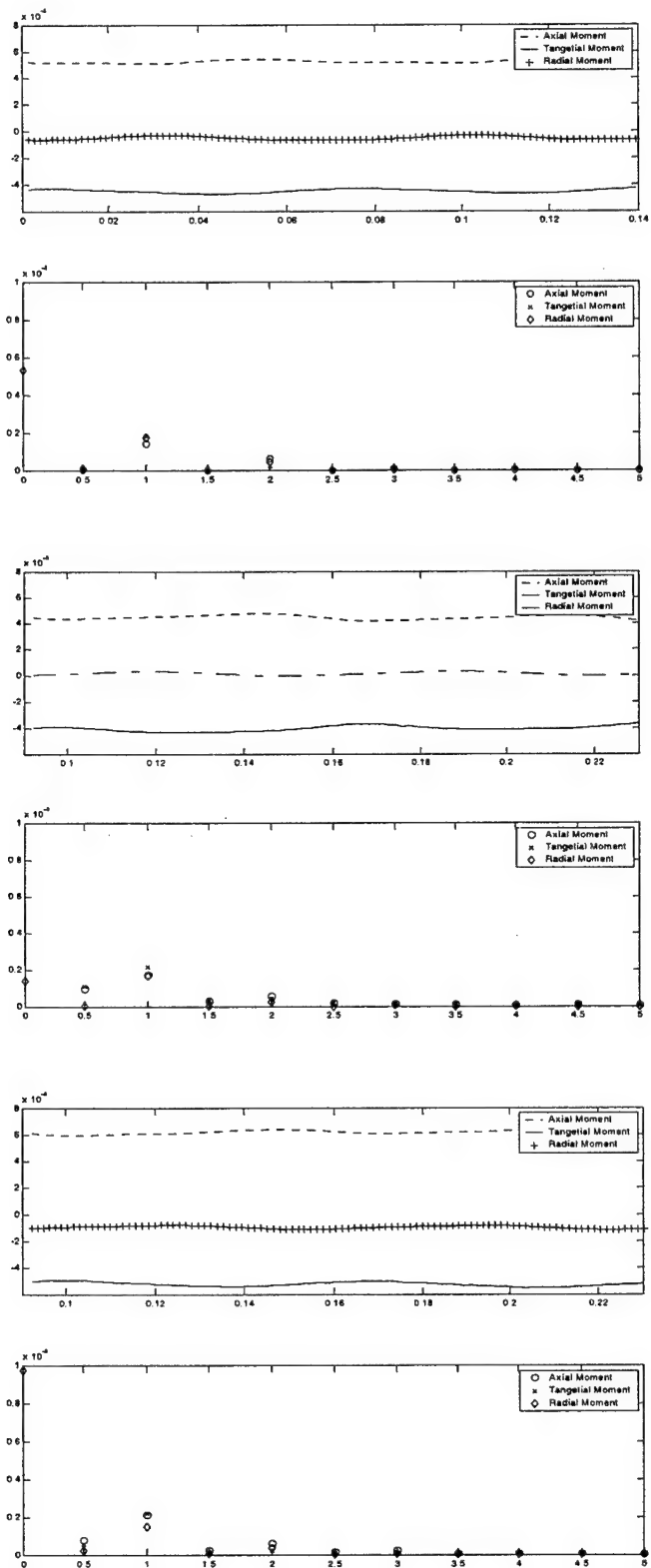


Figure 35. Rotor Moment Time History and Fourier Analysis; Tuned, Rotor A, Rotor

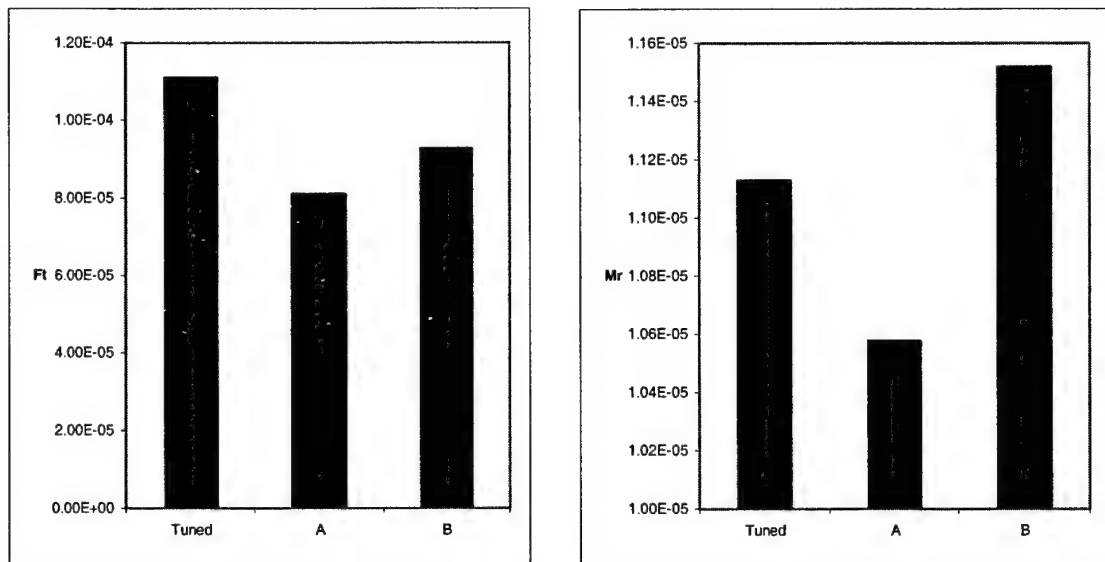


Figure 36. IGV First Harmonics

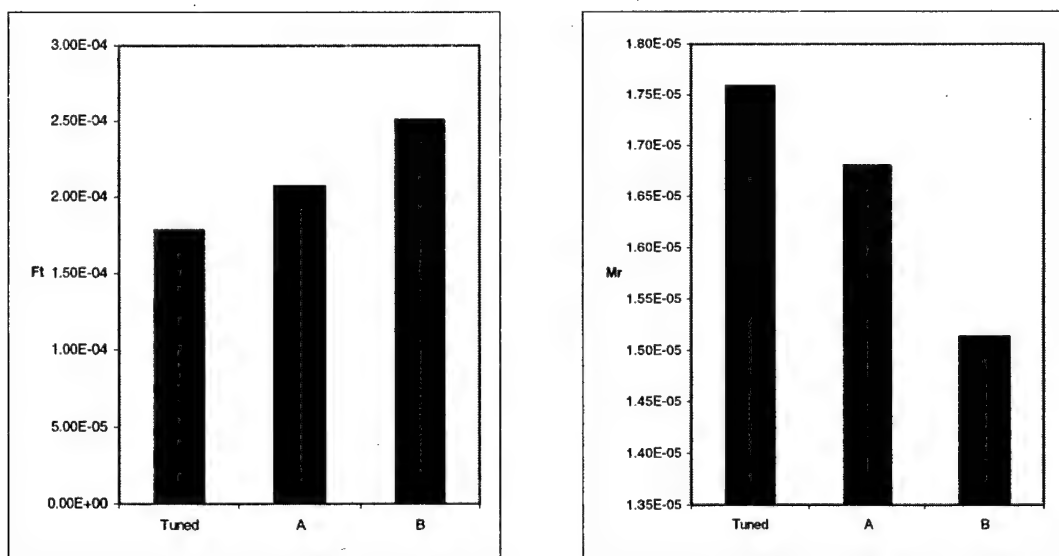


Figure 37. Rotor First Harmonics

## Appendix A: $y^+$ Calculation for Viscous Grids

To determine the spacing necessary to resolve the boundary layer, the wall coordinate  $y^+$  is calculated using the procedure outlined below.

To determine the Reynolds number, the local flow velocity must be calculated. From the given conditions (standard-day) of total pressure, total temperature and the mass flow rate from the TESCOM data report, the mass flow parameter  $\phi$  can be calculated using:

$$\phi = \frac{m\sqrt{T_0}}{AP_0} \quad (A.1)$$

where  $A$  is the local annulus area. To find the Mach number, another definition of the mass flow parameter is:

$$\phi = \sqrt{g_c \frac{\gamma}{R}} \cdot M \cdot \left(1 + \frac{\gamma-1}{2} M^2\right)^{\frac{\gamma+1}{2(\gamma-1)}} \quad (A.2)$$

where  $g_c$  is the gravitational constant and  $R$  is the gas constant. Using a solver routine on a spreadsheet, the local Mach number can be calculated. Using standard-day conditions, we can calculate the local flow velocity from:

$$U = M \cdot \sqrt{\gamma RT} \quad (A.3)$$

The Reynolds number is then calculated from:

$$Re_x = \frac{\rho U_x}{\mu} \quad (A.4)$$

If we assume a Blasius flat-plate solution, the skin friction coefficient is given by:

$$C_f = \frac{0.664}{\sqrt{\text{Re}_x}} \quad (\text{A.5})$$

Assuming a  $y^+$  value of one, the local  $y$  value can be calculated from the following definitions:

$$C_f = \frac{\tau_w}{\frac{1}{2} \rho U^2} \quad (\text{A.6})$$

$$\nu = \frac{\mu}{\rho} \quad (\text{A.7})$$

$$y^+ = \frac{y}{\nu} \sqrt{\frac{\tau_w}{\rho}} \quad (\text{A.8})$$

## Bibliography

1. El-Aini, Y., R. deLaneuville, A. Stoner, and V. Capece. "High Cycle Fatigue of Turbomachinery Components – Industry Perspective," AIAA Paper No. 97-3365, AIAA/ASME/SAE/ASEE 33<sup>rd</sup> Joint Propulsion Conference and Exhibit, Seattle, WA, July 6-9, 1997.
2. Richman, Michael and Sanford Fleeter. "Navier-Stokes Simulation of IGV-Rotor-Stator Interactions In a Transonic Compressor," AIAA Paper No. 2000-3379, AIAA/ASME/SAE/ASEE 36<sup>th</sup> Joint Propulsion Conference and Exhibit, Huntsville, AL, July 16-19, 2000.
3. Hall, Edward J., Nathan J. Heidegger, and Robert A. Delaney. ADPAC v1.0 – User's Manual, NASA/CR-1999-206600.
4. Sanders, A. and S. Fleeter. "Rotor Blade-to-Blade Wake Variability and Its Effect on Downstream Vane Response," AIAA Paper No. 97-2753, AIAA/ASME/SAE/ASEE 33<sup>rd</sup> Joint Propulsion Conference and Exhibit, Seattle, WA, July 6-9, 1997.
5. Chiang, H., and S. Fleeter. "Oscillating Aerodynamics and Flutter of an Aerodynamically Detuned Cascade in an Incompressible Flow," AIAA Paper No. 89-0289, 27<sup>th</sup> Aerospace Sciences Meeting, Reno, NV, January 9-12, 1989.
6. Spara, K. and S. Fleeter. "Aerodynamic Detuning for Control of Supersonic Rotor Forced Response," AIAA Paper No. 90-2018, AIAA/SAE/ASME/ASEE 26<sup>th</sup> Joint Propulsion Conference, Orlando, FL, July 16-18, 1990.
7. Hoyniak, D. and S. Fleeter. "Aerodynamic Detuning Analysis of an Unstalled Supersonic Turbofan Cascade," ASME Paper No. 85-GT-192, 30<sup>th</sup> International Gas Turbine Conference and Exhibit, Houston TX, March 18-21, 1985.
8. Murthy, Durbha V., Christophe Pierre, and Gisli Ottarsson. "An Efficient Constraint to Account for Mistuning Effects in the Optimal Design of Engine Rotors," AIAA Paper No. 92-4711, 4<sup>th</sup> AIAA/USAF/NASA/OAI Symposium on Multidisciplinary Analysis and Optimizations, Cleveland, OH, September 21-23, 1992.
9. Hoyniak, Daniel, and Sanford Fleeter. "Aerodynamic and Structural Detuning of Supersonic Turbomachine Rotors," AIAA Paper No. 85-0761, AIAA/ASME/ASCE/AHS 25<sup>th</sup> Structures, Structural Dynamics and Materials Conference, Orlando, FL, April 15-17, 1985.

10. Sawyer, Scott, John M. Feiereisen, and Sanford Fleeter. "The Influence of Rotor Detuning On the Acoustic Response of An Annular Cascade," AIAA Paper No. 96-1689, 2<sup>nd</sup> AIAA/CEAS Aeroacoustics Conference, State College, PA, May 6-8, 1996.
11. Car, D. and S. L. Puterbaugh. "Analysis of a Highly Loaded, Transonic, Inlet Compressor Stage: Isolated and Multi-stage Performance," AIAA Paper No. 2000-3206, AIAA/ASME/SAE/ASEE 36<sup>th</sup> Joint Propulsion Conference and Exhibit, Huntsville, AL, July 16-19, 2000.
12. Law, C. H. and Wennerstrom, A. J. "Design of a 1250 ft/s, Low Aspect Ratio, Single-Stage Axial Flow Compressor," AFAPL-TR-79-2096, 1979.
13. Law, C. H. and Puterbaugh, S. L. "A Computer Program For Axial Compressor Design (UD0300M)," AFWAL-TR-82-2074, 1982.
14. Law, C. H. "Investigation of a High-Stage-Loading, Low-Aspect-Ratio, Single-Stage Compressor (TESCOM Configuration 1A)," AFWAL-TR-83-2016, 1983.
15. Jameson, A., W. Schmidt, and E. Turkel. "Numerical Solutions of the Euler Equations by Finite Volume Methods Using Runge-Kutta Time-Stepping Schemes," AIAA Paper No. 81-1259, 1981.
16. Jorgeson, P. C. E., and R. V. Chima, "An Unconditionally Stable Runge-Kutta Method for Unsteady Flows," NASA TM-101347, AIAA Paper No. 89-0205, 1989.
17. Radespiel, R., C. Rossow, and R. C. Swanson. "Efficient Cell Vertex Multigrid Scheme for the Three-Dimensional Navier-Stokes Equations," AIAA Journal, Vol. 28, No. 8, pp. 1464-1472, 1990.
18. Giles, M. B., "Nonreflecting Boundary Conditions for Euler Equation Calculations," AIAA Journal, Vol. 28, No. 12, pp. 2050-2058, 1990.
19. Saxer, A. P., "A Numerical Analysis of 3-D Inviscid Stator/Rotor Interactions Using Non-Reflecting Boundary Conditions," MIT GTL Report 209, 1992.
20. **TIGER™ User Guide.** Documentation for TIGER™ Version X3.1. Catalpa Research, Inc., Champaign, IL, 2000.

## **Vita**

2<sup>nd</sup> Lt. Andrew L. White graduated from the North Carolina School of Science and Mathematics in Durham, North Carolina in May 1995. He entered undergraduate studies at the North Carolina State University in Raleigh, North Carolina from which he graduated with a Bachelor of Science degree in Aerospace Engineering in May 1999. He was commissioned through Detachment 595 AFROTC at the North Carolina State University. His first assignment was to the Air Force Institute of Technology at Wright-Patterson AFB, Ohio.

# REPORT DOCUMENTATION PAGE

Form Approved  
OMB No. 074-0188

The public reporting burden for this collection of information is estimated to average 1 hour per response, including the time for reviewing instructions, searching existing data sources, gathering and maintaining the data needed, and completing and reviewing the collection of information. Send comments regarding this burden estimate or any other aspect of the collection of information, including suggestions for reducing this burden to Department of Defense, Washington Headquarters Services, Directorate for Information Operations and Reports (0704-0188), 1215 Jefferson Davis Highway, Suite 1204, Arlington, VA 22202-4302. Respondents should be aware that notwithstanding any other provision of law, no person shall be subject to a penalty for failing to comply with a collection of information if it does not display a currently valid OMB control number.

PLEASE DO NOT RETURN YOUR FORM TO THE ABOVE ADDRESS.

1. REPORT DATE (DD-MM-YYYY) 20-03-2001			2. REPORT TYPE Master's Thesis		3. DATES COVERED (From – To) Jan 2000 – Mar 2001
4. TITLE AND SUBTITLE  COMPUTATIONAL INVESTIGATION OF AEROMECHANICAL HCF EFFECTS IN A COMPRESSOR ROTOR			5a. CONTRACT NUMBER  5b. GRANT NUMBER  5c. PROGRAM ELEMENT NUMBER  5d. PROJECT NUMBER  5e. TASK NUMBER  5f. WORK UNIT NUMBER		
6. AUTHOR(S)  White, Andrew L., Second Lieutenant, USAF			8. PERFORMING ORGANIZATION REPORT NUMBER  AFIT/GAE/ENY/01M-09		
7. PERFORMING ORGANIZATION NAMES(S) AND ADDRESS(S)  Air Force Institute of Technology Graduate School of Engineering and Management (AFIT/EN) 2950 P Street, Building 640 WPAFB OH 45433-7765			10. SPONSOR/MONITOR'S ACRONYM(S)  11. SPONSOR/MONITOR'S REPORT NUMBER(S)		
9. SPONSORING/MONITORING AGENCY NAME(S) AND ADDRESS(ES)  AFRL/PRTF Attn: Kelly Navarra 1950 Fifth St. Wright-Patterson AFB, OH 45433-5648			Commercial: (937) 255-2734 DSN: 785-2734		
12. DISTRIBUTION/AVAILABILITY STATEMENT  APPROVED FOR PUBLIC RELEASE; DISTRIBUTION UNLIMITED.					
13. SUPPLEMENTARY NOTES					
14. ABSTRACT  High-Cycle Fatigue is a major problem facing the gas turbine industry today. It has been investigated by many researchers, using many different methods. Due to its highly complex nature, designers still do not have adequate tools to accurately predict the onset of high-cycle fatigue.  A three-dimensional Navier-Stokes program was used to perform a study of the unsteady aerodynamics on a compressor rotor. The effect of aerodynamic detuning on the forced response of a rotor blade was compared to a baseline tuned rotor case. Detuning consisted of a ten percent decrease in circumferential spacing between alternate pairs of blades. The high-cycle fatigue effects of this detuning were investigated by examining the unsteady forces and moments on the rotor blades and inlet guide vanes.  Computations were performed using a three-dimensional NASA research code (ADPAC) on a cluster of five desktop PCs. Computational times were on the order of several days for a grid of approximately 500,000 cells. These computations showed that detuning of the rotor blade could result in a reduction in the forced response of the IGV and rotor blades. This reduction came without much loss in overall performance (less than ten percent) and therefore may be a viable option to reduce high-cycle fatigue.					
15. SUBJECT TERMS FATIGUE(MECHANICS), FLUID DYNAMICS, FLUID MECHANICS, UNSTEADY FLOW, COMPUTATIONAL FLUID DYNAMICS, COMPRESSORS, AXIAL FLOW COMPRESSORS, DETUNING					
16. SECURITY CLASSIFICATION OF:		17. LIMITATION OF ABSTRACT	18. NUMBER OF PAGES	19a. NAME OF RESPONSIBLE PERSON Dr. Paul I. King, ENY, Paul.King@afit.edu	
a. REPORT U	b. ABSTRACT U	c. THIS PAGE U	UU	19b. TELEPHONE NUMBER (Include area code) (937) 255-3636, ext 4628	

Standard Form 298 (Rev. 8-98)  
Prescribed by ANSI Std. Z39-18